Università di Pisa

Facoltà di Scienze Matematiche Fisiche e Naturali
Corso di Laurea Specialistica in Scienze Fisiche

Anno Accademico 2005/2006

Tesi

Single top quark studies at CMS

Candidato
Giovanni Petrucciani

Relatore
Prof. Lorenzo Foà

Contents

Introduction

The final aim of this work is to study the searches and analyses of single top quark production at CMS: even if the top quark has been discovered more than a decade ago, only observations of pair production ($t\bar{t}$) have been made so far. A measurement of direct, electroweak, single top quark is important to test our understanding of Standard Model physics, probe the possible existence of fourth generation of fermions through tests of V_{CKM} unitarity, and measure top quark polarization; it is also necessary for many physics searches for which single top quark production is an important background, such as $H \to W\,W \to \ell\,\nu\,\ell\,\nu$ and for the search for charged Higgs bosons, such as those required in supersymmetric models.

In the first part the overall picture of the theoretical basis will be provided, staring from the foundations of the Standard Model, which encompasses almost all our present knowledge of particle physics. The important facts of hadronic physics, such as parton density functions, radiative effects and hadronization will also be introduced, as they are necessary to link LHC and Tevatron cross sections to the interactions between partons (quarks and gluons) and to understand the production of jets, the way outgoing partons appear experimentally. This introduction will be completed with a summary of the phenomenology of the top quark, focused especially on single top production.

After an overview of the Large Hadron Collider (LHC) which is currently being build at CERN, the second part of this work will describe the Charged Muon Solenoid (CMS) experiment, aimed to explore in depth particle physics up to the TeV scale: the main features of the subdetectors (silicon tracker, calorimeters, muon chambers) will be described, together with the reconstruction algorithms for tracks, vertices and "high level objects" like electrons, muons and jets, and the trigger; again, focus will be put mostly on those features interesting for top physics.

A short appendix on some specific aspects of the inner tracker integration and testing, carried on in the INFN Pisa laboratories, of which I had first-hand experience, will conclude this introductory part.

The third and last part of the work is devoted to single top quark searches. After reviewing the latest CDF results for single top searches at Tevatron, the common tools and features useful for CMS studies all the three channels will be presented, which will then be described in depth: t-channel ($qb \to tq'$), with the largest cross section and clear signature, exèpected to be observed in the first LHC runs ($1\,\mathrm{fb}^{-1}$), probably to be observed also at Tevatron in the following years; associate tW production ($qg \to tW$), harder to disentangle from the

background and invisible at Tevatron due to a smaller cross section, but which should be observed after one full year of LHC operation ($10\,\mathrm{fb}^{-1}$); s-channel ($qq' \to t\bar{b}$), for which neat theoretical calculations can be done but with a tiny cross section, whose observation will be an hard goal also for LHC.

The analyses of the three channels that will be published in the CMS collaboration Physics Technical Design Report have been done almost independently by three groups, and I contributed personally to the tW channel. In this thesis, anyway, all three channels will be revisited trying to check, and possibly improve, some of the results applying a uniform treatment to issues common to the three channels, and using the tools that were brought up those analyses and in those for similar physics channels like $t\bar{t}$ and $H \to W\,W$.

Part I

Standard Model and top quark physics

Chapter 1

The Standard Model

The "Standard Model" (SM) is the theory that summarizes almost all the knowledge we have on particle physics; it describes a wide range of phenomena, and has been tested experimentally with a remarkable accuracy, even if there are some small but important problems on which it gives no satisfactory answer.

While the theory has emerged gradually in almost a century of theoretical and experimental investigation, and it is not yet fully established, we will describe it from the logical point of view, and not the historical one.

Quantum field theory is a vast subject, and even a short but comprehensive resume of it would be too long for this thesis, so we will only introduce the key concepts that will be useful later on.

Theoretical rigor is not among our aims, and all mathematical details will be left over. Most of the results come from the *perturbative* quantum field theory, which is in excellent accord with the observations, even if the there are some problems in the deep mathematical foundations of the theory which probably prohibit the interpretation of it as "final theory of everything".

1.1 Particles of the SM

The standard model particles can be grouped into three categories:

- **Matter**, fermions with spin $\frac{1}{2}$: three leptons e, μ, τ with their associated neutrinos ν, and six quarks u, d, s, c, b, t.
- **Gauge bosons**, spin 1 bosons that carry interactions between fermions: the well known photon γ, the weak $W^{\pm}, Z^0$ and the octet of gluons g
- The **Higgs sector**, which has not been observed yet but is necessary for the model, as it is the means through which particles acquire mass: in the SM this sector is minimal, and contains just one neutral scalar H, but non minimal options with more particles have also been considered.

Chirality and parity In the SM the left-handed fermions have different interactions than their right-handed partners, so the two halves must be considered separately. This also means that parity (P) is not just broken, but really not defined for the SM particles; as anti-particles have the opposite chirality, the

product of charge conjugation and parity (CP) is well defined (and nevertheless broken).

Neutrinos As the evidence for non massless neutrinos is now compelling, the classic SM picture with three massless left-handed neutrinos ν is starting to be replaced by an extended one with three additional (heavy) right handed neutrinos N.

Generations SM fermions are often divided into three generations, each of which contains one charged lepton, one neutrino and a pair of quarks (e, ν_e, u, d)

1.2 The gauge theory

1.2.1 Gauge theories

Gauge theories are particular quantum field theories in which particles have an **internal local symmetry**: "internal" means that it does not touch the space-time degrees of freedom of a particle[1], "local" that the parameters of this transformation are functions of the space-time position.

Let $\mathcal{G}$ be some Lie group[2]: all our fields will form representations of this group, and the action $S = \int \mathcal{L} d^4x$ must be invariant under such transformations, which is most often achieved by making the Lagrangian itself invariant.

Fields transform as $\phi'^i(x) = U^{ij}(x)\phi^j(x)$, but ordinary derivatives transform differently due to an extra term $(\partial_\mu \phi'^i(x) = U^{ij}(x)\partial_\mu \phi^j(x) + \phi^j(x)\partial_\mu U^{ij}(X))$, and so a covariant derivative is introduced as

$$D_\mu \phi^i(x) = \partial_\mu \phi^i(x) - i\, g\, t_a^{ij} A_\mu^a(x) \phi^j(x)$$

where $A_\mu^a(x)$ are the gauge vector fields, t_a^{ij} the generators of $\mathcal{G}$ in the representation of the fields ϕ^i and g is the charge[3]. If all ordinary derivatives are replaced with covariant ones then a Lagrangian invariant under the global symmetry is made invariant also under gauge transformations.

The beautiful feature of gauge theories is that the interacting Lagrangian $\mathcal{L}$ can be obtained easily from the free one just by replacing the ordinary derivatives in the kinetic terms with the covariant ones. This means that the most general gauge theory with vectors and fermions can be synthetically written as

$$\mathcal{L} = -\frac{1}{4} F_{\mu\nu}^a F^{\mu\nu a} + \bar{\psi}(i \not{D} - m)\psi$$

Because of this, gauge theories are very constrained: the only choices are the group, the representation of the fermions (gauge bosons are always in the fundamental representation), and the value of the charges: for non abelian groups

[1] Coleman and Mandula proved that almost all the possible additional symmetries of a relativistic QFTs are internal except for supersymmetry

[2] A group with real or complex parameters, well described by the generators T^a of the infinitesimal transformations, which obey anti-commutation rules $[T^a, T^b] = i f^{abc} T^c$

[3] If the group is "simple" there is just one charge g; otherwise $\mathcal{G}$ can be the product of many groups $\mathcal{G}_i$ each with it's own charge g_i

(i.e. $SU(2)$) there is just one charge, while abelian $U(1)$ can have a different charge for each particle.

1.2.2 The SM: $SU(3)_C \times SU(2)_L \times U(1)_Y$

The gauge group of the SM is the direct product $SU(3)_C \times SU(2)_L \times U(1)_Y$.

Strong $SU(3)_C$

$SU(3)$ is the group which describes the strong interactions among quarks and gluons, also called "colour" interactions and whose theory is Quantum Chromo-Dynamics (QCD). It has 8 generators, so in the theory there will be 8 massless gauge bosons, the gluons; the group is non abelian, and so the gluon themselves carry a charge and have strong interactions. Among the many available representations for the fermions, the quarks fill in the simplest non trivial ones, **3** and $\bar{\mathbf{3}}$, which can be multiplied to produce both the gauge-invariant bilinear $\bar{q}q$ for the mass term and the octet current $\bar{q}\gamma^\mu \lambda^a q$ which couples to the gluons.

Strong coupling At low energies the interactions among quarks are very strong, and no perturbative treatment can be done; lattice approaches are used successfully to calculate QCD corrections to meson decays with good accuracy, and other results can be obtained through dispersion relations, but there are very important unresolved issues such as confinement. The energy scale at which these effects become important is $\Lambda_{QCD} \sim 250\,\mathrm{MeV}$, which is roughly the mass scale of light hadrons.

Confinement It is an experimental fact that all free particles are "colorless" $SU(3)$ singlets: all mesons are in the scalar $\bar{q}^a q^a$ state, and barions are in the antisymmetrical $\epsilon^{abc} q^a q^b q^c$. The phenomenological explanation for this is that among coloured particles there is an attractive force with increases for increasing distance, but there is yet no well proved and quantitative explanation of this behaviour from a theoretical point of view[4].

Asymptotic freedom In the high energy, " ultraviolet", regime the behaviour of QCD changes: vacuum polarization for this theory is such that the renormalized charge decreases with decreasing distance (or increasing energy), at high energies colour interactions become weaker; this behaviour is well understood in the context of renormalization, and is extremely important because it allows a perturbative treatment of strong interactions.

Electroweak $SU(2)_L \times U(1)_Y$

The electromagnetic an weak interactions are usually treated together as they emerge from the breaking of a $SU(2) \times U(1)$ symmetry, as it will be described in section 1.3; now we'll describe the theory as if the symmetry was unbroken.

[4]There are some results from lattice calculations, models in a reduced number of dimensions, or even using the duality between gravity and quantum field theories (AdS/CFT).

Table 1.1: Particle content of the SM from a gauge point of view, except for the Higgs sector; the three generations of fermions have exactly the same gauge interactions so they are not stated separately

Particle	symbol	$SU(3)$	$SU(2)$	$U(1)$
	$L = \binom{\nu}{e_L}$	1	**2**	$-1/2$
leptons	e_R	1	1	-1
(x3 gen.)	N	1	1	0
	$L = \binom{u_L}{d_L}$	**3**	**2**	$+1/6$
quarks	u_R	**3**	1	$+2/3$
(x3 gen.)	d_R	**3**	1	$-1/3$
gluons	g	**8**	1	0
W bosons	$\vec{W}$	1	**3**	0
B boson	B	1	1	0

Weak isospin $SU(2)_L$, the weak isospin, has three generators and so there is a triplet of gauge bosons ($\vec{W}$ or W^i). Just like in the $SU(3)$ case, the SM fermions fill in the simplest representation of $SU(2)$, the singlet $T = 0$ and the doublet $T = \frac{1}{2}$.

Weak hypercharge $U(1)_Y$ is the abelian group associated to the *weak hypercharge*, whose interactions are mediated by a neutral B boson. The presence of this abelian factor is a concern for theoretical physicists, as it allows for arbitrary values of the particle charges[5] while is experimentally very well proved that electric charge is quantized (i.e. $|q_p/q_e| = 1$ within 10^{-21})

Summary

The particle content of the SM, with their gauge group representation and hypercharges, including the right handed neutrino, are summarized in table 1.1.

1.3 Spontaneous symmetry breaking and the Higgs mechanism

The SM described in 1.2.2, with only gauge interactions, is far from satisfying.

Particle masses The first problem is that all particles must be massless, as there are no gauge-invariant mass terms except for a Majorana mass for the N: to allow for the observed non zero masses, the gauge symmetry must be broken, but an explicit breaking of the symmetry adding extra terms to the Lagrangian is not allowed[6], so spontaneous symmetry breaking must be invoked.

[5] For the SM the requirement of no gauge anomalies constrains the charges to their observed value, but a more compelling explanation for charge quantization would be preferred by many physicists.

[6] Theories with vector particles that are not gauge bosons have problems in the low energy ("infrared") limit

Global symmetries If only gauge interactions are considered, fermions of different families are not directly coupled, the $\bar{\psi}\not{D}\psi$ is invariant under a full $U(3)$ of unitary rotations in the generation (or flavour) space; this includes. a $U(1)$ symmetry for each flavour, so that flavour quantum numbers must be conserved, which is not true for hadronic ones: observed decays like $K \to \pi\pi$ ($s \to du\bar{u}$ at quark level) require a transition from the (c, s) doublet to the (u, d) one, which does not conserve the number of particles of each generation. .

1.3.1 Spontaneous symmetry breaking

The spontaneous symmetry breaking (SSB) is a peculiar feature of infinite dimensional systems like QFTs, in which a symmetric Lagrangian can produce a physics which is not symmetric; it is manifest in a plethora of different fields, from the rotational instability of fluids to condensed matter and solid state theories (superfluids, superconductors), but in this work we'll be focused only on particle physics.

Vacuum states Symmetry breaking can happen in QFT when the vacuum state of the theory is not symmetric: the physical observables are essentially vacuum expectation values of some functions of the fields, $\langle 0|\phi_1(x_1)\dots\phi_n(x_n)|0\rangle$, which won't be symmetric if the vacuum $|0\rangle$ is not symmetric .

The existence of non symmetric vacua is possible because of the infinite degrees of freedom of field theories: in ordinary quantum mechanics, the vacuum state of a system is just one ray of vectors in the Hilbert space, while for QFT the vacuum state is "the Hilbert space itself", as for each possible vacuum $|0\rangle$ a complete representation of the theory can be build in the Hilbert space generated applying polynomials of the fields to the vacuum ($P(\phi)\,|0\rangle$). Different vacuum states providing different physical realizations of the theory are possible as mathematically they are inequivalent representations of the algebra of the theory, which can exist for infinite dimensional algebras like QFT but not for the finite dimensional Von Neumann algebra of ordinary quantum mechanics.

Goldstone theorem This theorem on QFT, which can be proved with full mathematical rigor even beyond perturbation theory, connects symmetries with the existence of massless particles: for each generator of a continuous broken symmetry there must exist a particle of zero mass with the same quantum of the generator.

Goldstone theorem poses problems for SSB in the standard model: if we look for a breaking $SU(2)_L \times U(1)_Y \to U(1)_{EM}$ we should find three massless particles, two of which will be electrically charged, which is in sharp contrast with the observations. Fortunately, there are subtle reasons for which this theorem is not true for the SM: Goldstone theorem applies to *global* continuous symmetries, but not to gauge symmetries; the argument is rather technical, and depends on the Gauge used, so only some hints will be given here: in local gauges the Goldstone particle exist in the theory but is not physical (it is associated to states with negative norm, as happens to time-like polarized photons in QED),

while in gauges with no unphysical particles the charged fields are non local [7], and so the hypothesis of the theorem are no longer met.

The spontaneous breaking of a gauge symmetry leads to a different phenomenology, the Higgs mechanism.

1.3.2 The Higgs mechanism

The scalar QED toy model

The universally used example for the Higgs mechanism is a simple $U(1)$ theory with a charged scalar and a photon, with the Lagrangian

$$\mathcal{L} = -\frac{1}{4}(F_{\mu\nu})^2 + (D_\mu\phi)^\dagger(D^\mu\phi) + \mu^2\phi^\dagger\phi - \frac{\lambda}{4}(\phi^\dagger\phi)^2 \qquad (D_\mu = \partial_\mu - ieA_\mu)$$

The potential depends only on $\rho^2 = \phi^\dagger\phi$, $V(\rho^2) = -\mu\rho^2 + \frac{\lambda}{4}\rho^4$, and has a minimum on the circumference $\rho^2 = \frac{2\mu}{\lambda}$ and not in the origin $\phi = 0$ because of the negative mass term[8]: this means that the vacuum expectation value (vev) of ϕ, $v = \langle\phi\rangle$ which minimizes the potential will be non zero. It is then common to assume that the "correct" perturbative expansion should be done using $\varphi = \phi - v$ a dynamical field; assuming ϕ_0 real, and with the change of variables $\varphi = \rho e^{i\theta}$ (ρ, θ real fields), the covariant derivative of ϕ becomes

$$D_\mu\phi = \left[\partial_\mu\rho + i\rho\left(\partial_\mu\theta - eA_\mu\right) - ieA_\mu(\rho - v)\right] e^{i\theta}$$

Under a gauge transformation $\theta \to \theta + e\Lambda$, $A_\mu \to A_\mu - \partial_\mu\Lambda$, so choosing an appropriate $\Lambda(x)$ we can rotate away θ from the Lagrangian and get

$$\mathcal{L} = -\frac{1}{4}(F_{\mu\nu})^2 + (\partial_\mu\rho)^2 + e^2(\rho - v)^2 A_\mu A^\mu + V(\rho)$$

This Lagrangian appears much different from the original one: now we have one neutral scalar particle (ρ) which interacts with the photon through $\rho\rho\gamma\gamma$ and $\rho\gamma\gamma$ vertexes, but even more important we have a mass term for the photon $e^2v^2A_\mu A^\mu$ and no Goldstone bosons. The degree of freedom that would have been associated to the propagation of the Goldsone boson provide instead the additional (longitudinal) polarization of the gauge boson, now massive. The common saying is that the Goldstone boson is "eaten up" by the gauge boson, which becomes massive.

Standard Model

In the standard model the Higgs field before SSB is a $SU(2)_L$ doublet with hypercharge, Φ; its covariant derivative can be written as

$$D_\mu\Phi = \partial_\mu\Phi \; - \; i\frac{1}{2}g\,\vec{W}_\mu\cdot\vec{\sigma}\,\Phi \; - \; i\frac{1}{2}g'\,B_\mu\,\Phi$$

[7] This can be hinted through Gauss' theorem, which allows to determine the net charge within a region only by knowing the values of the fields on the region's boundary

[8] A 3d plot of the potential looks much like a Mexican hat, and it's universally known under this name

If we write the upper and lower components of Φ separately, ϕ^+ and ϕ (both charged under $U(1)_Y$), and we use the unitary gauge where $\langle\Phi\rangle$ is real, then

$$\Phi = \begin{pmatrix}\phi^+\\ \phi\end{pmatrix} \xrightarrow{SSB} \begin{pmatrix}0\\ v\end{pmatrix} + \begin{pmatrix}\xi^+\\ \xi\end{pmatrix}$$

The terms quadratic in v will provide mass to the gauge bosons

$$\mathcal{L} \supset \frac{1}{8}v^2\left(g^2|W^1|^2 + g^2|W^2|^2 + (-gW^3_\mu + g'B_\mu)^2\right)$$

and the mass eigenstates are

$$\begin{aligned}
W^\pm_\mu &= \frac{1}{\sqrt{2}}(W^1_\mu \mp i\,W^2_\mu) & m_W &= g\frac{v}{2}\\
Z^0_\mu &= \frac{1}{\sqrt{g^2+g'^2}}(g\,W^3_\mu - g'\,B_\mu) & m_Z &= \sqrt{g^2+g'^2}\frac{v}{2}\\
A_\mu &= \frac{1}{\sqrt{g^2+g'^2}}(g\,W^3_\mu + g'\,B_\mu) & m_A &= 0
\end{aligned}$$

Of the four components of Φ only one is left as a dynamical field, a neutral scalar h.

Fermion masses

The same Higgs field that gives masses to the gauge bosons can also provide masses to the fermions: gauge invariance permits the following Yukawa terms to appear in the SM Lagrangian

$$\mathcal{L} \supset \lambda_u\bar{Q}\cdot\Phi^\dagger\,u_R + \lambda_u\bar{Q}\cdot\Phi\,d_R + \lambda_e\bar{L}\cdot\Phi^\dagger\,e_R + \lambda_\nu\bar{L}\cdot\Phi\,N$$

The λ_x, 3×3 matrices because of three generations, become mass matrices $m = v\lambda$ when Φ acquires a vev; the last term provide neutrino masses, but otherwise plays a negligible role in SM physics.

Non minimal Higgs sectors

Some simple extensions of the SM have two Higgs boson doublets H_1, H_2, both of which acquire a non zero vacuum expectation value; each boson interacts with a different group of fermions, i.e. H_1 give mass only to u quarks and H_2 to d quarks and leptons. As there are only three gauge bosons to provide mass to, and 8 real degrees of freedom, 5 Higgs particles remain: it can be easily derived that two are charged, $h^\pm$ and three neutral (h, H, A).

Mass eigenstate and symmetries

Usually one can rotate the basis for the three generations to work in the mass eigenstates, at the price of mixing matrices appearing in the gauge interaction terms. If there are no neutrino masses then there is only one unitary mixing matrix, V_{CKM}, all the others are non physical and can be rotated away redefining the fields.

The global symmetry of the theory is now reduced as generations are no longer identical. With no neutrino masses, the total symmetry is $U(1)^4$: one from the global phase of all quarks, barion number conservation, and one for each lepton flavour (which are separately conserved). If neutrino masses are added, but with no Majorana mass for N, it is only $U(1)_B \times U(1)_L$, the total lepton and barion number (L, B) are conserved; in the most general case another phase is constrained by the additional $m_N \bar{N}^c N$ term, and L is no longer conserved.

Chapter 2

Introduction to hadronic physics

2.1 Partons in hadrons

At very low energies protons and neutrons behave like point-like particles, but at energies above $\sim 10\,\text{GeV}$ a radically different picture appears, in which hadrons are seen as bunches of loosely bound "partons". These have been observed in deep inelastic scattering of electrons or neutrinos on proton targets, from hadron production in e^+e^- colliders and especially in hadronic colliders.

Deep Inelastic Scattering If a high energy electron (or neutrino) collides with a stationary proton, the internal structure of the proton is undone, and in the final state there will be the electron and some hadrons. By measuring the momentum and flight direction of the outgoing electron it is possible to determine the amount of energy and momentum transferred in the scattering, and measure the proton form factors[1]. In inelastic collisions the two parameters are independent, but experimentally the proton form factors are found to be function of only one variable

$$x = \frac{Q^2}{2P \cdot q}$$

where P is the proton four-momentum, q the transferred four-momentum, and by convention $Q^2 = -q^2$. This scaling law, originally proposed by Bjorken, can be proved under the assumption that the proton is composed by "free" point-like fermions with momentum $p_i = z_i P$ collinear to the one of the proton: in this model, the form factors are functions of x multiplied by constant factors and by the probability densities $f_i(z)$ of finding partons of type i with a fraction z of the proton momentum.

Parton density functions By observing the deep inelastic scattering of electrons and neutrinos at different energies on proton and neutron targets, it is

[1] Form factors are the coefficients of the most general parametrization of the electron-proton scattering amplitude, functions of all the Lorentz invariant scalars in the process.

possible to extract the probability densities $f_i(x)$ of finding a parton i with x momentum fraction. These densities are universally known as parton density functions (PDFs).

It appears clearly that within a proton or neutron there are not just the three quarks naïvely expected (*valence quarks*), but also a "sea" of q and $\bar{q}$ partons with low x, which have very similar distributions in all baryons, almost independent from the flavour for light quarks (uds); PDFs for the valence quarks and sea quarks are very different, as the latter are abundant at low x but negligible at $x \sim 1$, while valence quarks are peaked for larger values of x. A plot of the PDFs for quarks within as proton will be shown in figure 2.1.

There is also another striking fact: the average fraction of the barion momentum carried by all quark constituents together, obtained integrating over all quark flavour PDFs, is not 1 but only about one half: this means that the other half of the barion momentum is carried by the gluons, which are invisible in DIS experiments as they undergo no electroweak interactions.

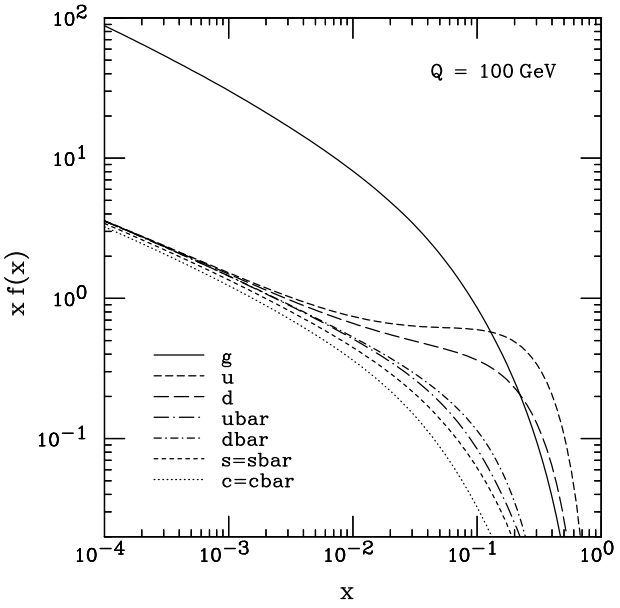

Figure 2.1: Parton density functions for the proton, from the CTEQ6M NLO fit[CTEQ] at $Q^2 = (100\,\mathrm{GeV})^2$

Hadronic collisions Within the parton model, a collision between hadrons is seen as the interaction between partons; if i, j label the parton types, and x_i, x_j, the longitudinal fractions of the hadron momentum carried by them, the cross section can be expressed as

$$\sigma(pp \to X; s) = \sum_{i,j} \int dx_i dx_j f_i(x_i) f_j(x_j) \hat{\sigma}(i + j \to X; \hat{s})$$

where $\hat{\sigma}$ is the elementary, partonic, cross section, and $\hat{s} = x_i x_j s$ is the square of the energy available in the center of mass frame of the two partons (this equation is often called Factorization Theorem).

Gluon PDFs Collisions between hadrons can be used to measure directly the gluon PDF[2]; the g distribution is similar to that of sea quarks, peaked at low x, but gluons are more abundant. With respect to $q\bar{q} \to q\bar{q}$, $qq \to gg$, $qg \to qg$, the gluon gluon scattering $gg \to gg$ is also increased by large *color factors*, related to the larger multiplicity of gluon states, so that it is the dominant process in in pp or $p\bar{p}$ interactions at low x.

PDF dependence on Q^2 If Bjorken scaling is tested on a large energy range, the accord much less satisfactory; this is not a surprise, as we know that QCD interactions are sensitive to the scale through $\alpha_s(Q^2)$, and we also expect processes like gluon splitting ($g \to q\bar{q}$) to be influenced by the energy scale. A complex set of differential equations, by Altarelli and Parisi[AP], can be used to calculate the evolution of PDF as a function of Q^2; for increasing Q^2, valence quarks have their maximum pushed towards lower x, while sea quark and gluon distributions increase much for small values of x.

A plot of the gluon PDF for different Q^2 can be found in figure 2.2, clearly showing this behaviour.

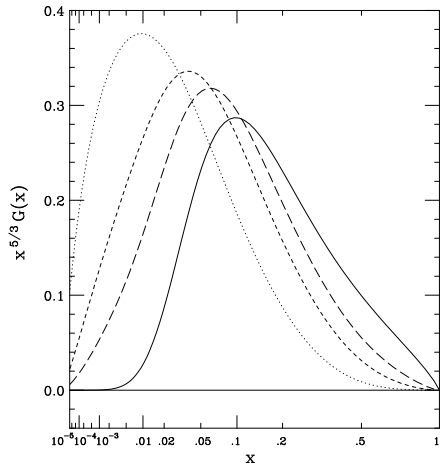

Figure 2.2: Gluon PDF from the CTEQ6M fit, at different Q^2 scales: $Q = 1\,\text{GeV}$ (solid), $2\,\text{GeV}$ (long dashes), $5\,\text{GeV}$ (short dashes), and $100\,\text{GeV}$ (dotted).

The overall emerging picture is: within hadrons there are point-like particles, which have only soft interaction among themselves, without large momentum transfers; when a high energy collision takes place, only one parton is involved in the process, and it behaves like a free particle. After the collision, the scattered parton undergoes soft interactions with the other constituents of the hadrons, which will lead to hadronization, but this won't alter dramatically the result of the hard interaction.

Uncertainties on the PDFs As PDF parameters are fitted from experimental data, they are affected by uncertainties which will propagate to any cross

[2]This is not the only way; inclusive photoproduction $\gamma N \to \psi X$ of the ψ particle (a $c\bar{c}$ bound state) can also be used

section calculated using those densities; these uncertainties affect mostly the gluon PDF, for which less measurements are available[3] and evolution through a larger Q^2 range is needed in order to reach the energy scale of the interactions at LHC, while the densities for valence quarks are more constrained.

2.2 Radiative corrections

Radiation in QED Radiative corrections are known since the first developments of quantum electrodynamics (QED): in addition to the leading order process, corrections can be calculated both for alike processes when additional particles are produced (i.e. in $e^+e^- \to \mu^+\mu^-$ all the leptons can radiate *real* photons), or for the same process including additional the contributions from the exchanges of particles (i.e. in the same process an additional *virtual* photon can be emitted by the e^- and absorbed by the μ^+, without changing the final state). All corrections are expected to be suppressed by powers of the coupling constant α.

Naïve calculations of this corrections would lead often to divergences for large momenta of particles in the inner lines (ultraviolet divergences), but these can be treated correctly through the renormalization procedure obtaining finite results.

Additional divergences arise from the infrared regime, such as the emission of nearly collinear radiation; these divergences cancel out if one restrict the computation to non collinear photons (i.e. those above some energy threshold), and if one considers both the contributions from additional inner lines and from radiation.

Soft radiation In the method described before, radiative corrections are assumed to be computed "exactly", that is with the correct matrix element for final states containing all the radiated particles, which require lengthy computations of $2 \to n$ Feynman diagrams.

For what concerns the radiation of *soft* particles, with energies much smaller than the hard process scale, approximations can be made factorizing out the radiation step, which allow to write the cross section for the radiation of an additional particle as the normal cross section times a correction factor depending only on the momentum of the radiated particle.

This approximation allows to easily compute the corrections for any number of radiated particles, as long as all these particles are soft.

Large logarithms The correction for a single soft photon emission are numerically large due to logarithmic enhancements in the form $\log(-q^2/m^2)\log(-q^2/\mu^2)$ where $-q^2$ is the hard process scale, and m^2, μ^2 are infrared cutoffs: m^2 is given by the radiating particle masses; μ^2 is an auxiliary, non physical, infrared cutoff which will be removed later when adding together corrections from real and virtual soft photons and replaced by the minimum energy threshold E for detecting soft photons[4].

[3] In particular, it cannot benefit from the results from HERA, an asymmetric *ep* collider, as gluons don't have electroweak interactions

[4] A threshold is necessary for *defining* the final state with the additional radiated photons.

Because of this, corrections for multiple radiated photons must be taken into account. Nevertheless, the $(\alpha \log \log)^n$ corrections can be resummed for any number of soft photons with total energy below E obtaining a finite (and bounded) cross section correction proportional to $\exp(-k \log(-q^2/m^2) \log(-q^2/E^2))$; this resummation procedure is called Leading Log (LL) approximation.

Radiation in QCD In QCD the coupling constant is larger ($\alpha_s/\alpha_{em} \gtrsim 10$ at $q^2 \sim m_Z^2$), and color factors from the high multiplicity of states enhance the importance of radiative corrections; meanwhile, hadronization provides a natural infrared cut-off, as particles radiated at small angles will end up in the same jet of the mother particle without being resolved independently.

Because of these factors, LL corrections provide a good description of the radiation of additional soft quarks and gluons, which appear experimentally as additional soft jets.

Parton showers Within Monte Carlo simulations, a procedure called *showering* and based on LL computations is often used: radiative corrections are done by through splitting probabilities $P(a \to b + c)$ which contain the factorized radiative corrections for processes like $q \to q + g$, $g \to q\bar{q}$ which are used to attach radiative correction to incoming particles (initial state radiation, ISR) or outgoing ones (final state radiation, FSR), and the procedure is iterated on all the leaves obtained from the splitting.

With respect to analytical LL computations, in parton showers some "higher order" corrections are taken in account, such as the finite momentum carried away by radiated particles or color coherence effects, so that the final results are in good accord with data as long as only soft radiation is concerned.

Hard radiation and matching In some cases the hard tails of the radiation are interesting, such as when signal process (i.e. $qb \to tq' \to \ell\nu bq'$) process has to be resolved against an inclusive background which naturally produces less jets (i.e. inclusive W production) and is important only when additional hard jets are produced by radiation.

In this case parton showers results are unsatisfactory, as the correction for soft radiation has much lower hard tails than the correct ones, and computation with explicit matrix elements for the final state with n radiated jets are necessary.

"Exact" computation can be performed only up to some number of radiated jets, and so the corrections for additional soft jets must be performed anyway, but with particular care of avoiding double-counting between the events with additional "hard" jets from matrix element and additional "soft" jets from showering; this *matching* procedure between matrix elements and parton is difficult, but can be performed, and is included in some Monte Carlo simulations specifically targeted to $2 \to n$ processes (e.g. AlpGen).

2.3 Hadronization

Because of confinement, partons scattered or produced with large p_T with respect of the parent hadron can't be emitted as free particles; a *jet* of collimated

hadrons is instead produced. This process can't be described through perturbative QCD, as it happens in the strong coupling regime; because of this, phenomenological models are used, with parameters tuned to reproduce the experimental results.

Lund string model

Principle This model, often used in Monte Carlo simulations[5], is based on the fact that the large distance quark interactions can be interpreted through a "inter-quark" potential which grows linearly with the separation $V(r) \propto r$; this form was suggested by spectroscopy of heavy quark bound states and the approximate relation $J = a + bM^2$ between hadron spins and masses. Such a potential can be interpreted as if quarks where bound by a "string" with constant energy per unit length.

The basis Let us consider, for simplicity, a final state with only two back-to-back quarks, such as what could be produced in $e^+e^- \to q\bar{q}$. In this model, the string between the two quarks is stretched as the two fly away in opposite directions, while the interquark force decelerates them; a $q\bar{q}$ pair may be formed at any point of the string, breaking it into two parts which will then evolve independently. A probability is assumed for the breaking of the string replacing a segment of it with $q\bar{q}$ pair uniform in time and position and independent on the string length, proportional to a "quantum tunneling" factor $\exp(-\pi m^2/\kappa)$, where m is the quark mass and κ the string tension, and that the new pair has the same energy-momentum of the piece of string which is replaced.

When a string piece becomes short enough, it might survive without breaking until the two quarks have been fully decelerated by the interquark force and the string starts shrinking and then undergoes oscillations; at this time, usually, the string is replaced by a hadron and the process is halted.

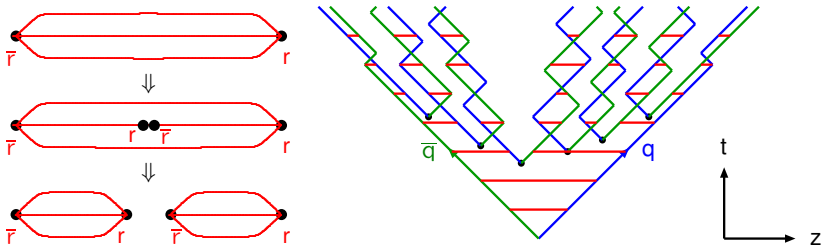

(a) String splitting (b) String dynamics

Figure 2.3: Two simplified pictures describing the evolution of color strings in the Lund showering[PYTHIA]

Refining the algorithm The description so far has been unidimensional, but a transverse momentum can also be assigned to the new $q\bar{q}$ pair, taken from

[5]The Lund string model is used in the very popular PYTHIA generator

a phenomenological distribution (usually $\propto \exp(-{p_T}^2)$ obtained through the replacement $m^2 \to m^2 + {p_T}^2$), and the same is done for quark spin states.

Gluons are handled differently: not endpoints of a string, but "kinks" in a string which can move within it, just as if each gluon were an inseparable $q\bar{q}$ pair bond together, which connects two different strings.

Because of the e^{-m^2} suppression, only u, d and less frequently s quarks can be produced in fragmentation[6], which provides a satisfactory treatment of jets initiated by light quarks or gluons.

Fragmentation of heavy quarks within the string model is taken into account by a different probability density, to account for harder quark fragmentation. Other fragmentation models, specific to heavy quarks, have been proposed and are often included in generator programs.

2.4 Heavy quark fragmentation

Jets initiated by quarks (c, b) often contain a flavoured meson (D, B) which carries a large fraction of the quark momentum. In other terms, the *fragmentation function* $D_Q^h(z)$, the probability that a hadron h is found in the fragmentation products of the quark Q with a longitudinal momentum fraction z, is peaked at high values of z if h is a $Q\bar{q}$ meson.

There are many phenomenological explanations and models of this *hard fragmentation* of quarks; here we will just describe briefly the Peterson model, which is very simple and provides a satisfactory description of experimental data.

Peterson fragmentation Peterson's idea was to assume that the amplitude of the process is proportional to an energy denominator, like in time dependent perturbation theory, $(E_i - E_f)^{-1}$, and that everything else can be treated as a constant except for a z factor from phase space. As a result, if $\vec{p}$ is the momentum of Q, and approximating $m_Q \simeq m_h$ one gets

$$\Delta E = \sqrt{m_Q^2 + p^2} - \sqrt{m_Q^2 + z^2 p^2} - \sqrt{m_q^2 + (1-z)^2 p^2}$$

which can be expanded for large p/m_Q obtaining

$$\Delta E \propto 1 + \frac{1}{z} + \frac{\epsilon_Q}{1-z}$$

where $\epsilon_Q = (m_q/m_Q)^2$. The fragmentation function is then

$$D_Q^h(z) \propto \frac{1}{z}\left[1 + \frac{1}{z} + \frac{\epsilon_Q}{1-z}\right]^{-2}$$

This function is peaked at $z \sim 1 - 2\epsilon_Q$, with a width $\sim \epsilon_Q$.

[6]The probability of producing a charm quark, instead, is 10^{-11}.

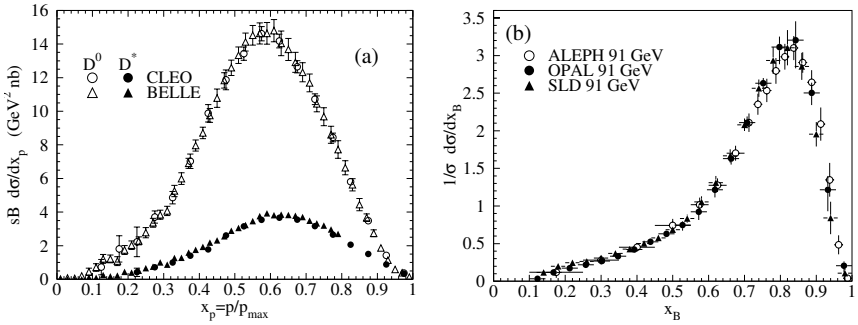

(a) Charm quark

(b) Bottom quark

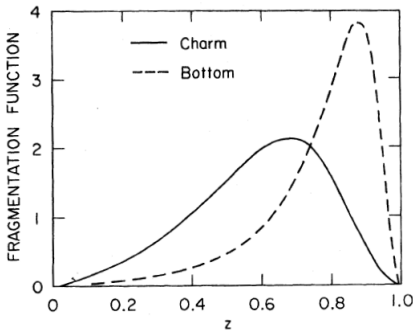

(c) Peterson $D(z)$

Figure 2.4: The measured charm and bottom quark fragmentation functions compared with the $D(z)$ from Peterson, with $\epsilon_c = 0.15$ and $\epsilon_b = (m_c/m_b)^2\epsilon_c \simeq 0.016$.

Chapter 3

Top quark physics

3.1 Introduction

The top quark is by far the heaviest of the SM fermions, it has a Yukawa coupling $\lambda_t \simeq 1$, which makes top quark physics much different from the one of lighter quarks.

As $m_t > m_W + m_b$ the top quark can decay in a real W, so his width is $O(\alpha)$ instead of $O(\alpha^2)$; thanks also to a huge phase space for decay products and $V_{tb} \sim 1$[1] the decay width is $\Gamma_t \simeq 1.4\,\mathrm{GeV}$. Having $\Gamma \gg \Lambda_{QCD}$ the soft interactions from hadronizations can be neglected, as the quark decays before forming hadrons; this means that observables like the spin which are normally "washed out" by hadronization can be measured for the top quark (see section 3.3).

Because of its strong coupling, the top quark plays a big role in the one loop structure of the SM (see section 3.2): the value of top quark mass is a critical parameter in precision tests of the Standard Model

The top quark is also important for the search of flavour-changing neutral currents (FCNC) and hints on beyond SM physics.: when the "unknown physics" is integrated out, the SM-like effective field theory has additional terms of dimensionality $d > 4$ which are naturally suppressed by negative powers of the scale Λ at which unknown physics live; the corrections to SM observables are then $O((q/\Lambda)^n)$ where q is some energy or mass scale involved in the process, and their possible effects on the top quark should be much bigger than those on light quarks.

If more than three generations exists, the value of V_{tb} is almost completely unconstrained; it is not experimentally feasible to measure it through the top quark width, but it would be possible by studying the production of single top quarks, such as through $u\,\bar{d} \to t\,\bar{b}$, for which $\sigma \propto |V_{tb}|^2$.

[1] This comes from V_{CKM} unitariety, and is not true if there are more than three generations

As most of this thesis work will be dedicated to physics of single top quark, only a short review of the other topics of top physics will be given.

3.2 Top quark in the one loop SM

The LEP experiment was devolved mostly to electroweak physics, and the top quark was too heavy to be directly produced, but it was anyway possible to constrain its mass within 10%, as the one loop corrections to SM observables are very sensitive to the top mass.

Now that top quarks can be produced at Tevatron, and would be produced copiously at LHC, the directly measured value of the top quark mass can be introduced as an additional data in the fit of the Electroweak Precision Observables (EWPO); this allows to constraint the allowed values for the Higgs boson mass, if the SM is assumed to be true, or test if the data are compatible with some BSM scenario with greater accuracy. A sample plot of the allowed regions in the (m_W, m_t) for the SM and its supersymmetric extension, and the current experimental values, are shown in figure 3.1.

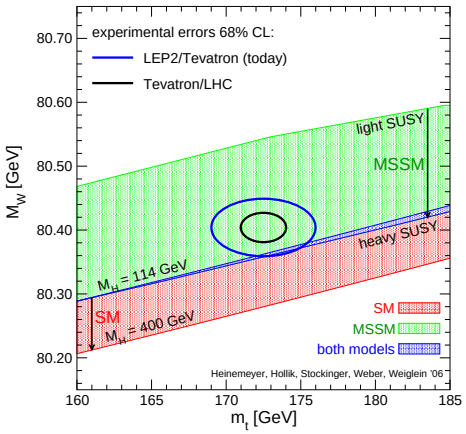

Figure 3.1: Measured values of m_W, m_t with the current accuracy and the one expected in the future Tevatron and LHC, compared to the values allowed in SM and MSSM (minimal sumersymmetric Standard Model)

3.3 Top quark spin

3.3.1 Spin correlation in $t\bar{t}$ production

The top pair production does not yield polarized quarks, but the spins of the two members of the pair are anyway correlated, as they must sum up to the gluon spin.

The top quark spin can be estimated by using the angular distribution of the decay products in $t \to Wb \to \ell\nu b$ or $t \to Wb \to q\bar{q}'b$ decays, which is given by

$$\frac{1}{\Gamma}\frac{d\Gamma}{d\cos\theta} = \frac{1}{2}(1 + \kappa\cos\theta) \tag{3.1}$$

The values of κ for different particles are: 1 for leptons and the light antiquark $\bar{q}'$, ± 0.41 respectively for the W and the b quark, -0.31 for the neutrino or the light quark q; as it is almost impossible to tell the difference between a q and a $\bar{q}$ initiated jets, the value of κ can also be calculated for "the lower energy" light quark in the event, and the result is 0.51.

If semileptonic quark decays are considered, in which the full kinematics can be reconstructed and the signal purity is high, one can study the double differential distribution of the decay products of the two quarks in the $t\bar{t}$ center of mass frame. If q is either the b quark or the lower energy light quark, an angular distribution

$$\frac{1}{N}\frac{d^2N}{d\cos\theta_\ell\, d\cos\theta_q} = \frac{1}{4}(1 - \mathcal{A}\kappa_\ell\kappa_q \cos\theta_\ell \cos\theta_q) \tag{3.2}$$

is expected, with $\mathcal{A} \simeq 0.35$ for both choices of quark.

Measurement of this quantity at LHC should be feasible, extracting the value of $\mathcal{A}$ with a $\sim 20\%$ relative accuracy with $10\,\mathrm{fb}^{-1}$[CMS NOTE 2006/111].

3.3.2 Single top polarization

Single top quark production is allowed only through weak interactions, in which the $V - A$ structure causes the produced quark to be of left chirality; the top quark is not massless or ultra-relativistic, so chirality is not the same as helicity, but nevertheless large values of the top quark polarization can be achieved if the correct reference frame is chosen[Mahlon].

The easiest mode for top polarization studies is t channel, in which a polarizations above 90% are expected in the direction of the "spectator" light quark. If leptonic decays of the W boson are selected, a measurement of the top quark polarization can be achieved using the angular distribution of the lepton with respect to the top quark spin, given by equation (3.1), with $\kappa = 1$.

In order to measure the polarization the top quark momentum must be reconstructed, but this is possible in by imposing the W mass constraint to reconstruct the longitudinal momentum of the neutrino, while the transverse component is fixed by the energy conservation in transverse plane.

Studies about measuring the top quark polarization at LHC have been done within the ATLAS collaboration, and can be found in section 18.1.6.7 of [Atlas].

3.4 Single top quark production

Single top production is possible only through electroweak charged current interactions. In particular, three different channels can be defined, by the virtuality of the W boson: t channel is when the q^2 is space-like, and a W boson is exchanged between a b "sea" quark and another, usually light, quark (t channel); s channel is when a $u\bar{d}$ pair annihilates into $t\bar{b}$ through an intermediate W^* with $q^2 \geq (m_t + m_b)^2$; associated tW production, where the W boson is real.

All three processes involve a Wtb vertex, and so the cross sections are quadratic in $|V_{tb}|$, so that a measure of the cross section will constrain the

element of V_{CKM} without assuming three fermion generations; the other constraint on $|V_{tb}|$ from the unitarity relation $|V_{tb}|^2+|V_{ts}|^2+|V_{td}|^2 = 1$, which gives $|V_{tb}| \simeq 0.993$, is dependent on the number of families, and it is almost nullified if a fourth generation is allowed, becoming $0 < |V_{tb}| \leq 0.993$ [Vtb].

3.4.1 t-channel production

The t channel production is characterized by the LO process $q\,b \to q'\,t$, as depicted in diagram 3.2(a); for this process, the b quark is assumed to be already present within the "sea", eventually arising from a resummation of Feynman diagrams in which a gluon undergoes collinear $g \to b\bar{b}$ splitting.

NLO corrections A NLO correction can be done taking into account the process in which the b quark is produced by a non collinear gluon splitting (diagram 3.2(b)), with the required care to avoid double-counting. The full NLO cross section has been calculated in [Stelzer], including also terms from the extra gluon exchanges, gluon radiation and gluon splitting $g \to q\bar{q}$ for the non b quark; corrections are of order α_S or $1/\ln(m_t^2/m_b^2)$ for the $g \to b\bar{b}$ correction[2].

Asymmetry t vs $\bar{t}$ The production cross section is different for t and $\bar{t}$ production, as a top quark can be produced through $q\,b \to q'\,t$ if q is either a up-type quark or a down-type antiquark, while the anti-top requires an up-type antiquark or a down-type quark; up quarks are more abundant than down quarks in protons, while the densities for all light anti-quarks are equal, so the production of a top quark is favoured with respect to the production of an anti-quark: the NLO cross sections are 153 pb and 90 pb respectively.

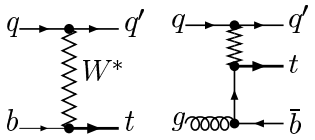

(a) LO (b) $g \to b\bar{b}$

Figure 3.2: The leading order process for t channel single top production, and the initial gluon NLO correction

3.4.2 Associate tW production

Associate tW production can proceed through s or t channel diagrams, as shown in figure 3.3. In both cases the initial partons are a gluon and a b quark; as the parton density function for the b and $\bar{b}$ quarks are the equal, the cross section for tW^- and $\bar{t}W^+$ are equal. As one of the vertexes is from strong interaction, $\sigma \propto \alpha_S\alpha_W$ instead of α_W^2; nevertheless the cross section is smaller than t channel

[2]This is because the process with the initial state b quark is obtained by resummation of collinear splittings, which are order α_S but enhanced by the large logarithm $\ln(\mu^2/m_b^2)$ ($\mu \sim m_t$); the non collinear splittings are again order α_S but don't have the logarithmic enhancement.

single top, because the required momentum fraction x is larger, and the cross section is proportional to $1/s$ instead of $1/m_w^2$.

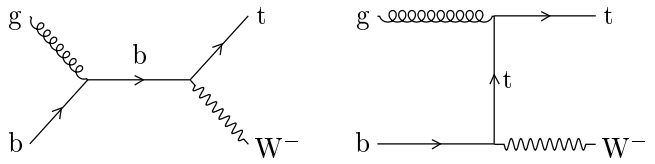

(a) s channel tW (b) t channel tW

Figure 3.3: The two LO diagrams for associated tW production.

NLO Next to leading order corrections to tW process pose non trivial problems on the definition of the process: if the b quark for $gb \to tW^-$ is produced in a $g \to b\bar{b}$ splitting, the final state $W^-t\bar{b}$, which is the same as for $t\bar{t}$ production except that the top ($W^-\bar{b}$) is off mass shell; this means that $t\bar{t}$ and tW mix at NLO, and interference terms must be taken into account. A sample diagram among those producing this mixing is shown in figure 3.4.

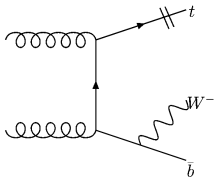

Figure 3.4: A sample NLO diagram which mixes tW and $t\bar{t}$ at NLO: the top quark indicated by the cut line is the one expected from tW production, while the $W^-\bar{b}$ system can be interpreted both as the W from the tW process plus a radiated $\bar{b}$ quark, or as the second top quark in a $t\bar{t}$ event, if $m(W^-\bar{b}) \sim m_t$.

Different prescriptions have been proposed in order to obtain a gauge invarian and positive definite cross section fot tW production alone at NLO. A suitable one is to impose an upper bound to the p_T of $\bar{b}$ quark introduced in the NLO cross section [Campbell], which yields a NLO cross section of 60 pb when both tW^- and $\bar{t}W^+$ are considered[3].

3.4.3 s-channel production

Single top production in the s channel is mediated by an off-shell W boson with $q^2 \geq (m_t + m_b)^2$. The process is remarkably simple, $q\bar{q}' \to W^* \to t\bar{b}$, as illustrated in the diagram 3.5; q can be any up-type quark and $\bar{q}'$ any down-type antiquark, but the dominant contribution is from $u\bar{d} \to t\bar{b}$ as they are more abundant than the heavier quarks.

[3]Another proposed definition is to leave out all the $\alpha_S^2\alpha_W$ diagrams, which will be attributed to the $t\bar{t}$ process[Maltoni], which gives similar results for σ.

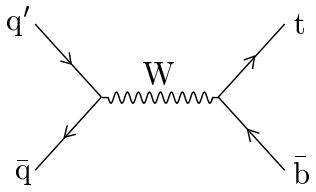

Figure 3.5: Leading order diagram for s-channel single top production.

As light quark PDFs within the proton are well known, especially for large values of x, a much smaller uncertainty is expected from this source, which makes this channel potentially the most attractive for a precision $|V_{tb}|$ measurements. In addition, parton luminosity can be constrained by measuring the abundant $q\bar{q} \to W^* \to \ell\nu$ process, even if the presence of the neutrino does not allow to reconstruct the full kinematics and give a complete measurement of the PDFs involved.

The cross section at leading order is only 10 pb at LHC, one or two orders of magnitude below the dominant backgrounds ($t\bar{t}$ and t channel single top). At Tevatron the situation is somewhat better, as $\sigma(t\bar{t})/\sigma(sch.) \sim 7$ because of the higher parton luminosity for $q\bar{q}$ processes in $p\bar{p}$ colliders with respect to pp ones, and the larger x values needed which suppress processes with gluons in the initial state.

NLO Corrections to the production cross section have been calculated up to order α_S and $\alpha_W m_t^2/m_W^2$ [Smith]. The first corrections arise from initial and final state QCD radiation; the two processes don't interfere at order α_S, as the $q\bar{q}$ pair which does not radiate the gluon is in a colour singlet state while the other is in the colour octet state. The other correction, given by Yukawa interaction, comes from loops containing the Higgs boson or the longitudinal polarization of the electroweak bosons.

The uncertainty on the NLO calculation is $\pm 6\%$ including contributions from higher orders, estimated through the variation of the factorization and renormalization scale, and uncertainties from parton density functions.

The value of the cross section is strongly dependent on the top quark mass, so that $\delta\sigma/\sigma \simeq 4.4\,\delta m_t/m_t$. With the accuracy expected by the combined results of Tevatron and the first years of LHC, $\delta m_t/m_t \simeq 2\,\text{GeV}$, the cross section will be affected by an additional $\pm 5\%$ uncertainty from this source.

Part II

LHC and CMS

Chapter 4

Large Hadron Collider

The Large Hadron Collider (LHC) is a circular $p\,p$ collider designed to address physics up to the TeV scale.

4.1 Preceding accelerators

Before LHC the two main accelerators for high energy physics where the Large Electron Positron (LEP) and the Tevatron at Fermilab.

LEP LEP was a circular $e^+\,e^-$ collider designed to study electroweak physics and probe possible new physics at the Fermi scale. At first it operated at $\sqrt{s} \sim 90\,\mathrm{GeV}$, the Z^0 mass peak; later, in the LEP2 phase, the energy was raised to $\sqrt{s} \sim 200\,\mathrm{GeV}$, at a luminosity of $10^{32}\,\mathrm{cm}^{-2}\mathrm{s}^{-1}$. The extremely clean environment allowed for precision physics, as the measurement of the one loop correction to electroweak observables, obtaining indirect limits on the top quark mass ($178.1^{+10.4}_{-8.3}\,\mathrm{GeV}$, [PDG]) and on the Higgs boson mass ($114^{+69}_{-45}\,\mathrm{GeV}$, $m_h \leq 260\,\mathrm{GeV}$ at 95% CL, [PDG]). Unfortunately there was no "new physics" in the accessible energy range, and even for the direct Higgs boson only an upper limit was obtained, $m_H \geq 114.4\,\mathrm{GeV}$[PDG], mostly from the $e^+\,e^- \to Z\,H$ channel.

Tevatron Tevatron is a circular $p\bar{p}$ collider operating at $\sqrt{s} \sim 2\,\mathrm{TeV}$, and luminosity $6 \cdot 10^{31}\,\mathrm{cm}^{-2}\mathrm{s}^{-1}$ (Run II). Among its achievement was the first observation of the top quark[TopQuark] and measurement of its mass ($m_t = 172.5 \pm 2.3\,\mathrm{GeV}$ [TEWG]); it has also observed B_s oscillations, and found exclusion limits for many beyond SM scenarios (supersimmetry, extradimensions, ...). The current integrated luminosity is about 1 fb^{-1}, and the expectations for the end of Run II (2009) are 8 fb^{-1}, which could allow for 3σ evidence of a light Higgs boson ($m_h \lesssim 120\,\mathrm{GeV}$) or a significant improvement of the LEP2 limit ($m_h > 185\,\mathrm{GeV}$ at 95% CL)

4.2 The LHC project

In order to improve the LEP and Tevatron results it was necessary to increase both energy and luminosity.

Energy losses Synchrotron radiation prevents constructing a LEP-like collider at $\sqrt{s} \sim 1\,\text{TeV}$: energy loss scales as γ^4, and with 27 km circumference already at 160 GeV 10% of the particle energy would be lost in just one revolution; for protons this loss is reduced by $(m_e/m_p)^4$ and is thus neglegible even for energies of some TeV. As the technologies for building a linear $e^+\,e^-$ collider at TeV scale were yet unavailable[1], and excavation of a 700 km circular accelerator would have hardly been possible, the choice of a proton machine was almost forced.

Beam energy The design energy for LHC, $\sqrt{s} \simeq 14\,\text{TeV}$ has been dictated by the radius of the LEP tunnel and the maximum bending magnetic field that was foreseen to be available (8.3 T). Protons are composite particles, and so the energy available in the parton-parton scattering will often be much smaller than 14 TeV; for a collision among valence quarks, which carry the largest fraction of the proton energy, $\frac{1}{6}\sqrt{s}$ is a good estimate[2], so that the real physics reach of LHC is $\sim 2\,\text{TeV}$.

Luminosity Increasing luminosity much above the Tevatron values is necessary to allow for the observation of processes with tiny cross sections; this will be achieved by increasing the bunch crossing rate and the number of particles per bunch while reducing the bunch size.

Choice of pp In order to achieve a luminosity of $10^{34}\,\text{cm}^{-2}\text{s}^{-1}$ it was necessary to use only protons, which are much easier to handle than antiprotons. As a consequence the average energy available in a $q\bar{q}$ annihilation will be smaller, because the $\bar{q}$ cannot be valence quarks; most of the process of interest are anyway dominated by interaction with at least one gluon or a b quark in the initial state (i.e. $g\,g \to h$), which can be found with the same probability in a p or a $\bar{p}$, and so this drawback is sustainable.

4.3 LHC running cycle

Injection Protons pass through a long chain of accelerators before begin injected into LHC: the first steps are a linear accelerators (LINAC), then a Booster ring (PSB); next, bunches are accelerated to 26 GeV in the Proto Synchrotron (PS), and trains of bunches are fed into the Super Proto Synchrotron (SPS) where they are further accelerated to 450 GeV to be injected in the LHC; the whole transfer system is already complete and tested.

Acceleration and squeezing Once inside LHC the protons are accelerated by RF cavities up to 7 TeV; in the meantime, the beam is also squeezed in the transverse plane to increase luminosity.

[1] Such a machine, the International Linear Collider (ILC), might be built around year 2015[ILC]

[2] There are three valence quarks, and half of the proton momentum is carried by gluons

Beam lifetime Due to the high luminosity, a large number of "minimum bias" events happen at every bunch crossing, reducing the number of available protons and degrading the overall beam quality; in addition, protons can interact with the gas of particles inside the beam pipe, and the packets themselves spread because of intra beam interactions: combining all these effects, the luminosity lifetime of the beam is 15 h, of which only the first 10 h will be used for physics.

4.4 LHC running parameters

Table 4.1: LHC running parameters

	Pilot runs	Physics start	**Low $\mathcal{L}$**	**High $\mathcal{L}$**
Number of bunches	43–156	936	2808	2808
Protons per bunch $[\cdot 10^{10}]$	1–4	4	4	11.5
Luminosity $[\mathrm{cm}^{-2}\mathrm{s}^{-1}]$	0.3-20$\cdot 10^{30}$	10^{32}	$2 \cdot 10^{33}$	10^{34}
Integrated lum.	$10\,\mathrm{pb}^{-1}$	$1\,\mathrm{fb}^{-1}$	$10\,\mathrm{fb}^{-1}$/y	$100\,\mathrm{fb}^{-1}$/y
Year	2007	2008	2008	2010

Chapter 5

The CMS detector

5.1 Overview of the CMS detector

The CMS detector has a roughly a cylindrical shape, 22 m long, with an outer radius of 7 m. It is divided into two regions: barrel ($|\eta| \lesssim 1.4$)[1], where subdetectors are layered at increasing R, and endcaps where layers are placed at different values the of the z coordinate.

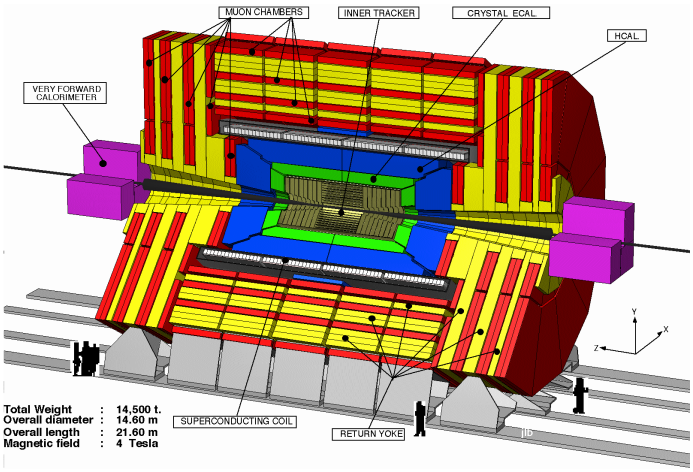

Figure 5.1: Longitudinal view of the CMS detector.

Tracker Proceeding from the interaction point outward, the first subdetector encountered is the tracker; silicon pixels and strips are used to accurately measure charged particle tracks inside the 4 T magnetic field. The tracker coverage extends up to $|\eta| \leq 2.5$.

[1] η is the pseudorapidity, $\eta = -\log\tan(\theta/2)$; this variable is often used at colliders as it coincides, in the ultra-relativistic limit, to the rapidity $y = \frac{1}{2}\log((E+p_z)/(E-pz))$ that is additive for boosts along the z axis

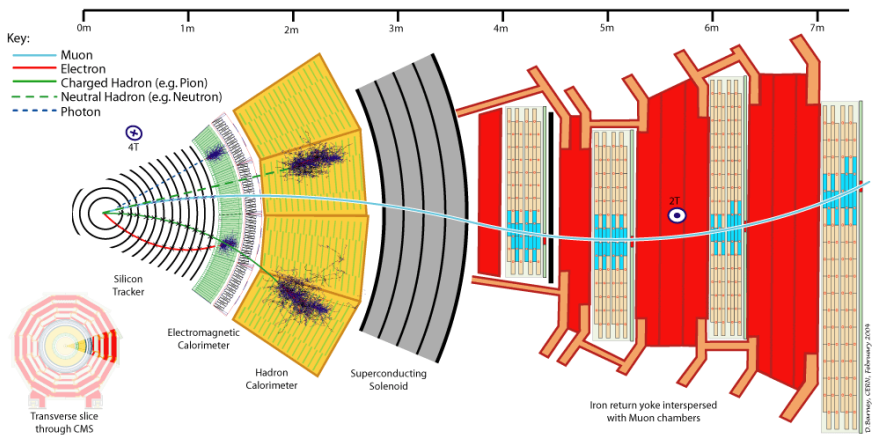

Figure 5.2: A transverse slice of the CMS detector, with the qualitative experimental signatures of the different particles.

ECAL The electromagnetic calorimeter is situated outside the tracker; is composed by scintillating $PbWO_4$ crystals, with an excellent resolution for energies ranging from 1 GeV to the TeV range; coverage is up to $|\eta| = 3.0$, even if precise data-taking is limited to $|\eta| \leq 2.6$. In the endcaps a *preshower* detector (lead and silicon strips) is used to improve the π^0 rejection through the $\gamma \to e^+e^-$ conversion and to help identifying the interaction vertex.

HCAL The intense magnetic field prohibits using iron, so the CMS hadronic calorimeter is made of layers of brass and scintillator plates. HCAL can detect hadrons up to $|\eta| = 3$, so an additional front calorimeter (HF) in quartz and scintillating fibers is installed to extend the reach to $|\eta| = 5$.

Magnet The magnetic solenoid is situated outside the hadronic calorimeter. It a superconducting solenoid, with inner radius of 3 m and a length of 13 m, able to produce a 4 T magnetic field when traversed by a 20 kA current.

Muon system The muon tracking system is made by drift tubes (barrel) and cathode strip chambers (endcaps) inside the return joke of the magnet. As muons are crucial for CMS physics, resistive plate chambers are used to provide an additional trigger system.

5.2 Tracker

5.2.1 Requirements

In the hostile environment of a high energy, high luminosity hadron collider, the requirements for the tracking system are stringent.

Occupancy At $\mathcal{L} = 10^{34}\,\mathrm{cm}^{-2}\mathrm{s}^{-1}$ the number of collisions in each bunch crossing is expected to be about 25, which results in $\sim 10^3$ tracks filling CMS

every 25 ns: reconstructing all those tracks require highly segmented detectors to avoid combinatorial issues given by multiple particles striking the same active element at the same time.

Momentum range To exploit the full reach of CMS, the tracker must provide a good momentum resolution up to TeV energies; nevertheless, an efficient reconstruction of low p_T tracks ($\leq 5\,\text{GeV}$) is crucial for isolation cuts.

Impact parameter Vertex reconstruction and good impact parameter resolution is necessary for b tagging, and to help isolation cut efficiency even in the presence of high pileup.

5.2.2 Pixel detector

The pixel detectors are used close to the beam pipe ($r \sim 4 - 10\,\text{cm}$), three layers in the barrel and two in the endcaps. Pixel detectors have a real 2d reconstruction of hits, which drastically reduce the combinatorial problem of track reconstruction; each pixel element is about $100 \times 150\,\mu\text{m}^2$ wide, which keeps the occupancy at the 10^{-4}.

The position resolution expected from pixel detectors from test beam studies and GEANT Monte Carlo is $10\,\mu\text{m}$ in the $r\phi$ coordinate and $15\,\mu\text{m}$ in the z coordinate. The signal over noise ratio for a minimum ionizing particle is ~ 70; efficiencies above 99%, except for the first layer ($\epsilon \simeq 96\%$), are expected.

Pixels play a crucial role in *track seeding*, and are also used for fast tracking at trigger level.

5.2.3 Inner tracker

In the range $r \sim 20 - 50\,\text{cm}, |z| \leq 65\,\text{cm}$ from the interaction point, charged particle flux drops below $6 \cdot 10^6\,\text{cm}^{-2}\text{s}^{-1}$ and silicon strip detectors can be used. Inner tracker strips are 10 cm long ad $80 - 120\,\mu\text{m}$ wide, which keeps occupancy at the $2 - 3\%$ level; the thickness us $320\,\mu\text{m}$. The inner tracker is composed of four barrel layers (TIB) and three endcap discs (TID); the first two barrel layers and the two inner rings of the discs are *stereo*, with two sets of modules tilted by 100 mrad so that the z coordinate can be measured by finding intersections between hit strips.

Charge deposits in each strip are read by analog devices (APV), one for each set of 128 strips, converted into optical signals by analog opto-hybrids (AOH) to be transmitted at the front end digitizers (FED) with 10 bit ADC; analog gain adjustment can be made on a per-AOH basis by selecting one of the four possible scales. APV can sample both in peak and in deconvolution mode, the latter providing a better time response at the price of a slightly higher sensitivity to noise.

In order to suppress noise, both common mode and pedestal corrections are applied: the first subtracts from the signal of each strip the average signal found on all the 256 strips, ignoring the ones above some threshold which are likely to be hit by a particle; the second correction is applied by subtracting the average of all common modes computed over a large sample of events (~ 1000). Typical values for the single strip noises are 5 ADC counts at operation temperature.

Modules are grouped in strings of three, or six for stereo layers, and " manifolds" of three to six strings, each one independent in both the control, power supply and cooling services so that any failure in one system won't harm the other parts of the tracker.

Each FED has nine readout units each able to handle the output of 96 pairs of APVs; FED are also in charge of applying zero suppression to reduce the overall data volume by an order of magnitude. Control signals, including trigger ones, are sent through a separate I2C control bus from the front-end controllers (FEC) to the DOHM (digital opto-hybrid module), one for each manifold, and then forwarded in a ring-like circuit to each module; backup DOHM assure a failover control channel.

Resolutions expected for single hits are $23 - 34\,\mu$m in the transverse $r\phi$ plane and, for stereo modules, $230\,\mu$m in the longitudinal z coordinate. For a minimum ionizing particle the signal to noise ratio is $\sim$11.

5.2.4 Outer tracker

In the outer tracker particle fluxes are low enough to allow for $20\,\text{cm} \times 180\,\mu$m strips while keeping occupancies below 1%; modules used in the outer tracker are also thicker ($500\,\mu$m). There are seven barrel layers (TOB) and 9 endcap discs (TEC); the first two TOB layers and TEC rings 2, 5 have stereo sensors with the same tilt angle as in the inner tracker.

Expected resolutions for single hit are $35 - 52\,\mu$m ($r\Phi$), $530\,\mu$m (z).

5.3 Electromagnetic Calorimeter

5.3.1 Requirements

ECAL, the electromagnetic calorimeter of CMS, has been designed aiming for three possible physics targets: a light Higgs boson decaying through $h \to \gamma\gamma$, a heavy Higgs boson decaying $H \to ZZ^{(*)}$ followed by $Z \to e^+e^-$, and possible heavy Z-like gauge bosons which appear in many beyond SM scenarios. In addition, good performance at low energies is required to identify electrons in jets, coming from the decays of heavy quarks.

The calorimeter must provide a very good measurement of energy from the low energy region, $\sim 1\,\text{GeV}$, up to the TeV scale; a general parametrization of the calorimetric energy resolution has three terms with different energy dependence:

$$\frac{\sigma(E)}{E} = a \oplus \frac{b}{\sqrt{E}} \oplus \frac{c}{E} \tag{5.1}$$

The constant a term, dominant at high energies, contains contributions from calibration (especially the inter-calibration between cells), longitudinal uniformity and containment.

The stochastic term b is due to Poissonian fluctuations in energy collection from photostatics and the amount of energy deposited in non sensitive material: because of this, it is much smaller in homogeneous calorimeters than in sampling ones ($\sim 2\%$ compared to $\sim 10\%$); this term is critical for the $h \to \gamma\gamma$ signal.

The noise term c comes mostly from electronics but receives contributions also from pileup, radioactivity, leakage currents and other similar effects; it is never important for single hard objects (electrons, photons), but it can influence jet reconstruction when many small energy deposits are summed.

Longitudinal shower shape $N(x)$ is approximatively given by $x^{\alpha}e^{-x/\mathrm{X}_0}$, so that a depth of many X_0 is required to fully contain high energy showers; full containment is necessary to avoid large uncertainties in the energy measurement due to fluctuations in the shower tail. Transverse profile of the showers scales as the Moliére radius (R_M), so that position resolution can be improved by using materials with short R_M, combined with a fine segmentation.

Transverse segmentation is also very important to discriminate single hard photons from isolated $\pi^0 \to \gamma\gamma$ and helps against pileup by reducing the integration area. For the same reason a fast readout is necessary to avoid integrating energy deposit from multiple bunch crossings. Calorimeter information must be available at the first trigger level, even if with reduced granularity, to allow for electron and photon trigger channels, which poses even more stringent requirements on the calorimeter readout timings.

Both sensitive material and the first steps of readout will be under a very heavy radiation flow, which require radiation hard materials to reduce the progressive decrease in resolution induced by radiation damage; particle fluxes increase rapidly with $|\eta|$, thus limiting the calorimeter coverage to $|\eta| \leq 3$, while precision measurements are further restricted to $|\eta| \leq 2.6$.

5.3.2 Calorimeter structure

Scintillating crystals

In order to keep the stochastic term in eq. (5.1) small an homogeneous design has been adopted. Lead tungstenate ($PbWO_4$) crystals have been chosen as sensitive material because of small X_0 (0.89 cm) and R_M (22 mm), and fast response (80% of the light emitted within 25 ns).

ECAL barrel crystals are quasi-projective[2], with a front face of $22 \times 22\,\mathrm{mm}^2$, matching the Moliere radius, and a length of 23 cm $\simeq 25.8\,\mathrm{X}_0$. Crystals are grouped in structures called submodules, 2×5 crystals wide in the $\eta \times \phi$ coordinates: electrons bent by the solenoidal magnetic fields emit bremsstrahlung photons in the forward direction, which will hit the calorimeter at the same η coordinate of the electron but at different ϕ; summing energy deposit in a whole submodule is a fast way of recovering such energy losses suitable for trigger level reconstruction.

In the barrel crystals are larger (28.62×28.62 mm) and shorter ($24.7\,\mathrm{X}_0$, as there is a preshower detector installed before them), grouped in $5x5$ structures called supercrystals.

Radiation damage R&D work has been done to quantify the effects of radiation damage to crystals, and to improve their hardness both by doping the crystal with niobium or lanthanium and by annealing the crystals in abìn oxygen-

[2] their axis forms a 3° angle with the vector from the nominal vertex, in order to increase hermeticity.

enriched atmosphere. The main effect of radiation is the formation of color centers in the crystal, which reduce light collection efficiency and introduce longitudinal non uniformities; the first effect is dominant, but can be corrected for by monitoring light attenuation factors through lasers and optical fibers. From test results it appears that the energy resolution degradation will be below 0.2% even after ten years of LHC operation and a 15% reduction of collected light.

Readout

Light yield of lead tungstenate is $30\gamma/MeV$ (1.3% of NaI, 7.2% of BGO), so devices with intrinsic amplification must be used.

APD In the barrel the light will be collected by avalanche photodiodes, solid state detectors where charge multiplication is provided by accelerating photoelectrons with a strong electric field so that additional electrons are produced by impact ionization on a $p-n$ junction. The gain selected for normal operation is 50, but larger values (up to 300) are possible without large noise increase.

VPT Radiation damage induced dark currents does not allow for APDs in the endcaps, so vacuum phototriodes (VTP) have been chosen. VPTs are basically tiny photomultipliers with a single gain stage and a short distance between electrodes to allow operation in the non uniform magnetic field up to $B \sim 4\,\mathrm{T}$. Smaller quantum efficiency (22% vs 75% of APDs) and a gain of only 10.2 are balanced by a larger light collection window.

Electronics In the electromagnetic calorimeter analog to digital conversion is done on the detector by *floating point ADC* after the signal is processed by a multi gain preamplifier: three possible gains ($\times 12$, $\times 6$, $\times 1$) are automatically selected to cover the full range 40 MeV to 1.7/3 TeV in the barrel/endcaps, with 10 bit ADC resolution. Fast cell summation for level 1 trigger usage and buffering while waiting for the trigger response are both done in the front end. The results are transmitted over optical links to data acquisition and trigger control. Selective readout, zero suppression and data compression using non linear scales are used to reduce the overall data size of one event from 2 MB to 100 kB.

Preshower detector

As the CMS calorimeter lacks longitudinal segmentation, π^0/γ rejection is hard, so a preshower detector is used in the encaps where hadron fluxes are greater. Two layers of lead, $2\,\mathrm{X}_0$ and $1\,\mathrm{X}_0$, followed by planes of silicon strips with 1.9 mm pitch are placed in front of the calorimeter to initiate showers: 95% of the photons will undergo pair production already in the first lead layer.

Photons from a 200 GeV π^0 will reach the ECAL front plane with an angular separation $\Delta\alpha \sim 0.07°$, which implies $\Delta x \sim 4\,\mathrm{mm}$; even if there is some broadening because of lateral shower development, it is possible to effectively resolve the two hits

While the preshower detector is also useful for improving the position resolution and the identification of minimum ionization particles, the uncertainty in the amount of energy lost within the absorber worsens the stochastic term in

the calorimeter by an additional 5%, which prohibits the use of a preshower in the barrel.

5.3.3 Performance and calibration

Energy resolution

Energy resolution expected from test beam data and GEANT4 Monte Carlo simulations is given by

$$\frac{\sigma(E)}{E} = 0.55\% \oplus \frac{2.7\%}{\sqrt{E\,[\mathrm{GeV}]}} \oplus \frac{155\,\mathrm{Mev}}{E} \qquad \text{(barrel)} \tag{5.2}$$

$$\frac{\sigma(E)}{E} = 0.55\% \oplus \frac{5.7\%}{\sqrt{E\,[\mathrm{GeV}]}} \oplus \frac{770\,\mathrm{Mev}}{E} \qquad \text{(endcaps)} \tag{5.3}$$

Major contributions in the stochastic term come from photostatics (2.3%), containment (1.3%) and the deposit in the preshower (5%, endcaps only); the constant is dominated by calibration (0.4%) and longitudinal non uniformities (0.3%). Figure 5.3.3 provides the energy dependence of the resolution in the barrel. It is important to note that diphoton mass resolution is influenced also from the knowledge of the interaction vertex: if it is precisely known the angular uncertainties are negligible, but if only the beam constraint is used the 5.3 cm uncertainty on the vertex contributes as 1.5 GeV to the mass width.

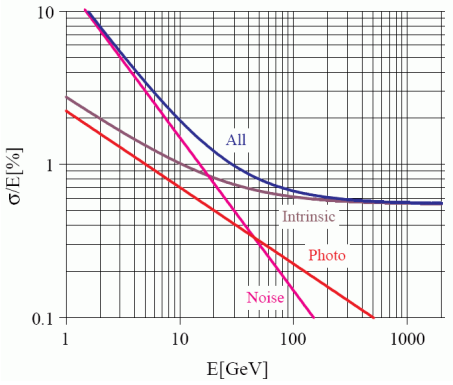

Figure 5.3: ECAL energy resolution (barrel), from [ECTDR]. Intrinsic uncertainty includes both containment and the constant term.

Calibration

Multiple methods will be used to calibrate ECAL. Test beam data will be used for startup calibration of the energy scale of each crystal, while later online methods will be used.

Radial symmetry A fast inter-calibration along the ϕ coordinate can be obtained by exploiting the symmetry of both physics and detector: by requiring the average energy deposit to be constant over ϕ, a $1-3\%$ accuracy in the calibration can be obtained in a few hours of data taking.

Single electron The simplest calibration method uses isolated electron tracks (i.e. from $W \to e\nu$), whose momenta can be measured by the tracker; this method relies on having a fully operational, aligned and calibrated tracker, so it can't be used at startup. A calibration precision of 0.6% appears to be attainable for $10\,\mathrm{fb}^{-1}$.

$Z \to e^+e^-$ decays The clean signal obtainable from Z decays can provide both absolute energy scale calibration and relative intercalibrations between crystals. Already with $2\,\mathrm{fb}^{-1}$ a 0.6% accuracy can be reached.

Di-photon decays Light meson such as π^0 and η decaying into photon pairs could provide an additional source of inter-calibration which is less sensitive to tracker material, if only unconverted photons are selected; by choosing events with a small opening angle, the combinatorial background is reduced. Statistical accuracy on the calibration constants is estimated to be below 0.5%, but systematics have not jet been fully investigated.

Light monitoring In addition to physics calibration, light collection efficiency must be monitored to correct for the ageing of the crystals due to radiation damage.

Reconstruction issues

In addition to calibration, reconstruction must take into account some other issues:

- The material budget before the calorimeter is between 0.5 and 1.2 radiation lengths, so that photons have a fairly large probability of undergoing pair production: specific algorithms have been designed to find associated electron pairs and reconstruct the parent photon.
- Electrons radiate bremsstrahlung because of the centripetal acceleration given by the magnetic field; these soft photons can be recovered during the electron reconstruction to avoid biases in energy resolution.
- Specific correction must be applied for the non sensitive areas: energy deposits from electrons hitting near crystal borders, or between crystal modules are only partially collected, but a calibration using lateral shower shape can be used to correct for this.

5.4 Hadronic calorimeters

Hadronic calorimetry is essential for measuring jets produced by quarks and gluons, and to spot and measure missing transverse energy produced by neutrinos (or more exotic particles).

Hadrons are often produced also at high $|\eta|$, so that the CMS hadronic calorimetry is build up with two devices, HCAL and HF, to provide excellent hermeticity for the whole range $|\eta| \leq 5$.

Additional subdetectors exist to provide even greater coverage, CASTOR (up to $|\eta| \simeq 6.5$) and the Zero Degree Calorimeter (ZDC), but they don't have

a direct impact on most physics analysis except for their use in luminosity monitoring, so they won't be described in this work; more information can be found in [PTDRv1], chapter 7.

5.4.1 Subdetectors and electronics

HCAL HCAL is the calorimeter designed to cover the central region, in the same pseudorapidity range of ECAL, $|\eta| < 3$; it is a sampling calorimeter with scintillator tiles and metal absorber plates.

The calorimeter is within the strong magnetic field so brass was chosen over iron for absorber material, except for the first and last two plates that are in stainless steel to increase the structural strength.

In the barrel, scintillator tiles $\Delta\eta \times \Delta\phi = 0.087^2$, 3.7 mm thick, are read out through a single wavelength shifter and clear optic fibers; light signals from projective towers built from the 17 layers are optically merged and read through pixelated hybrid photodiodes (HPD) mounted at the outer edge of the structure.

A single layer of scintillator tiles, HCAL Outer (HO) is mounted in the barrel region but outside the magnet solenoid, as a tail-catcher for deeper showers; tiles are projective with HCAL towers, but the readout channel is independent. The HO allows to reach a total depth of about 11 nuclear interaction lengths.

In the endcaps tiles with larger η size are used, and there is a larger fraction of absorber material over sensitive one; readout devices are the same as in the barrel.

HF The forward hadron calorimeter has to face a very harsh radiation environment, so that plastic scintillator is no longer suitable; a Cherenkov calorimeter in steel and quartz fibers is used instead, as it provides the necessary radiation hardness. In order to have total hermeticity, fibers are directly inserted in the steel absorber.

Due to its Cherenkov nature, the HF is much more sensitive to the electromagnetic component of the jet, such as photons from π^0 decays, and the hit position resolution is improved due to the more regular development of e.m. showers with respect to the hadronic ones.

Towers within HF are not projective, as fibers run parallel to the beam line, but some longitudinal segmentation is provided by using fibers of two different lengths.

Cherenkov light is carried by optical fibers outside the detector to a safe location shielded against radiation and magnetic field, where conventional phototubes (PMT) are used for readout.

Electronics Analog electric signals from HPT and PMT are converted to digital by fast ASIC devices called QIE (charge integrator and encoder) which dynamically choose different readout scales so that the ADC quantization error is always negligible with respect to the signal.

5.4.2 Performance and calibration

HCAL calibration Multiple calibration methods will be used both for overall energy scale calibration and cell-by-cell intercalibration.

Initially, collimated radiation sources and charge injectors will be used to validate the single components; global energy scale is obtained through test beam experiments with $\pi^{\pm}$, $e^{\pm}$ and $\mu^{\pm}$ beams for a limited set of modules.

At later steps, radiation sources, UV lasers and LED pulsers are used to monitor the response of all HCAL channels, and isolate tracks from physics events (especially hadronic tau decays) can be used both through E/p and p_T balance methods to further tune the calibration constants.

Specific calibration for the detector response to full jets are described later, in section 6.7.2.

Bare energy resolution A measurement of the bare energy resolution for single pion tracks at test beam is plotted in figures 5.4 and 5.5 for ECAL+HCAL and HF respectively. The resolution can be fitted as:

$$\frac{\sigma(E)}{E} = \frac{120\%}{\sqrt{E\,[\mathrm{GeV}]}} \oplus 6.9\% \qquad \text{(ECAL+HCAL)}$$

$$\frac{\sigma(E)}{E} = \frac{270\%}{\sqrt{E\,[\mathrm{GeV}]}} \oplus 13\% \qquad \text{(HF)}$$

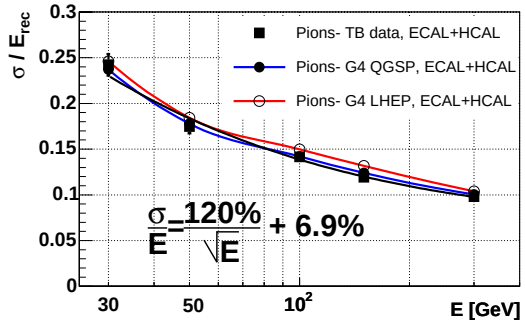

Figure 5.4: Energy resolution for ECAL + HCAL at test beam (single $\pi^{\pm}$), compared with Monte Carlo predictions

Response corrections The energy resolution of ECAL+HCAL can be improved by using energy-dependent corrections: from test beam data it is possible to determine a simple parametrization for the response functions of the two calorimeters and the average fraction of neutral particles. The improvement is substantial: the stochastic term is nearly halved (120% → 70%) with only negligible increase of the constant term (7% → 8%) on the whole range of test beam energies from 5 GeV to 300 GeV.

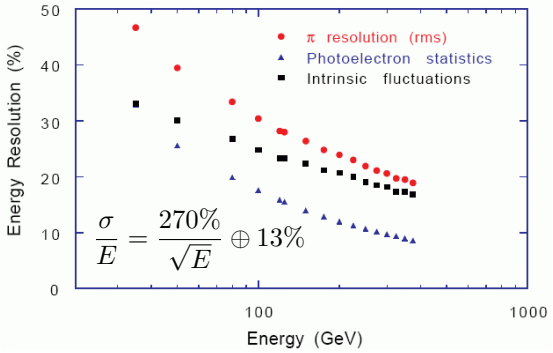

Figure 5.5: Energy resolution for HF test beam (single $\pi^{\pm}$); the photostatics is also computed separately, and the difference between photostatics and the total measured resolution is plotted as "intrinsic"

5.5 Muon System

5.5.1 The basics

Muons with energies below some TeV loose energy in matter only through ionization, so they can easily traverse through all the calorimeters with a very little energy loss while all the other particles except neutrinos give rise to shower processes and are absorbed. By placing a muon detector outside the calorimeters the tracks can be easily reconstructed as the hit multiplicity is much lower (the vast majority of tracks in the inner detector are charged hadrons). Muons are the cleanest signals available at LHC.

Muon Triggers In order to use muons at trigger level 1, a very fast p_T measurement must be performed. In addition, the whole trigger system is redundant: resistive plate chambers (RPC) and ionization chambers (drift tubes, cathodic strip chambers) are used in parallel to increase efficiency and to allow for operations even in the case of a complete failure of one system. Time resolution is important to assign the muon to the correct bunch crossing.

Momentum and charge resolution An accurate measurement of the muon momentum and the dimuon invariant mass are necessary: to improve the resolution, the measurement of the muon system can be combined with the inner tracker for a $\delta p_T/p_T \leq 1.5\%$ at 100 GeV, but the muon chamber information can be used also alone ($\delta p_T/p_T \sim 10\%$ at 100 GeV). Knowledge of the muon charge is also very important; the charge identification has to be correct 99% of the times for any value of p_T.

5.5.2 Structure

The muon system is composed by drift tubes in the barrel, for $|\eta| \leq 1.3$, cathodic strip chambers in the endcaps, $0.9 \leq |\eta| \leq 2.4$, and resistive plate chambers in both region, $|\eta| \leq 2.1$; the full layout is depicted in figure 5.6.

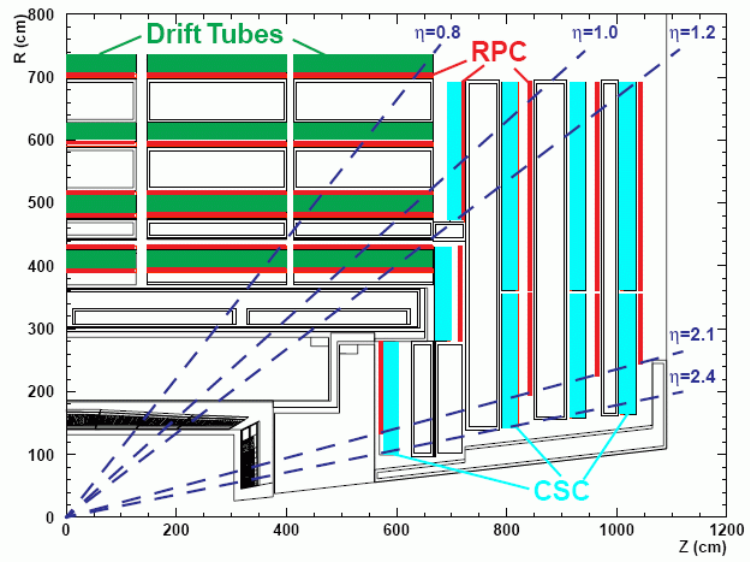

Figure 5.6: The muon system, showing drift tubes (TD), cathodic strip chambers (CSC) and resistive plate chambers (RPC)

The structure of each element of the muon system will be described here, while tracking reconstruction and trigger usage will be discussed later in section 6.6 and chapter 7 respectively.

5.5.3 Drift tubes

Drift tubes (DT) are used in the barrel, $|\eta| \leq 1.3$ to measure the muon p_T both for offline analysis and at trigger time, as the tubes are self triggering.

Drift tubes use the same principle as drift chambers: a charged particle ionizes the gas inside, and ions and electrons drift in the strong electric field between the anode and the cathode; the signal is collected when the electrons reach the anode wire. The distance between the particle track and the wire is measured through the drift time, as the electron rapidly reaches a constant drift speed of 55 μm/ns.

As the magnetic field is almost completely contained in the iron return joke, it gives no problem in operating the drift tubes.

Tubes Each tube is composed by an anode wire and two I shaped cathodes, shared with the neighbouring tubes, plus some field-shaping electrode strips used to improve the linearity of the distance/drift time relationship; a transverse section of a CMS drift tube is shown in fig. 5.7

Tubes have been chosen over conventional drift chambers to keep each wire protected from the noise produced in other cells[3], and as a safety measure against possible wire breaking.

[3] At TeV energies muons have also a non negligible chance of starting a e.m. shower

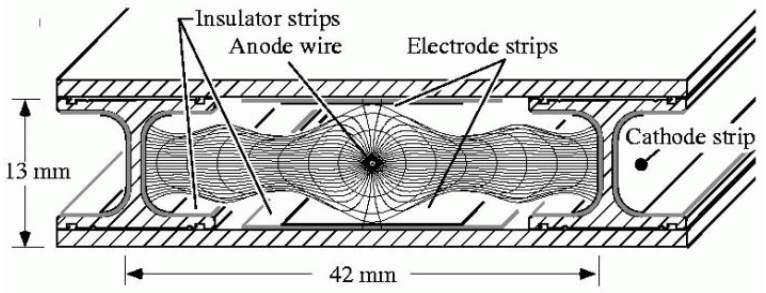

Figure 5.7: Transverse section of one muon drift tube

Layers Drift tubes are arranged in sets of four layers, with staggered tubes to prevent left/right ambiguities; in addition, a standalone time measurement can be done using the mean hit time on the four wires of a layer. Hit position within each layer are measured within 250 μm.

Stations A muon station is formed by three sets of four layers, two for the $r\phi$ coordinate and one for z, except for the outermost station that has no z plane. The resolution of a single station is 100 μm in $r\phi$ and 150 μm in z, and the time resolution is 5 ns; stations can also provide track direction measurement with ~ 1 mrad accuracy.

5.5.4 Cathode strip chambers

Drift tubes can't be used in the endcaps because of the strongly varying magnetic field and the much higher noise from hadron punch-through and radiation (mostly neutrons), so cathode strip chambers have been chosen because of their good speed and greater radiation hardness.

In these chambers, closely spaced (3.12 mm) anode wires are stretched between two cathodes, one segmented in strips ($3-16$ mm wide) perpendicular to the wires, spaced by 9.5 mm, and the other without segmentation. A particle traverses the cathodes and produces an ionization trail through the chamber; the electrons are accelerated to the wire, where an avalanche occurs, inducing a charge on the cathode (see 5.8. The coordinate orthogonal to the wire is measured by fitting the charge distribution on the cathode strips, while the longitudinal one is given by the wire that has been hit.
In CMS the strips have a fan shape, placed radially to measure the $r\phi$ coordinate, while the wires measure r. The strip width is $\Delta\phi = 10°$ for the first station and the external part of the other three stations, and 20° for the others; an angular sector of CSC is depicted in figure 5.9.

Each station is composed by six layers of cathode strips and wires: the hit point resolution in the $r\phi$ coordinate is 75 μm for the first station and 150 μm fot the others, and ≤ 200 μm in the r coordinate. CSC stations can also measure the the hit time, with a 6 ns accuracy.

Coverage is provided in the $0.9 \leq |\eta| \leq 2.4$ range, but at startup the chambers will be installed only up to $|\eta| \leq 2.1$.

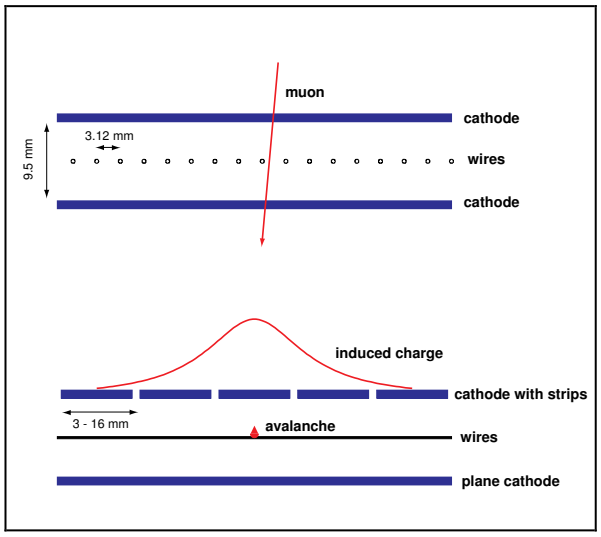

Figure 5.8: The basic principle of cathodic strip chambers

5.5.5 Resistive plate chambers

Resistive plate chambers (RPC) provide a complementary trigger system, very fast and with cheap readout; they can also help the track reconstruction in the CSC resolving ambiguities in pairing the 1D hits to 2D ones.
Begin an evolution of spark chambers, RPCs are capacitors with parallel electrodes, made of a material with high resistivity such as bakelite, coated with conductive paint (graphite). When a ionizing particle traverses the region between the plates a short discharge happens, rapidly stopped when the free charge on the conductive surface is exhausted. The readout is made using the induced charge in strips placed outside the capacitor, and isolated from the electrodes.

In CMS the chambers are actually double-gap, composed by a pair of high voltage electrodes on the two sides of a ground voltage one (see figure 5.10).

RPCs are operated in avalanche mode, where charge multiplication is not very high, to allow for high rates but requiring a strong amplification: in the preceding experiments (such as BaBar) chambers where operated in streamer mode, with higher gain but limited to $\sim 100\,\mathrm{Hz/cm^2}$ which is not suitable for LHC; lower currents should also reduce the ageing damage.

Six layers of drift chambers are used in the barrel: four on the two sizes of the DT stations 1 and 2, and two others on the inner sides of stations 3 and 4. In the endcaps RPCs are situated on one side of each of the four CSC stations (see figure 5.6)

RPC planes don't measure coordinates; in order to provide a hit position measurement a fine segmentation is necessary, and is allowed by the cheapness of the readout system. Track momentum is reconstructed with a non standard algorithm: fast electronic logic processors search for patterns in the RPC hits, which are keyed to different p_T regions; this coarse resolution is not good for offline track reconstruction, but is sufficient for the trigger, which benefits from

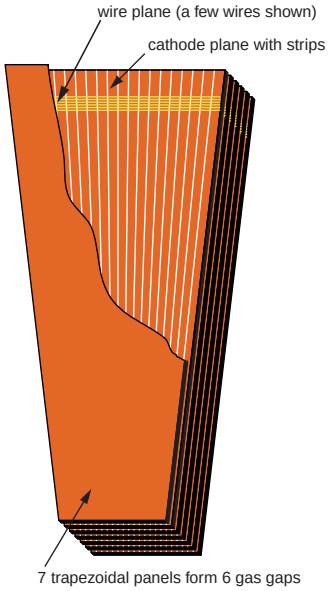

Figure 5.9: A sector of a cathodic strip chamber used in CMS; only some wires have been drawn in the figure.

the very fast speed of the response, comparable to that of scintillators (time resolution of 3 ns.

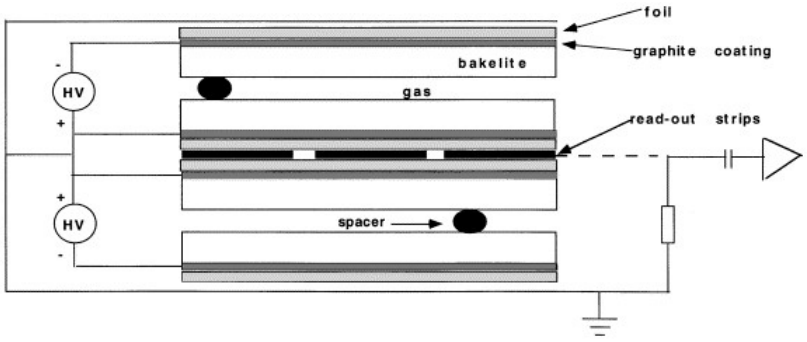

Figure 5.10: A double resistive plate chamber

Chapter 6

CMS Simulation and Reconstruction

6.1 CMS Software

Many software packages where developed specifically for the CMS experiment. A brief overview of the important elements used in the following chapters will be summarized here for convenience; a more complete description may be found in chapter 2 of [PTDRv1].

The CMS software has undergone many changes throughout its development, starting from Fortran and GEANT3 based software (CMKIN, CMSIM, ...), proceeding to a C++, object oriented, modular framework (OSCAR, ORCA, COBRA, FAMOS, ...) using GEANT4[G4] for detector simulation, and now heading to a unified C++ framework totally integrated with ROOT[ROOT], under the name of CMSSW, still under heavy development.

6.1.1 Simulation

Simulation of physical processes proceeds through two steps: first the physics of the event is simulated through a Monte Carlo program, and saved in some standardized format such as HepMC ntuples; next, the events are passed through the detector simulation, which is also in charge of simulating particle decays and interactions in the whole detector, except for a small region around the interaction vertex where the detector-independent simulation from the preceding step is used.

OSCAR The OSCAR[1] package, based on GEANT4, provides a full simulation of the CMS detector, including a complete description of the geometry, detailed modelling of the particles interactions within the different materials and simulation of the whole electronics readout.

The simulation has been extensively validated with test beam data.

[1] Object oriented Simulation for CMS Analysis and Reconstruction, [OSCAR].

As samples for most physical processes are used in many different analysis, the generation of fully simulates samples is done centrally by the CMS production team, which receives requests for event samples from the physics groups. The complete simulation of the CMS detector is a lengthy task, events with rich topologies like $t\bar{t}$ might require minutes to be simulated, so the production is distributed among the many computational nodes of the CMS collaboration, and access to data samples is provided through Grid.

FAMOS FAMOS[2] is a fast simulation software suitable for custom production of large amounts of events, as the time used for each event is reduced by about three orders of magnitude; it is needed for many tasks like the simulation of events with slightly different generator or detector parameters to evaluate systematic uncertainties, or when OSCAR samples for some physical process have not jet been produced. It is based both on simplified simulation of the real interaction of the particles in the detector material (with simplified geometry), and on parameterizations obtained from the full simulation.

Despite its speed, FAMOS gives a fairly accurate picture of the CMS detector response; a detailed comparison between the two simulations can be found in section 2.6 of [PTDRv1].

6.1.2 Reconstruction

ORCA All recent CMS analyses are based on the ORCA[3] reconstruction code, a modular system where multiple algorithms with their own parameter sets can be used for reconstructing all objects. ORCA implements the full detector reconstruction, starting from the (simulated) raw signals produced by the detector parts.

Different data tiers are produced, starting from the raw signals (Hits), proceeding through digitizion (Digi) and arriving to reconstructed physics objects in the Data Summary Tape (DST) tier; this effectively reduces the amount of data that must be read and processed in the analysis where only higher level information is used.

Data are fully distributed through CMS nodes of the LHC Grid and catalogued in a database so that they can be accessed in a way independent from the physical location of the data. The ExRootAnalysis software, a part of ORCA, is sometimes used to produce ROOT trees from ORCA data, which can be stored in conventional files and analyzed also outside the ORCA framework.

CMSSW Reconstruction within the new framework is based on Event Data (ED) streams starting from the sources, such as the real or simulated DAQ, lower levels objects produced in another stream, or ED stored on a file, passing through selection filters and then through analysis and output modules. Three data tiers are foreseen: Full Events (FEVT), which include also raw data; Reconstructed Data (RECO), where all reconstructed objects are included; Analysis Object Data (AOD), limited to medium and high level objects like tracks and jets but without the large volume of information of lower level data, such as no calorimeter cell energies or tracker hits.

[2] FAst MOntecarlo Simulation, [FAMOS]
[3] Object-oriented Reconstruction for CMS Analysis, [ORCA].

6.2 Event Reconstruction

Event reconstruction is done first at the subdetector level, staring from hits in the tracker an muon chambers, and energy deposits in calorimeter cells. ln the following steps these informations are combined to produce higher level objects (tracks, vertices, calorimeter clusters), up to the reconstructed physics objects (leptons, jets,...).

In this chapter hit and track reconstruction will be presented first (sec. 6.3), followed by vertex reconstruction (sec. 6.4); reconstruction of muons (sec. 6.6), electrons and photons (sec. 6.5), jets (sec. 6.7) and missing transverse energy (sec. 6.8) will follow. The description of the algorithms used to discriminate jets from b quarks (sec. 6.9) will conclude the the part on the reconstruction of physics objects[4].

The procedures for determining the luminosity will be presented last section of the chapter,6.10,

Details which are specific of the reconstruction at trigger level will be treated later in chapter 7.

6.3 Track reconstruction

The process of track reconstruction can be split into five steps: hit reconstruction, seeding, trajectory building, ambiguity resolution and final fit.

6.3.1 Hit reconstruction

Before any tracking can be done, particle hit points must be reconstructed from charge deposit within strips and pixels.

Pixel hits Hit reconstruction starts from pixels with a signal over noise ratio (S/N) above 6, and adding adjacent pixels if they have $S/N > 5$ until there are no more pixels to add; the cluster is then retained if $S/N > 10.1$.

Hit position is obtained by looking at the charges of the pixels on the edges of the reconstructed cluster. If the track angle is already known, such as when the track is partially reconstructed in some preceding step of the analysis, it is taken in account in determining the cluster center; otherwise the reconstruction is done as if the track was coming straight from the nominal interaction point.

Strip hits The merging procedure is similar to those of the pixel, except that clusters are started if $S/N > 3$, strips are added if $S/N > 2$ and clusters are retained if $S/N > 5$; for highly inclined tracks, one strip wide holes within the clusters are allowed.

Using the edge charges to determine the hit center is not possible for clusters with less than four strips, as the cross-talk between nearby strips is too high; in that case, the centroid of the charge distribution is used.

[4]The algorithms for tagging jets from hadronic τ decays will not be described, as they are not used in top quark physics

6.3.2 Track seeding

In order to start trajectory building, an initial estimate of the track parameters is required; the procedure of matching hits to produce track candidates is called seeding.

In order to estimate the track parameters two hits plus either a third hits or the beam constraint (only in the transverse region) or an already reconstructed vertex are needed.

Pixel pairs Pixels have low occupancies and precise 2d measurements, which makes them the ideal candidate for seeding. In the standard algorithm, pairs of hits within two pixel layers are used together with the beam axis constraint (that is, only in the transverse plane).

The algorithmic efficiency[5] is generally above 99.5%, while the global one is reduced by $1-2\%$ from geometrical and detector inefficiencies.

At low luminosity $\sim 4 \cdot 10^4$ pairs are found in a $H \rightarrow ee\mu\mu$ event, and the process takes up 30 ms CPU time (2.8 GHz Xeon). To simplify the trigger reconstruction (see 7.2), the algorithm can be limited to a smaller region: a $\Delta\eta \times \Delta\phi = 0.5 \times 0.5$ rectangle produces only 1/40 of the total hit pairs, and can be examined in just 6 ms of CP time.

Pixel triplets Triple pixel hits are sometimes used as they produce much less seed candidates, about two orders of magnitude less at low luminosity, and have a purity above 90%/80% at low/high luminosity; the efficiencies are obviously lower, 98% algorithmic, and 88%/82% total at low/high luminosy, and the computing time is almost the same.

Pixel triplets are used at trigger time instead of full tracks when a very fast reconstruction is needed, and might be used also in heavy ion collisions where the expected number of tracks is very high, so that a reduction of the total number of seeds by one or two orders of magnitude is well worth the 10% decrease in seeding efficiency for real tracks.

Pixel-less seeding In the very first runs at LHC startup the pixel detector will not be available, so that another seeding algorithm has been developed, using the first three TIB layers, the whole TID and the two inner rings of TEC layers 1-3. The efficiency is $1-2\%$ worse than for pixel seeding for $|\eta| < 0.5$, but equal to the pixel one up $|\eta| \sim 2$, where the pixel efficiency drops while the pixel-less one is good even up to $|\eta| \sim 2.3$.

Mixed seeding In cases where higher efficiencies at large values of $|\eta|$ is required, a combined seeding using pixel layers and the two innermost rings of the first three TEC layers can be applied, with an efficiency $> 96\%$ even up $|\eta| \sim 2.45$.

[5] Algorithmic efficiency is the efficiency computed only on events in which a full and correct input is passed to the algorithm, so it does not include detector effects like geometrical acceptance or noise

Pixel pairs + vertex seeding Especially at trigger time, it can happen that tracks and vertices are first reconstructed with the pixel information only and then using the full tracker information.; in that case, the already known primary vertices can be used when the seeding for full tracks is performed, instead of the much weaker beam axis constraint. The gain is a much larger suppression of ghost seeds, $\times 10$ at low luminosity and $\times 50$ at high luminosity; the efficiencies depend on the event type, and vary between 60% and $\simeq$ 100%.

A comparison plot of the efficiencies of pixel, pixel-less and mixed seeding is give in figure 6.1.

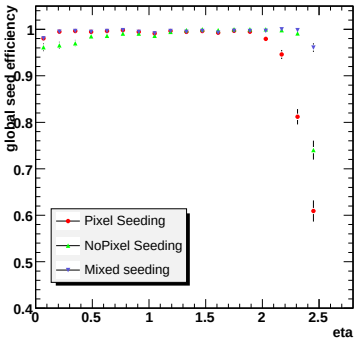

Figure 6.1: Global seeding efficiency for standard pixel seeding, pixel-less seeding and mixed seeding (pixel and TEC)

6.3.3 Trajectory building

Trajectory building is an iterative process based on the Kalman filter method[KF]: track candidates are extrapolated outward to the subsequent detector layers (*navigation*), and if matching hits are found, the track parameters are updated with the new information and the process is iterated on until a *stopping condition* is met or all the tracker layers have been traversed.

Navigation During the navigation step, the trajectory is evolved taking into account magnetic field, multiple scattering and energy loss in the material. When a suitable detector layer is found, hits are searched for within the spread given by the extrapolation uncertainties; for each suitable hit, a new track candidate is produced and fed into the next steps of the iteration. Inefficiencies due to failure in hit finding are reduced by allowing the track to "skip" one layer (a special "invalid hit" is added to the track instead of a real one); to avoid a combinatorial explosion of the number of tracks, only a maximum number of tracks (usually 5) is allowed to be propagated from one single seed, the other candidates are discarded (on a χ^2 basis) before proceeding to the next step.

Stopping conditions While the offline reconstruction of a real track will usually be completed only after all the tracker layers have been used, the propagation for bad tracks can be interrupted much before by requiring a maximum number of "invalid hits" in a track, either consecutive and global (usually 1), by

a cut on the fit χ^2 or if the reconstructed p_T falls below some threshold (usually 0.9 GeV).

When working at trigger level, usually the full tracker is not necessary, as the precision required can be met already with $5-6$ hits, and so an additional stopping condition is used to avoid spending time reconstructing all the $12-13$ hits.

6.3.4 Ambiguity resolution and final fit

Multiple track candidates may come from the same seed in the trajectory building step, but at the end this ambiguity must be cleared.

For each track pair, the shared hit fraction is defined as the ratio between the number of shared hits and the minimum among the number of hits in each tracks; if this fraction is above 0.5, one of the two tracks must be discarded: the track with more hits, or with smaller χ^2 if the number of hits is equals, is retained.

Ambiguity resolution is first applied to all tracks originating from the same seed, and then globally on all reconstructed tracks.

At the first steps of the track extrapolation, parameters are measured with large uncertainties, and this affects the quality of the final product of the iterations[6].

Because of this, at the end the track is refitted and smoothed: a Kalman filter is used again proceeding outward but removing the beam spot constraint and using the already fitted track parameters to improve the hit position measurements, and at every step a backward fit from the outermost layer inward to the current one is done and the two parameters are combined.

This procedure yields the best accuracy at both endpoints of the track, so that they can be used for extrapolations such toward as the position of closest approach to the beam axis, the interaction vertex or the inner side of the calorimeters.

6.3.5 Performance

Efficiencies Algorithmic and global efficiencies have been estimated with single particle samples (μ and π, $p_T = 1, 10, 100$ GeV) and QCD $b\bar{b}$ di-jet production ($\hat{p_T} = 120 - 170$ GeV) [7] including pileup expected at low luminosity.

For single muon both efficiencies are above 97.5% for all values of p_T in the $|\eta| < 2.1$ region. Pions have almost the same algorithmnic efficiency for $p_T \geq 10$ GeV, but for $p_T \sim 1$ GeV the value drops to 93%; global efficiencies are above 90% for for $|\eta| < 1$ and 85% for $|\eta| < 2$, if $p_T \geq 10$ GeV, and remain above $\sim 80\%$ even for 1 GeV pions.

In the QCD sample with pileup, algorithmic efficiencies are around 94%, while global efficiencies range between 90% and 80% as shown in figure 6.2(a). By changing the cut on the track χ^2/ndf global efficiency can be traded for

[6] This is particularly true for track inclination that strongly affects the hit measurement in the pixel layers

[7] $\hat{p_T}$ is the transverse momentum of the outgoing partons in center of mass frame of the partonic interaction.

higher fake track rejection, as show in plot 6.2(b); fake tracks are reconstructed mostly in the endcap region.

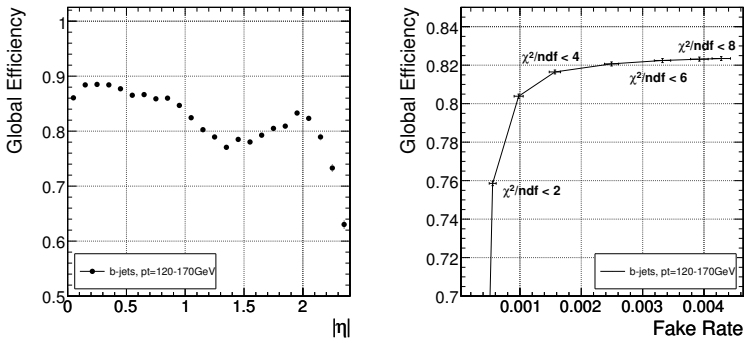

(a) Global tracking efficiency

(b) Efficiency vs fake rate for different χ^2/ndf cuts

Figure 6.2: Tracking efficiency for QCD $b\bar{b}$ di-jet production with $\hat{p_T} = 120 - 170\,\text{GeV}$ and low luminosity pileup

Resolution The resolution obtainable on the track parameters are shown in plots 6.3, 6.4. Momentum resolution is dominated by multiple scattering in the tracker material for low p_T, while for 100 GeV tracks its contribution is $20-30\%$; impact parameter measurement is mostly affected by the uncertainty of the hit in the first pixel layers for hard tracks, and by multiple scattering for soft ones.

The uncertainties when hit triplets in the pixel layers are used as tracks, i.e. at the first trigger steps, are plotted in 6.5

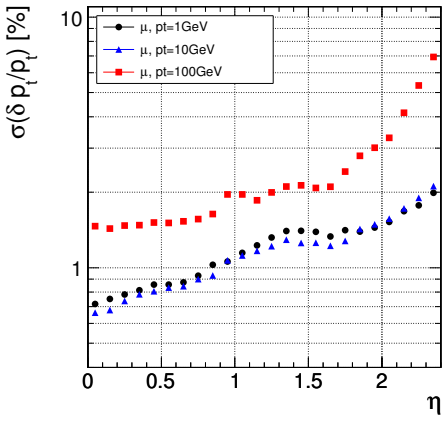

Figure 6.3: Tracking p_T resolution for single muons samples with $p_T = 1\,\text{GeV}$ (black dots), 10 GeV (blue triangles) and 100 GeV (red squares). Only tracker information is used here, see 6.6 for the full muon reconstruction.

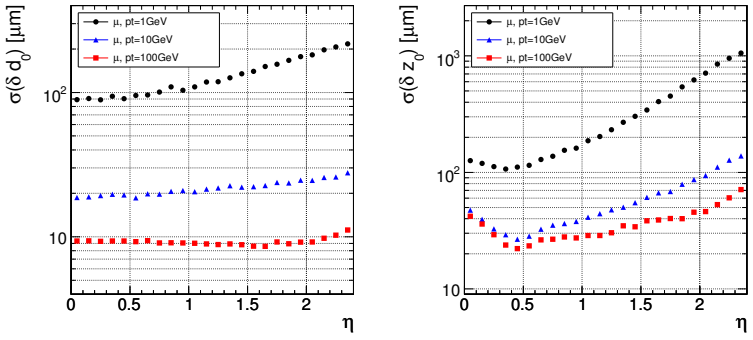

(a) Transverse IP (b) Longitudinal IP

Figure 6.4: Tracking impact parameter (IP) resolution for single muons samples with $p_T = 1\,\text{GeV}$ (black dots), $10\,\text{GeV}$ (blue triangles) and $100\,\text{GeV}$ (red squares). Only tracker information is used here, see section 6.6 for the full muon reconstruction.

6.4 Vertex reconstruction

The process of vertex reconstruction can be divided into two steps: first, tracks are grouped to form vertices (*vertex finding*), and then vertex parameters like position, $\sum p_T$ and χ^2 are estimated (*vertex fitting*). Nevertheless, often vertex finding algorithms use the vertex fitting ones to see if a set of tracks can be assigned to the same vertex.

6.4.1 Primary vertex finding

The method used for precisely reconstructing vertices employs all the tracks reconstructed in the event; there is also a faster method, used in HLT and described later, using only pixel triplets.

Preselection Tracks are preselected based on their distance of closest approach to the beam axis ($d_0/\delta d_0 < 3$) and p_T ($p_T > 1.5\,\text{GeV}$).

Track clustering Tracks are grouped using their z coordinate at the closest approach point: tracks with $\Delta z \leq 1\,\text{mm}$ are merged together

Simple fitting The tracks groups are fitted using the simplest vertex fitting algorithm, KVF (see below for details), and tracks not compatible with the vertex ($P < 5\%$) are removed.

Bad vertex rejection Vertices with poor fit quality ($P(\chi^2) < 1\%$) or not compatible with the beam line (again $P < 1\%$) are discarded.

Vertex are then sorted in decreasing order of the sum of the ${p_T}^2$ of the associated tracks.

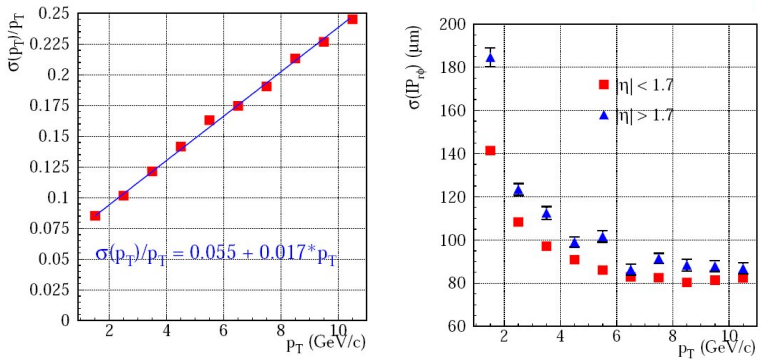

(a) Momentum (b) Transverse impact parameter

Figure 6.5: Resolution in p_T and transverse impact parameter when using hit triplets as tracks, for single muon samples

Secondary vertex finding Reconstructing secondary vertices, especially within jets, is important for any physics involving b quarks and is useful also for τ tagging; sometimes also the reconstruction of tertiary vertexes can be useful, for instance to reconstruct the $b \to c$ decay chain within jets.

The trimmed Kalman vertex finder (TKVF) uses the TKF fitter to first find primary vertices, and then tries to reconstruct secondary and tertiary vertexes using the tracks not compatible with the primary one. Additional requirements are applied: secondary vertices must be between $100\,\mu$m and $2cm$ far from the primary vertex in the transverse plane, and this distance must be statistically significant ($> 3\sigma$); the total invariant mass of the tracks must also be below 6.5 GeV (no secondary vertices are expected from SM particles heavier than b-flavoured hadrons)

6.4.2 Vertex fitting

Three different algorithms have been studied within CMS reconstruction. Their performance has been tested on a wide range of fully simulated samples, including the pileup expected for low luminosity runs: $B_s \to J/\Psi\phi$, $h \to \gamma\gamma$, Drell Yann $\mu^+\mu^-$, $t\bar{t}$, $t\bar{t}H$ ($H \to b\bar{b}$), and qcd di-jet production (both light quark and $b\bar{b}$ jets).

KVF The simplest fitter is known as Kalman Vertex Fitter, and uses a least-squares fit of all the tracks in the vertex, equally weighted. It is fast, but assumes that all measurements have Gaussian uncertainties and is then very sensitive to outliers (very ill-measured tracks, fake tracks or tracks not really coming from the vertex) so that the p-value of the fits is often very low.

TKF The Trimmed Kalman Fitter is a robust iterative version of KVF: at each step, if there are tracks not compatible with the fitted vertex, the least compatible one is discarded and the fit is iterated again. On average, $7-10\%$

of the tracks are discarded this way, and the fit fails to converge on about 0.1% of the vertices.

The TKF algorithm is slower than KVF ($\times 2 - \times 6$), but it improves the resolution of the vertex position, especially for difficult event types like $t\bar{t}H$: the σ is some $10 - 30\%$ lower, and the width of the 95% coverage region[8] is reduced by a factor $1.5 - 4$.

AVF Another robust algorithm has been developed within CMS, the Adaptive Vertex Fitter, where tracks are downweighted by their distance from the vertex scaled by the uncertainty on such distance; the procedure of reweighting and fitting is iterated over until it converges.

The average weight of the tracks is $0.90 - 0.93$, which means that almost the same number of tracks are "discarded" with AVF and TKF, but the fit fails to converge only in 0.02% of the vertices.

The algorithm is slower than TKF (up to $\times 1.5$) for small simple events, and faster for events with more that 30 tracks like $t\bar{t}H$ or $t\bar{t}$; the resolution on the vertex position is almost the same as for TKF.

A summary of the vertex position resolutions obtainable with the various algorithms is provided in table 6.1.

Table 6.1: Vertex position resolution expected from the different algorithms at low luminosity. Both the σ of a Gaussian fit and the half-width of the 95% confidence interval are given.

		$\Delta x[\,\mu\text{m}]$		$\Delta z[\,\mu\text{m}]$	
Sample	**Algo.**	σ	95%	σ	95%
	KVF	44.1	176	54.3	224
$\mathbf{B_s \to J/\Psi\phi}$ (pri vtx)	AVF	38.4	94.9	48.7	140
	TKF	39.4	98.7	49.5	144
	KVF	55.8	164	73.8	471
$\mathbf{B_s \to J/\Psi\phi}$ (sec vtx)	AVF	53.6	155	73	440
	TKF	54	174	75	502
	KVF	28.1	124	34	152
$\mathbf{h \to \gamma\gamma}$	AVF	22.1	73.7	29.9	106
	TKF	23	74.9	29.6	111
	KVF	15.5	77.1	26.5	119
Drell-Yan $\mu^+\mu^-$	AVF	12.7	39.2	22.5	60.4
	TKF	13.6	39.6	23	62.5
	KVF	14	118	17.9	112
$\mathbf{t\bar{t}H}$	AVF	9.55	21.1	13	30.3
	TKF	9.87	21.7	13.3	31.7

Kinematic Vertex Fitting In order to improve the resolution in the $B_s \to J/\Psi\phi$ channel, kinematic fitting of the vertex has been studied (see [1]). Energy-momentum conservation and mass constraints can be applied to constrain the

[8] As the vertex position resolution has non Gaussian tails, this region can be wider than the $[-2\sigma, +2\sigma]$ interval.

tracks in the vertices using Lagrangian multipliers in the KVF least-squares fit[9]. The resolution on the B_s mass is reduced by a factor two, both for σ and the 95% confidence interval.

6.4.3 Pixel vertices

Pixel vertex finding and fitting is necessary for b tagging at HLT level, and can be used to improve track reconstruction by using the fitted vertices instead of the beam spot constraint. Two algorithms for vertex finding have been tested, with the same samples used for standard vertex fitting. In both cases, tracks reconstructed using only pixel triplets and the vertex position is reconstructed only on the z axis. Pixel vertex reconstruction is very useful to identify tracks coming from pileup, which allows track-based isolation algorithms to remain efficient even under heavy pileup.

Histogramming Tracks are clustered by iteratively merging tracklets whose distance of closest approach to the beam line is below a fixed threshold.

Divisive This algorithm searches for large Δz regions with no tracks to subdivide the tracks into groups; within each group, an average vertex position is calculated and tracks compatible with that position are assigned to the vertex, and the procedure is repeated again looking for new vertices among the remaining tracks until all tracks are associated to a compatible vertex.

The divisive algorithm has shown to perform better, with a resolution of $\sim 50\,\mu$m in most of the event types considered. In both cases the efficiencies are smaller than for the track vertex finding, and for event types with low charged multiplicity such as $h \to \gamma\gamma$ values of $\sim$80% are expected.

As in the track vertex finding the vertices are sorted using the sum of the ${p_T}^2$ of the tracks, but with an upper limit of 10 GeV on the p_T as the resolution on the p_T of hard tracks using only pixels is bad due to the small lever arm.

6.5 Electron and photon reconstruction

6.5.1 Clustering

Energy deposits within the ECAL are grouped first to form clusters (associated to a single shower) and then SuperClusters, the calorimetric object associated to an electron or photon and all its possible radiations.

Hybrid algorithm It has been shown at test beams and with simulations that for single showers a reconstruction using a crystal array of fixed size[10] gives better energy resolution than a dynamic clustering, but bremsstrahlung and radiation in the magnetic field often produce additional energy deposits in the ϕ direction. Because of this, medium to high energy objects ($p_T > 5$ GeV) are

[9] As constraints are required to be held exactly, mass constraints cannot be used unless the natural width of the particle is below the experimental resolution, which is true $J/\psi \to \mu^+\mu^-$ but not for $\phi \to K^+K^-$

[10] Approximatively 94% of the energy of a single electron or photon is contained within 3×3 crystals, and 97% within 5×5.

usually reconstructed with the Hybrid algorithm, which first uses a fixed cluster side in the η, and dynamically determines the shower spread in ϕ.

Island algorithm For low energy deposits, very important for calorimetric isolation cuts, a different algorithm is used: starting from a seed crystal, adjacent ones are scanned first in ϕ and then in η adding them to the shower until a crystal not read out or a rise in energy is found. Seeding is done looking for high energy cells and starting with an array narrow in η and wide in ϕ.

Position measurement As crystals, in order to increase hermeticity, are not exactly projective, the correct position of the energy deposit within a crystal depends on the depth, and is usually parametrized as $a \cdot (b + \log(E))$ with different a, b for electrons and photons.

Using the energy weighted position of the cells does not provide the best position estimate for single clusters, as it is too biased towards the shower core. A better result on the $\vec{x}$ position can be obtained with a $\log(E)$ weighting.

$$\vec{x} = \frac{\sum_i w_i \vec{x}_i}{\sum_i w_i} \qquad w_i = w_0 + \log \frac{E_i}{\sum_j E_j}$$

For the estimation of supercluster position, instead, the energy weighted position of the clusters is appropriate.

Saturated channels A very high energy deposit in a single crystal ($E = 1.7\,\text{TeV}$ in the barrel, $E = 3\,\text{TeV}$ in the endcaps) can saturate the crystal ADC. In this case an algorithm has been designed to recover the correct value of the energy by using the deposits in a 5×5 crystal array. We won't discuss the algorithm here, as the energies involved in top quark physics are much below the ADC saturation values; more details can be found in section 10.1.4 of [PTDRv1]

6.5.2 Photon reconstruction

Isolation Many possible variables have been considered for photon isolation, using tracker and calorimeter information, and different ways of combining them (either summing energies or using multivariate methods). Rejection factors up to 50 for 90% signal efficiency appear to be attainable, and for signals with very high background (i.e. $h \to \gamma\gamma$) a background rejection of a factor 200 is possible with 50% signal efficiency.

Photon conversion The tracker material budget is very high, even exceeding $1\,\text{X}_0$ for high $|\eta|$, so that a non negligible fraction of the photons undergo pair production. By correctly pairing electron tracks, converted photons can be reconstructed with a total efficiency of 75% for a reference $h \to \gamma\gamma$ sample; if also single tracks are used to reconstruct photons then the efficiency is above 91% while keeping a 6%(9%) p_T resolution in the barrel (endcaps).

Photon conversion is also useful for π^0/γ rejection, and allows to reconstruct the photon vertex with a 1.9 cm accuracy.

6.5.3 Electron reconstruction

Tracking Electrons undergo much larger energy losses in the tracker material than other particles, which makes track reconstruction more challenging.

A specific non linear generalization of the Kalman filter has been designed, including Bethe-Heitler modelling of energy losses; while the energy resolution does not improve significantly, the position resolution (especially at both track ends) is greatly improved. This is due to the fact that the standard KF usually stops finding hits when the energy losses have decreased the electron p_T significantly.

Seeding is usually done using two pixel layers and the SuperCluster position, which allows also for fast and robust pixel tracking at trigger level 2.5 (see sections 7.2, 6.3).

Efficiencies are above 90% in the whole detector ($\simeq$ 96% in the barrel), except for very soft electrons ($p_T \lesssim 10\,\mathrm{GeV}$).

Cluster-track matching After an electron track has been reconstructed, angular matching and E_{cal}/p_{trk} cuts are applied, and a better estimate of the momentum is obtained by combining the two measurements.

Isolation Track isolation is usually performed by looking first at energy deposits in HCAL cells behind the SuperCluster, and then searching for tracks starting from the electron vertex and contained in a cone around the electron momentum.

Identification Isolation is not enough to provide good background rejection, so a larger number of observables is used to better identify electrons, using also lateral shower shape variables, and tracker variables at both ends of the track. Even keeping the efficiency above 90%, a rejection factor of $1.7 \cdot 10^3$ for jet background can be achieved.

6.6 Muon reconstruction

Global reconstruction Muon reconstruction can be performed either using only the muon chambers (*standalone*) or using also the tracker information (*global*); in the latter case, candidate tracks from the muon chambers are propagated back through the magnet and the calorimeters, taking into account magnetic field and energy losses, and a suitable track is searched in the outermost tracker layers, and an overall fit of the trajectory is attempted.

Muons with TeV-scale energies have a non negligible probability of loosing a significant amount of energy through radiative processes. In order to determine possible hard energy losses in the material between the outermost tracker layer and the first muon chamber, fits of the track using only tracker hits or including the first muon chamber are performed, and the χ^2 probabilities are compared.

The efficiency for global reconstruction is somewhat lower (fig. 6.6), as a larger number of matching hits is required, but the p_T resolution is greatly improved (fig. 6.7), and the charge misidentification chance is also reduced by almost two orders of magnitude.

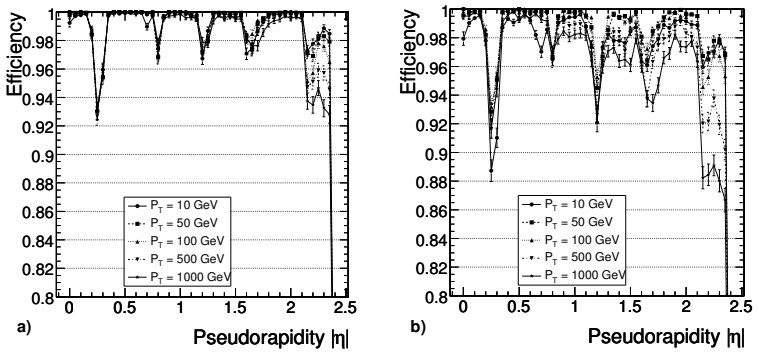

(a) Standalone (b) Global

Figure 6.6: Muon reconstruction efficiency as a function of $|\eta|$ for different p_T values, either using only the muon system plus vertex constraint or including also the tracker information

Effects of misalignment In order to provide an even more realistic estimate of the muon reconstruction performance in the first years of CMS, algorithms were tested in two different misalignment scenarios (first data taking and long term alignment). Even if at startup the performance is slightly degraded, the alignment procedures based on real data will allow to reach a performance almost exactly matching the one of a perfectly aligned detector.

Muon identification Identification of muons takes into account also calorimeter information, using a likelihood function to combine variables describing the energy losses in ECAL, HCAL and the HO scintillator layers.

A different approach to identification can be used for low p_T muons, as the standalone efficiency is lower: if a track is reconstructed in the inner tracker and some compatible hits are found in the muon chambers, this is usually enough to tag the object as a muon.

Muon isolation Muon isolation can be evaluated using the weighted sum of ECAL and HCAL deposits, pixel tracks or full tracker tracks; in any case, the algorithm is applied to objects within an axis given by the muon momentum at the vertex, except those within a smaller veto cone around the muon track or the extrapolated muon impact point at the calorimeters.

The veto radius varies with the position resolution of the source: 0.1 at HCAL, 0.05 at ECAL and 0.015 for any type of tracks; the isolation cone radius and the isolation E_T cut can be tuned for each specific analysis, typically $R \sim$ 0.2-0.3, $E_T \sim$ 1-5 GeV.

6.7 Jet reconstruction

A high p_T parton (quark or gluon) emerging from the hard scattering produces a jet of collimated particles, mostly light mesons like π's and K's, that end up in a cone in the $\delta R^2 = \delta\eta^2 + \delta\phi^2$ metric the size of which is approximatively independent from the parton p_T and flight direction. Because of this, there is

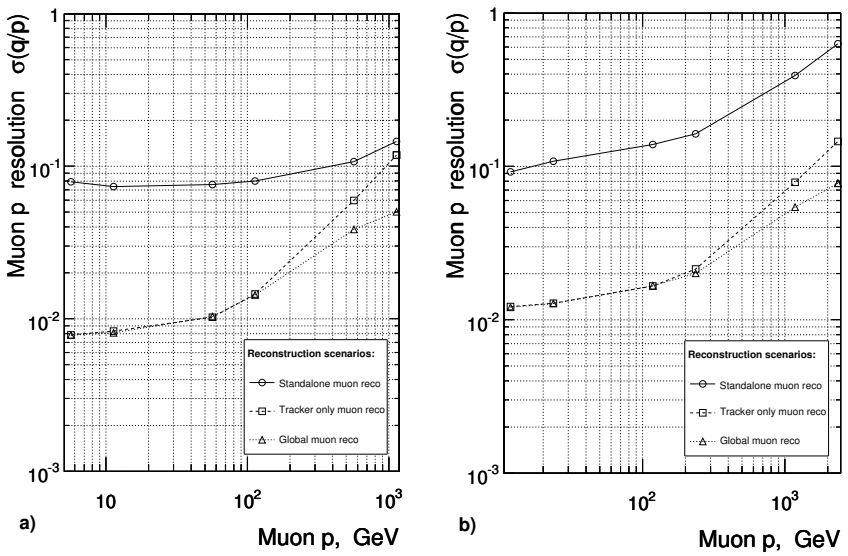

(a) Barrel (b) Endcaps

Figure 6.7: Muon p_T resolution as a function of p_T in the barrel ($\eta = 0.5$) and in the endcaps ($\eta = 1.5$), for standalone (circles), global (triangles) and tracker only (squares) reconstruction.

rarely any interest in the details of the particles after hadronization and the only concern is to find a way to cluster them in one object the energy and flight direction of which well approximates the one of the original parton.

6.7.1 Jet clustering algorithms

Different clustering algorithms can be applied to reconstruct jets. Algorithms can be used to cluster almost any type of objects: the objects used more frequently are calorimeter cells or towers, but for Monte Carlo studies sometimes also the particles after hadronization are considered; in the following explanation we assume that towers are used, but adapting the procedure to other objects is straightforward.

Iterative cone jets The iterative cone (IC) is a simple but fairly accurate algorithm suitable for both online and offline analysis. It has been used in all the single top CMS analysis presented in this thesis.

The algorithm is seeded using calorimeter towers above some E and E_T thresholds[11]. Starting from the tower with highest E_T, an iterative algorithm is used to reconstruct the jet, and the towers associated to it are removed from the list; the procedure is iterated until no candidate towers are left.

At each iteration step for the single jet, the cells within a cone of fixed $\Delta R = \sqrt{\Delta\eta^2 + \Delta\phi^2}$ are used to compute new jet direction and E_T. The algorithm is

[11] Usually $E_T > 0.5\,\text{GeV}$, $E > 0.8\,\text{GeV}$; the rather low E threshold is needed to suppress external noise that is almost uniform in η and thus can have a high E_T in the central region

repeated until it converges, i.e. until one step changes E_T by less than 1% and the direction by $\delta R < 0.01$, or the maximum number of allowed iterations is reached (usually 100).

Midpoint cone jets The midpoint cone algorithm is an improvement of the iterative cone algorithm designed to better handle overlapping jets.

At first, the IC algorithm described above is applied, except that towers associated with one jet are not removed from the list so that jet candidates can share the same tower. In a second step, whenever two jets are closer than the cone radius used, a *midpoint* vector is calculated using the sum of the two momenta, and a new jet candidate is seeded around that point.

A splitting and merging procedure is applied to this set of jet candidates, starting from the one with highest E_T: if this candidate does not share objects with any other jet candidate, it is removed from the list and stored as final jet; otherwise, the amount of energy shared with the neighbouring jet candidate with highest E_T is looked for; if it is above some threshold (usually 50%) the two jets are merged, otherwise the shared towers are split assigning each one to the closest jet in the (η, ϕ) space. The procedure is repeated again, always starting from the highest E_T candidate, until all candidates are stored as final jets.

k_T jets Inclusive k_T algorithm successively merges clusters, such as calorimeter towers or cells, until all the objects are stable.

At the beginning the list of objects is composed by energies in each calorimeter tower, which are given a light-like 4-momentum using the measured E_T and the known (η, ϕ) position.

For each of the N input objects i the d_i quantity is computed:

$$d_i = E_{T,i}^2 \cdot R^2$$

(R is a dimensionless parameter of the algorithm, 1 or 4 are values typically used in CMS)

In addition the quantity $d_{i,j}$ is computed for all the N^2 pairs of objects i, j.

$$d_{i,j} = \min(E_{T,i}^2, E_{T,j}^2) \cdot \Delta R^2(i,j)$$

with $\Delta R^2(i,j)$ the separation between the two objects in the (η, ϕ) space. The algorithm searches for the minimum values among the $d_{i,j}$ and the d_i. If the smallest of the d_i is smaller than any $d_{j,k}$ then the i-th object is considered stable, is removed from the working list and stored as final jet; otherwise, if the smallest $d_{i,j}$ is smaller than any d_k, the two objects i, j are merged in a single object with 4-momentum.

The procedure is iterated until all objects have been stored as "final" jets.

Sliding window (trigger L1) At trigger level 1 all these iterative algorithms cannot be applied, as a fast and fixed reconstruction time is needed.

In this case, towers are grouped in 4×4 regions, and a 3×3 mask is slided over the $\eta \times \phi$ map of the regions; a jet is reconstructed if the central region has higher E_T than all the 8 surrounding ones (and no electrons or photons have been found inside it)

6.7.2 Jet resolution and calibration

Two kind of effects contribute to a possible difference between the four-momenta of the parton and the reconstructed jet:

- Theoretical effects like final state radiation or the emission of particles at a large angle during the hadronization phase produce a difference between the parton momenta and the total momenta of the clustered particles (*particle jet*)
- Experimental issues like the non linearity of the calorimeter response or the noise from pileup and electronics produce a difference between the particle jet and the jet reconstructed from the calorimeter deposits.

These differences influence both the momentum resolution for the reconstructed jets and the knowledge of the overall jet energy scale. Improving the first requires to choose good reconstruction algorithms, while to improve the second a suitable calibration method must be found.

Calorimeter response

Hadronization is a stochastic process, and the amount and type of final state particles can change much between events with the same partonic final state.

A *non linearity* in the calorimeter response to hadrons makes the reconstructed energy dependent, for example, on the number of produced particles and not just on their total momentum, broadening the energy resolution (a plot of the calorimeter response to pions is shown in figure 6.10).

Likewise, a systematic difference between the calorimeter response to charged hadrons and to photons or electrons will introduce a dependence on the charge of the produced pions (π^0 decay immediately to photon pairs); this is usually expressed as the e/π ratio between measured energies of electrons and charged pions with the same momentum.[12]

Moreover, charged hadrons are bent by the magnetic field so that not all of them will hit the calorimeters within the cone in which they where generated, and this effect introduces a dependence both on the pion charges and momenta (softer pions are easily lost).

In addition, other uncertainties in the response come from the amount of energy of the hadronic cascade that is lost in nuclear reactions (splitting of nuclei, production of radioactive isotopes or slow neutrons) which are usually undetectable.

Jet calibration

The recoil method The main method that will be used for jet calibration at CMS is the *recoil method*, already tested in other experiments like $D\emptyset$. It is based on selecting events in which a parton recoils against another object whose momentum is measured with much greater accuracy (usually a photon or a Z boson), and imposing momentum conservation in the transverse plane; this provides directly a calibration between the transverse energy of the reconstructed jet and that of the recoiling parton.

[12] Photons are much more abundant than electrons in jets, but e/π is better measured in test beam experiments or using tracker information, and due to the (usually) much better electromagnetic energy resolution $e/\gamma \simeq 1$ so that $e/\pi \simeq \pi^0/\pi^{\pm}$

di-jet balance For large pseudorapidity (i.e. $|\eta| \gtrsim 2.5$) precision measurements of Z and photons are no longer available, so the calibration is done using the abundant di-jet events where one jet is in the barrel, for which calibration constants are already available, and one is at large $|\eta|$. This allows to extend the calibration to the whole η range of the hadron calorimeters (HCAL+HF).

Radiation and p_T unbalance One issue in this correction comes from radiative effects and underlying event: because of initial state radiation and net momentum carried away from the underlying event particles, the total $\vec{p}_T$ of the pair is not exactly zero; also, as the two produced objects radiate, they can lose some fraction of their momentum[13], further breaking the $\vec{p}_T$ balance. This must be correctly taken into account, as a naïve calibration using $\sum \vec{p}_T = 0$ would yield wrong values[14].

Uncertainties in the calibration Radiative effects are not the only systematic uncertainties: first, the values of the calibration constants obtained depend on the cuts used to select the events, which means that they are not universal (i.e. the calibration constants from $\gamma + jet$ events will not be optimal for all physical processes); next, the correct calibration constants for jets initiated by light quarks won't be fully appropriate for gluon or heavy flavour jets. Finally, the contributions from background events and the statistical uncertainty will contribute to the total calibration uncertainty

Other calibration methods

Other calibration methods exist, either more limited in scope, or expected to yield larger systematical uncertainties.

W mass calibration Thanks to the large $t\bar{t}$ production cross section and their clear signature, it will be possible to obtain a large sample of $t\bar{t} \rightarrow W^+bW^-\bar{b} \rightarrow \ell^+\nu b\bar{b}qq'$ for which the W mass constraint $m(qq') = m_W$ can be used to extract a jet energy scale calibration. This method can improve the knowledge on the energy scale, but it is limited to a small range of energies around $m(W)$.

Monte Carlo jet calibration A simple calibration procedure consists in determining the calibration efficiencies from simulated events ; this procedure is fast (as long as fully simulated events are available), and can be applied immediately at LHC startup, but is model dependent. It is also useful when studying the jet energy resolution, as by calibrating exactly calibrating the scale on that specific simulated sample one can obtain the net resolution without including calibration uncertainties.

Expected performance

Jet resolution The expected resolutions in transverse energy and direction for CMS is plotted in figures 6.8, 6.9. As Monte Carlo calibration method has

[13] Collinear radiation from a parton is not lost, as it ends up in the jet cone, but radiation at larger angles can be lost

[14] There is some subtlety in the procedure, as not only $\sum \vec{p}_T \neq 0$, but also the average parton $|p_T|$ for a fixed value of the other object p_T is not equal to the object p_T.

been used, this does not include jet energy scale uncertainty.

Jet energy scale At startup a 15% uncertainty is assumed, from test beam results and Monte Carlo calibration; already with $1\,\mathrm{fb}^{-1}$ integrated luminosity the energy scale is should be known within 5% for jets with $E_T > 50\,\mathrm{GeV}$ and degrading linearly to a 10% uncertainty at 25 GeV, and at $10\,\mathrm{fb}^{-1}$ the expected uncertainty is half of the one at $1\,\mathrm{fb}^{-1}$.

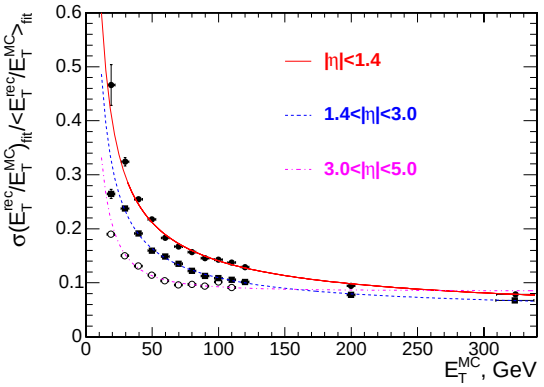

Figure 6.8: Transverse energy resolution expected for IC($R = 0.5$) jets, using Monte Carlo calibration

Improving the response using tracks A study has been made on the possible uses of tracker information to improve the jet energy resolution by correcting, at least partially, for the non linear response of the calorimeter and the loss of particles from the cone due to the magnetic field[CMS NOTE 2004/015].

The procedure assumes the response of the calorimeters to charged pions as a function of their momenta to be known either from test beam studies or in events with one isolated track (the expected responses from Monte Carlo studies are shown in figure 6.10).

The energy of the jets is corrected by adding the expected difference between the calorimeter response to tracks found within the jet cone and their real energy, using the p_T measured by the tracker. The energy of tracks that are within the jet cone at the production vertex but not at the calorimeter surface (out of cone tracks) is also added to the reconstructed jet energy, correcting for the effects of the magnetic field.

The results of these corrections is a $10 - 25\%$ relative improvement of the jet energy resolution; in the barrel the correct jet energy scale is recovered completely, and even in the endcaps (for $1.4 < |\eta| < 2$) the improvement is sizable, $E_{rec}/E_{gen} - 1$ is halved.

6.8 Missing transverse energy

Missing transverse energy in SM physics is a signature of neutrinos, and if there is a single neutrino in the event its transverse momentum can be determined as energy-momentum conservation requires $\vec{p}_T(\nu) = \vec{E}_T^{miss}$; if there are more

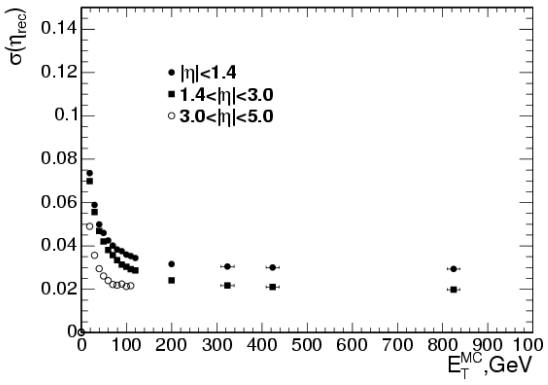

(a) η

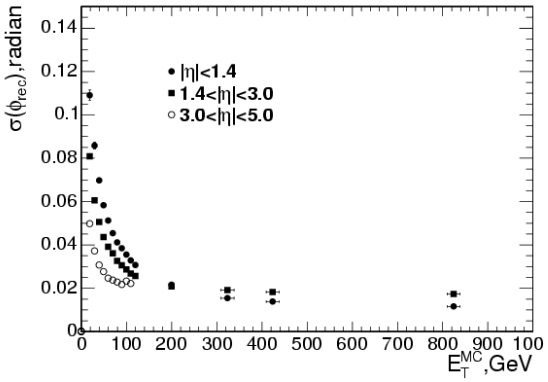

(b) ϕ

Figure 6.9: Angular resolution expected for IC($R = 0.5$) jets

neutrinos the kinematics is often unconstrained, but a cut on $|E_T^{miss}|$ is usually useful for rejecting the background. Beyond-SM scenarios usually have copious E_T miss sources, such as SUSY neutralinos or extradimension gravitons.

Unfortunately, detector effects can easily produce "fake" missing energy as the finite resolution breaks the balance between p_T; this is especially true for events with high E_T jets, as the total energy is obtained as sum of a large number of different vectors, sometimes poorly measured.

If one assumes that $\sigma(E_T) \propto \sqrt{E_T}$ for calorimeter hits, than a contribution to the missing energy resolution from the uncorrelated uncertainties on all the calorimeter cells can be estimated as:

$$\sigma(E_T^{miss}) = C\sqrt{\sum E_T}$$

As $|E_T^{miss}|$ is a positive variable, an average amount $< |E_T^{miss}| >$ of the order of $\sigma(E_T^{miss})$ is expected whenever the true missing energy is zero. Both these facts where observed in the UA1 and CDF experiments.

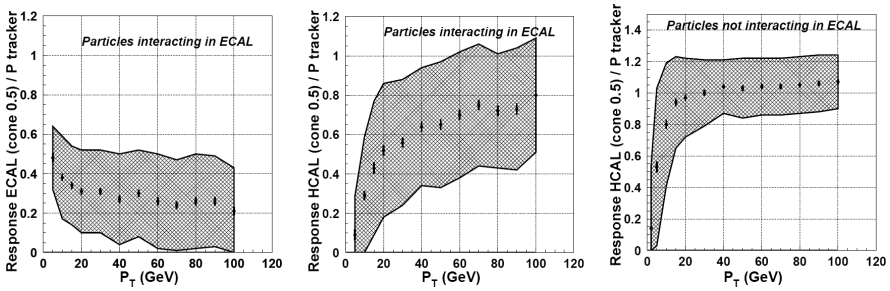

(a) ECAL resp. (b) HCAL resp. (c) HCAL resp.

Figure 6.10: (a) and (b) response in the ECAL and HCAL for pions interacting in ECAL, (c) response in HCAL for pions not interacting in ECAL; the shaded region is the RMS spread of the response.[CMS NOTE 2004/015]

E_T^{miss}in QCD jet events A study has been done on the expected E_T^{miss} resolution and the amount of "fake" E_T^{miss} for QCD di-jet events, using $3 \cdot 10^6$ fully simulated events with $\hat{p_T}$ ranging between 0 and 4 TeV, with low luminosity pileup (figure 6.11). The energy resolution can be fitted as a polynomial in $\sum E_T$

$$\sigma(E_T^{miss}) = 3.8\,\text{GeV} \;\oplus\; 0.97\sqrt{\sum E_T\,[\text{GeV}]} \;\oplus\; 0.012\sum E_T$$

where the constant factor is associated to noise, the stochastic one is from of the energy resolution on the single calorimeter objects, and the term linear in $\sum E_T$ is caused by containment and lack of a perfect hermeticity.

Applying corrections from jet calibration does not provide significant improvement to this resolution.

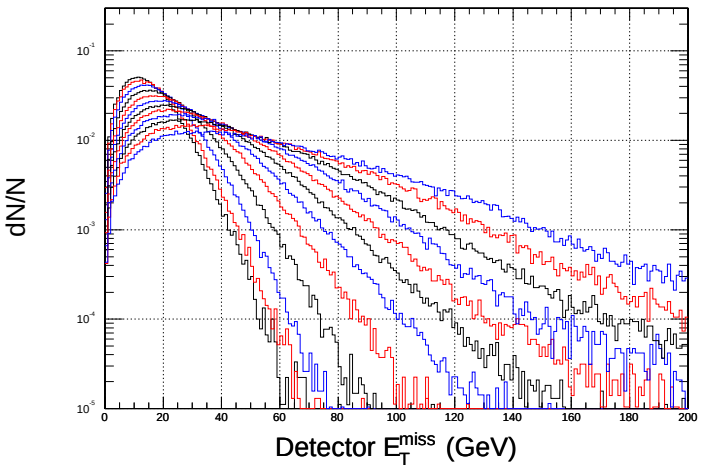

Figure 6.11: E_T^{miss} produced by detector effects in QCD multi-jet events with $\hat{p_T}$ in the ranges 20-30, 30-50, 50-80, 80-120, 120-170, 170-230, 230-300, 300-380, 380-470, 470-600 and 600-800 GeV.

E_T^{miss} in $t\bar{t}$ events In order to study events with real E_T^{miss}, a simulated sample of inclusive $t\bar{t}$ events was used. Also in this case, applying jet energy scale corrections does not improve the resolution significantly, but it corrects the average value of the measured E_T^{miss} which is otherwise only $\sim 90\%$ of the true value (see figure 6.12(b)).

Possible improvements While all these results use only the calorimeter information for determining the total $\vec{E}_T$ (except for muons), more advanced algorithms are under study using also tracker information, and taking into account calorimeter non linearities and the effects of the magnetic field[15].

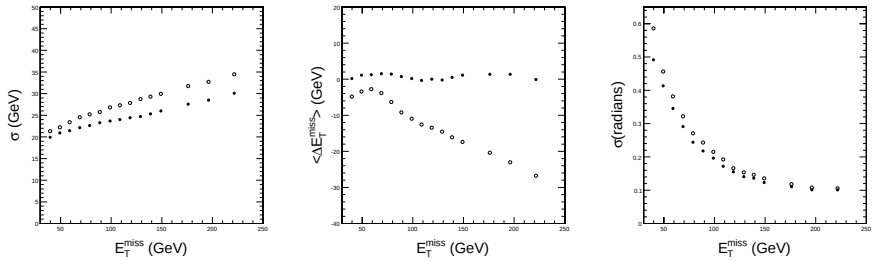

(a) Energy resolution (b) Energy error (c) Angular resolution

Figure 6.12: E_T^{miss} in inclusive $t\bar{t}$ events before and after the jet energy corrections (empty and full dots respectively). (a): E_T^{miss} resolution; (b) average error on $|E_T^{miss}|$; (c) average angle between the measured and true $\vec{E}_T^{miss}$ vectors.

6.9 Tagging of b-quark jets

Many interesting physics processes in the SM and beyond produce b quarks among the final state particles. In the processes of direct interest for this thesis, b quarks are produced in top quark decays $t \to W\,b$, and also directly in s-channel single top($qq' \to tb$).

While bottom quarks hadronize almost in the same way as lighter quarks do, jets from top quarks contain a B hadron, which often carries a large fraction of the initial parton momentum; by exploiting some general features such as the "long" B lifetime $c\tau \simeq 500\,\mu$m, large mass, the higher multiplicity of charged particles in the decay products or the presence of soft leptons from semileptonic b and c decays, it is possible to effectively distinguish jets originated from b quarks with reasonable accuracy; this procedure is called b tagging.

The b-tagging algorithms can be subdivided into three categories, if they use respectively: track impact parameters (IP), presence of a secondary vertex or presence of soft leptons.

[15] As particles with $p_T < 0.9\,\text{GeV}$ are bent back before reaching calorimeters, they contribute to the "fake" E_T^{miss}

6.9.1 Track impact parameter b tagging

Track selection This algorithm requires good quality tracks to perform well: at least eight tracker hits, including at least 2 pixel hits (crucial for impact parameter measurement) are required, $\chi^2/ndf < 10$, $p_T > 1\,\mathrm{GeV}$.

Tracks coming from other sources such as Λ^0 decays, photon conversions within the tracker or nuclear interaction in the beam pipe or pixel layers, are rejected by requiring a maximum transverse impact parameter of 2 mm.

Association of the tracks to the jet is done using a simple angular criteria, $\Delta R(jet, track)$, and typically used cone radii are 0.3 or 0.4.

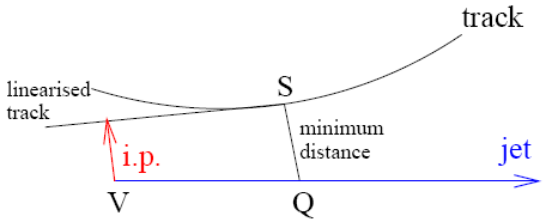

Figure 6.13: Three dimensional impact parameter. The signed flight path is the length of segment from V to Q measured in the jet direction

Signed track impact parameter A precise 3d reconstruction of the tracks allows not only to measure the transverse impact parameter between track and jet axis, but also the *flight path* of the particle, and to determine if the decay happened upstream or downstream with respect to the jet vertex. Physical flight paths are obviously always positive, but tracking resolution will cause the measured values for particles with short lifetime to be almost symmetrically displaced around zero, while longer lifetime particles will be found at positive flight paths.

As a convention common within b tagging algorithms, the sign of the flight path is propagated to the impact parameter, so that negative IP particles are those produced upstream.

Track counting The most basic b tagging criteria is just the number of tracks with positive impact parameter above some significance level. To reject tracks from other sources that would lead to an increased fake rate, tracks are required to have a distance of closest approach to the jet axis below 0.7 mm.

A continuous discriminant value, useful to compare the performance of different algorithms, can be obtained sorting the tracks by decreasing signed impact parameter significance, and using instead of the track count the significance of the n-th track, where usually n is often taken as two or three; in the results presented here the second track will always be used.

This algorithm is simple and reliable, and not dependent on complex calibrations, so it's used also in the first steps of the high level trigger.

Track probability A more advanced method uses the impact parameter to compute the probability of the tracks to come from the jet vertex.

Tracks with negative impact parameters are used as calibration source, as they provide half of the measured IP distribution for tracks with negligible true IP, and it is reasonable to assume that the positive half is symmetric. The probability of a track to come from the primary vertex is then computed using the extracted resolution function.

Finally, for a jet with multiple tracks, the confidence level for all those tracks to come from the jet vertex is a good discriminator; for convenience $x = -\log P$ is used as discriminating variable, so that light quark and gluon jets are clustered for small values of x while b quark jets have a larger x distribution.

The distributions of the b-tagging discriminator values for the different jet types are plotted in figure 6.14, while the performance for QCD jet samples can be found in figure 6.15.

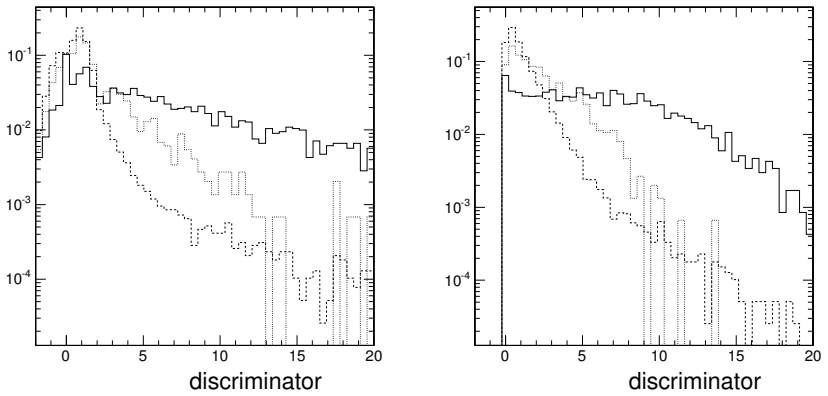

(a) Track counting ($n = 2$) (b) Track probability

Figure 6.14: Distribution of the b-tagging discriminator for track counting ($n = 2$) and track probability algorithms, for b-jets (solid), c-jets (dotted), $udsg$-jets (dashed)

6.9.2 Combined secondary vertex b tagging

Vertex classes Secondary vertices within jets can be searched using the Trimmed Kalman Vertex Fitter (described in section. 6.4.2). Jets can then be subdivide into three categories: "RecoVertex", jets with at least a real secondary vertex found; "PsedoVertex", jets for which no real secondary vertex is found but a pseudo vertex can be built from tracks not compatible with the primary vertex (signed IP significance > 2); "NoVertex" if not even two tracks are available in the jet to build a pseudo vertex.

Discriminating variables A multivariate discriminator is obtained by combining different variables: the number and the total invariant mass of all the charged particles associated to the real or pseudo secondary vertex, the ratio between their total energy and the energy of all tracks associated to the jet, the

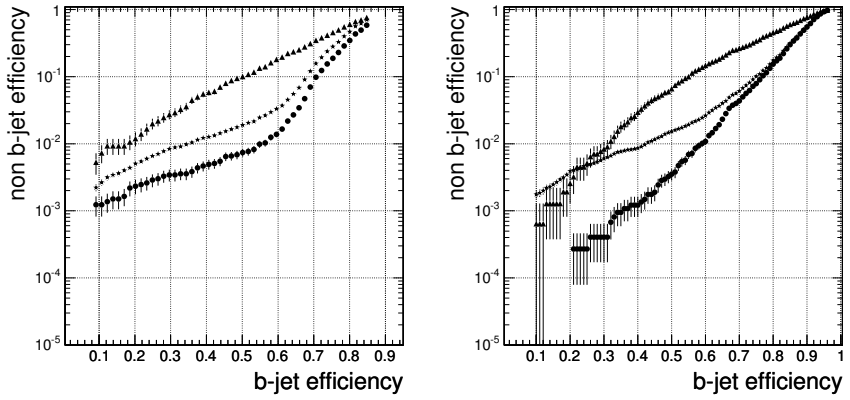

(a) Track counting (b) Track probability

Figure 6.15: Performance of track impact parameter b tagging algorithms on a QCD jet sample with $50\,\text{GeV} \leq p_T \leq 80\,\text{GeV}$, in the barrel ($|\eta| < 1.4$). In order of decreasing efficiency, jets from c, g and uds are plotted with triangles, stars and dots respectively.

significance of the transverse distance between the primary and the secondary vertex, the ratio between the energy of charged tracks associated the secondary vertex and the energy of all tracks associated to the jet, the rapidities of particles associated to the secondary vertex along the jet direction, and their transverse impact parameter significances.

Charm quark rejection To improve the rejection of jets originated from c quarks, an additional discriminating variable is computed: tracks are sorted by decreasing impact parameter significance, and the running total invariant mass is computed until it exceeds a threshold value associated to the c quark mass (usually 1.5 GeV) or all the tracks have been considered; the impact parameter significance of the first track which causes the running total to exceed the threshold, if any, is added to the discriminating variable.

Using simulated events, a combined likelihood ratio over all these variables, with E_T and η dependent distributions, can be extracted and used as final discriminator, up to possible riparametrizations and scale changes. The distributions of the discriminator variable for b, c and $udsg$ jets are plotted in 6.16(a).

This combined b tagging usually provides the best performance. Plots of the performance in QCD jet production and $t\bar{t}$ samples are shown in figures 6.16(b) and 6.18(b).

6.9.3 Soft lepton tagging

The branching ratio for semileptonic b quark decays is relatively high, about 19% for each lepton family if cascade decays $b \to c \to \ell$ are included; detection

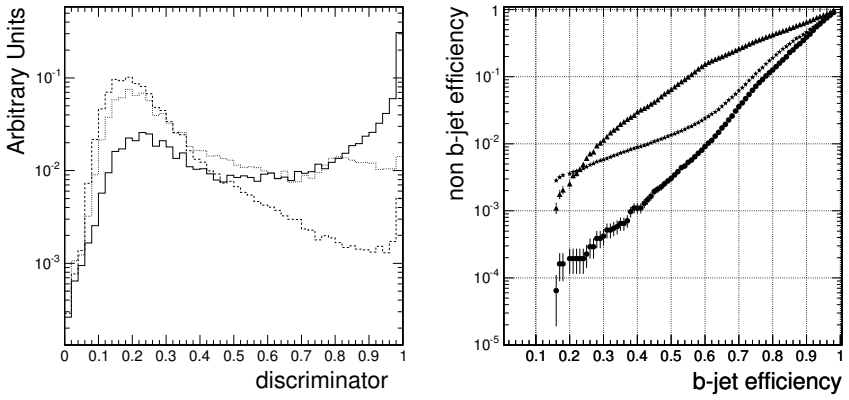

(a) Discriminator (b) Performance

Figure 6.16: Left) distribution of the discriminator value for b-jets (solid), c (dotted) and $udsg$ jets (dashed). Right) performance of combined secondary vertex b tagging algorithm; jets from c, g and uds are plotted with triangles, stars and dots respectively. Both plots are for QCD jet sample with $50\,\text{GeV} \leq p_T \leq 80\,\text{GeV}$, in the barrel ($|\eta| < 1.4$).

of soft leptons within a jet can be used to tag b jets even without the good impact parameter resolution that is absolutely necessary for the track and secondary vertex algorithms presented above, such as in the very first pixel-less data taking.

Muon identification Muon tracks with $p_T > 3.5\,\text{GeV}$ are easy to detect even within a jet, as a full track can be reconstructed in the muon chambers and extrapolated back in the inner detector to match with the jet; softer muons will often range out before the end of the chambers, so that a more difficult procedure has to be performed, extrapolating all tracks associated to the jet outward looking for hits in the chambers or examining energy deposits in the calorimeters.

The results presented here will use only tracks fully reconstructed in the muon chambers, but improvements will come along with the better muon identification algorithms hinted in section 6.6.

Electron identification Electrons are harder to reconstruct within jets as the associated calorimeter clusters must be separated from the nearby deposits from other jet particles. A neural network fed with many shower shape and cluster-track matching variables has been used; efficiencies between 60% and 70% can be obtained keeping the misidentification chance in the $1 - 2\%$ range.

Discriminating variables After lepton identification, a neural network is used to combine multiple discriminating variables: the lepton transverse momentum and angular separation relative to the axis given by the p_T weighted direction of the other tracks, the ratio between lepton momentum and jet energy, the significance of the three dimensional lepton impact parameter.

The algorithm performance for the two lepton flavours is plotted in figure 6.17 for a mixed jet and $t\bar{t}$ sample.

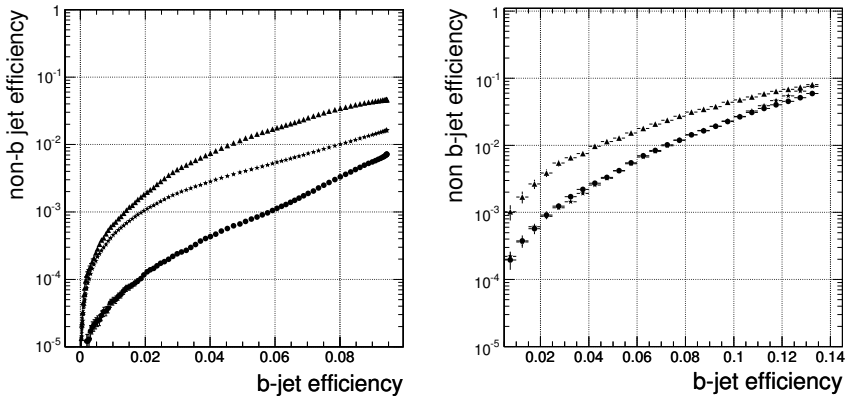

(a) Muon, $|\eta| < 2.4$ (b) Electron, $|\eta| < 1.4$

Figure 6.17: Soft lepton tagging performance using electrons and muons, on a mixed sample of QCD jet production and $t\bar{t}$

6.9.4 Performance of the algorithms

The performance of lifetime based algorithms has been tested on fully simulated events including low luminosity pileup for QCD jets and for semileptonic $t\bar{t}$ samples (figures 6.15, 6.16(b), and 6.18), while for soft lepton tags a mixed samples of QCD jet production and $t\bar{t}$ (figure 6.17).

In addition to detector resolution, a limiting factor is the presence of real detached vertices and tracks from the decay of long lifetime neutral particles (i.e. Λ^0 or K_L).

Worse performance for gluons than for uds jets is caused by the non negligible probability of gluon spitting into $b\bar{b}$ and $c\bar{c}$ pairs, and by the higher track multiplicity in gluon jets. Even worse rejection of charmed jets is caused by the comparatively large lifetime of D mesons ($c\tau = 310\,\mu$m and $120\,\mu$m for $D^{\pm}$ and D^0).

p_T and η dependence The dependence of the misidentification chance for constant b-jet efficiency of 50% on the jet p_T and η is plotted for the combined secondary vertex tag in figure 6.19: performance decrease at higher pseudorapidities is caused by the increased material budget; greater misidentification chance at very low and very high E_T is respectively due to the increased contribution of multiple scattering on the vertex and impact parameter measurements, and to the increased probability of gluon splitting in heavy flavours and track multiplicity. This behaviour is common to all lifetime based algorithms.

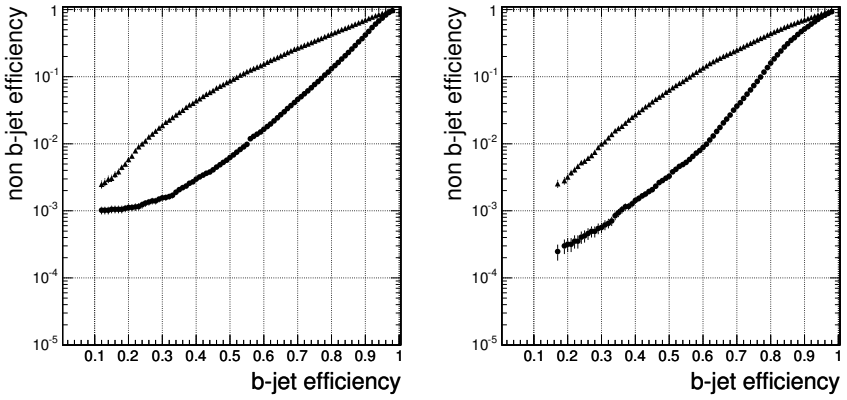

(a) Track probability (b) Combined sec. vertex

Figure 6.18: Performance of lifetime based b tagging algorithms on a semileptonic $t\bar{t}$ sample, in the barrel ($|\eta| < 1.4$) and for $p_T > 30\,\mathrm{GeV}$. In order of decreasing efficiency, jets from c and uds are plotted with triangles and dots respectively.

Alignment Simulations have been made to determine the degradation of b tagging performance at different alignment scenarios, first data taking ($L < 1\,\mathrm{fb}^{-1}$) and long term ($L \geq 10\,\mathrm{fb}^{-1}$). For constant value of the b jet efficiency, no appreciable variation of the mistagging efficiency for c jets has been found, and even for light flavours the performance is only slightly worsened, and only in the first data taking scenario.

Vertex-less tagging In a pixel-less scenario the expected resolution on the impact parameter is $\sim 1\,\mathrm{mm}$, so that lifetime base methods cannot be used. A variant of the soft lepton tagging has been designed specifically for this scenario: using only muons, mistag rates factors of $10^{-3}/5 \cdot 10^{-3}$ of $udsg$ can be achieved for a b-jet efficiencies of 5/10% and c jet mistag rates 1.5%/4% in the whole range $|\eta| < 2.4$; adding the semileptonic decays into electrons should allow to nearly double the efficiencies (and mistag rates).

Performance studies with data A study on the possibility of the b-tagging efficiency measurement using data has been carried on, based on the selection of semi-leptonic and di-leptonic $t\bar{t}$ events that provide a sample of b enriched jets. The expected accuracy on the b tagging efficiency for different values of E_T are plotted in figure 6.20; systematic uncertainties from initial and final state radiation, background cross sections and Monte Carlo knowledge of the sample purity have been included, while the other factors have been found to be negligible or are expected to be so.

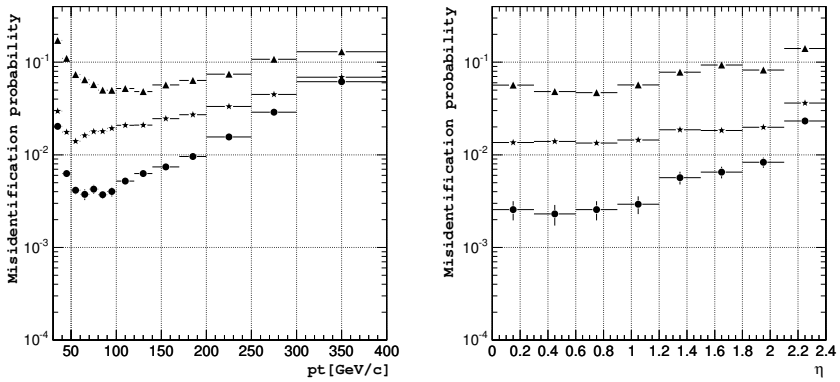

(a) Jet p_T (b) Jet $|\eta|$

Figure 6.19: Mistag ratio of the combined secondary vertex b tagging, for a constant efficiency of 50%; left) as a function of p_T, for $|\eta| < 2.4$; right) as a function of η, for $50\,\text{GeV} \leq p_T \leq 80\,\text{GeV}$. In both cases, QCD jet samples have been used

6.10 Luminosity measurement

An accurate luminosity measurement is required in order to extract meaningful cross sections from event counting; it is necessary to have both a fast measurement of (relative) instantaneous luminosity, extracted realtime with 1% statistical accuracy every 0.1 s, and an accurate offline determination of the absolute integrated luminosity with a total uncertainty of some percents. Knowledge of the former is important for monitoring, and also because it affects the amount of pileup superimposed to the hard physics events, which can alter significantly the efficiencies of selections sensitive to soft jets ($p_T \lesssim 30\,\text{GeV}$).

6.10.1 Online methods

The most basic method for luminosity measurement is event counting: any sort of fast detector is used to count the rate of events, as the instantaneous luminosity is proportional to the event rate. This allows to measure only the relative luminosity, as the cross section and efficiency for such events cannot be computed with good accuracy, but the absolute luminosity scale can be determined on much larger time scales by the use of offline methods.

Events with very simple signatures, such as anything that produces an amount of E_T above some threshold in forward calorimeters, and with large cross sections are used, in order to achieve high statistical accuracy in a short time.

Zero counting The problem with the above method at high luminosity hadron colliders is that multiple events may happen in the same bunch crossing, but it might be hard for the detector to disentangle them; for example at LHC, in the high luminosity regime, 25 inelastic pp interactions are expected at every bunch

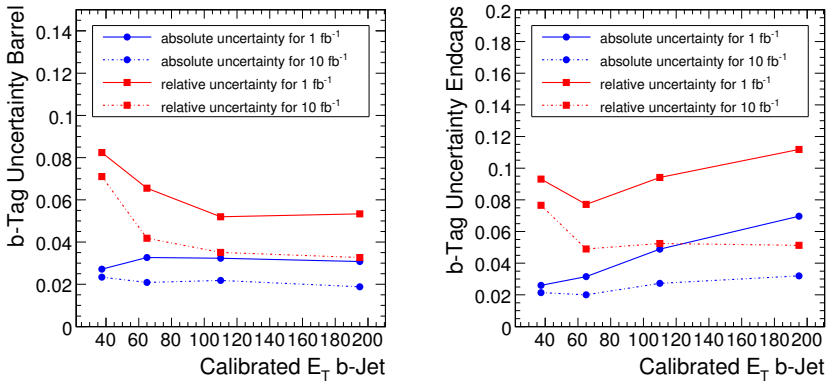

(a) Barrel (b) Endcaps

Figure 6.20: Uncertainty on the b tagging efficiency extracted from data for $1\,\mathrm{fb}^{-1}$ and $10\,\mathrm{fb}^{-1}$ integrated luminosity, in the barrel ($|\eta| < 1.5$) and in the endcaps ($|\eta| > 1.5$)

crossing. Anyway, it is usually very simple to determine if at least one event has happened in any given bunch crossing, i.e. by summing up energies over the whole calorimeter, so the improved version of the event counting method is based on counting bunch crossings with no interaction at all: by assuming Poisson statistics, the average number of events per bunch can then be computed.

Anyway, when luminosity is very high, the probability of no interaction at all is tiny, and the method looses statistical power ("zero starvation"); in addition, whenever this fraction becomes too small the systematic uncertainty on it will become unacceptably large, so that more sofisticated methods must be used, which will be described in the following.

HF luminosity monitoring The forward hadron calorimeter is well suited for luminosity monitoring with zero counting techniques.

Two additional improvements have been thought to increase performance and avoid succumbing to zero starvation. The first is based on determining separately the probability of an energy deposit below threshold in each HF tower; as the average occupancies of all towers are nearly the same, this method increases the number of (nearly) independent event counting experiments, and thus the statistical power of the technique.

The second method relays on the fact that the maximum E_T deposit from a single event in the HF is kinematically limited by the $|\eta|$ range to a few hundred of GeV; counting the total E_T collected in all HF towers provides then a lower limit on the number of events originated by the single bunch crossing, and can thus be used for luminosity measurements.

Pixel luminosity telescope The PLT is a special device, yet to be approved, which would allow another precise measurement of luminosity and interaction point centroid. It is based on three planes of special diamond pixels, much more radiation hard than silicon ones and with nearly 100% detection efficiency,

bump bonded to the traditional CMS pixel readout system and installed in the forward region, at $z = 1.65\,\mathrm{m}$, $r \sim 45\,\mathrm{mm}$ (which corresponds to $\eta \sim 4.3$), projective towards the nominal interaction point. A fast readout, suitable for

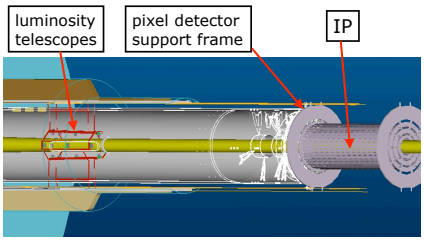

Figure 6.21: Location of the pixel luminosity telescopes within CMS

all bunch crossings, uses the triple coincidence of hits in the PLT planes; relative luminosity is then estimated by track counting.

At a reduced frequency, once for every L1 trigger accept, the whole system can be read out allowing even for full tracking of the event to pinpoint the sources of the particles, allowing even to spot detached tracks coming from interactions between halo particles and the beam pipe.

6.10.2 Offline methods

Z and W production The electroweak cross sections for inclusive Z and W production are large and known with relatively good accuracy, so that event counting can provide a precise offline determination of the integrated luminosity.

The main uncertainties come from detector acceptance and especially parton density functions (PDFs); undergoing studies suggest that the total uncertainty on integrated luminosity can be constrained to the few percent level, but at the moment a conservative value of $\pm 5\%$ at $10\,\mathrm{fb}^{-1}$ (3% at $30\,\mathrm{fb}^{-1}$, 10% at $1\,\mathrm{fb}^{-1}$) is used in the physics results.

Parton density functions are a sizable source of uncertainty in many cross section measurements, but for some processes it might be possible to cancel out this uncertainty if W and Z production are used to constrain not just integrated luminosity but also the differential parton luminosity, allowing for $\delta\sigma/\sigma \simeq 1\%$

TOTEM TOTEM is another experiment, independent from CMS but situated at the same LHC interaction point, dedicated to the study of diffractive proton collisions [TOTEM]. It should be able to measure the total pp cross section in a luminosity-independent way through dispersion relations and optical theorem, and through this knowledge the integrated luminosity can be constrained within $\approx 1\%$, as TOTEM and CMS will be observing simultaneously the same events.

Unfortunately TOTEM can operate only at low luminosity and with a different beam optics than the one used for normal CMS physics runs, and thus the luminosity calibration from TOTEM has to be extrapolated largely.

Chapter 7

CMS Trigger

In a high luminosity collider the trigger system is extremely important: the total inclusive rate of events in CMS is $\sim 10^9$ Hz, while the maximum rate at which events can be written to persistent storage is ~ 100 Hz, as the event size is roughly 1 Mb even after zero suppression and data compression.

In order to achieve the needed 10^7 rejection factor, trigger is divided in two parts: a fast level 1 (L1) trigger implemented in custom electronics and working in pipeline at 40 MHz with no deadtime, providing the first 10^4 suppression; ad a high level trigger (HLT) implemented in software in a large computer farm with fast interconnections.

As it is not known what physics will show up at LHC, the trigger must be extremely flexible, tunable for the best performance after the first data taking has shown what are the most important physics channels to focus on.

Measurement of the trigger efficiency using data is important to reduce systematic uncertainties in the measurements, and so many trigger channels must be available with rate prescaling to allow a continuous monitoring from the neatest event signatures down to minimum bias events. In addition, trigger must also be able to select special samples for detector alignment and calibration.

7.1 Level 1 trigger

7.1.1 Requirements and overview

Trigger processing at level 1 is extremely critical because of the high rates. To avoid loosing events, processing must be done in a synchronous pipeline; single subdetectors can buffer locally up to 128 bunch crossings, 3.2 μs, and almost 2 μs are lost in transferring the data and control signals from the detector to the trigger electronics, so that the total maximum processing time is limited to one microsecond.

Processing in pipeline the data of multiple bunch crossings at 40 Mz requires that the data flow within electronics is always the same for each event; in addition, the time spent in any reconstruction step must be constant, which forbids iterative algorithms.
Great focus has been placed on using *inclusive* and *local* trigger algorithms, so that processing separate detector regions can be done in parallel with no

problems. The only global objects are, for obvious reasons, total and missing E_T.

To allow easy tuning of the trigger, trigger candidates such as jets or muons are just sorted forwarding the four best ones to the next step, and cuts are applied only at the end.

7.1.2 Trigger L1 objects

At level 1 only the information from the muon chambers and the calorimeters, with reduced granularity, are available; this reduces the trigger objects to just a few.

Electrons and photons both are seen as particles that produce a large deposit in the electromagnetic calorimeter and not in the hadronic one; tracking is impossible at this step, and there is no way to tell the difference between electrons and photons. Calorimetric isolation, by vetoing the energy deposit in HCAL and requiring a more localized shower in ECAL, is essential to reduce the background from QCD jets.

Muons Muons have a cleaner signature than electrons, and can be reconstructed also when not isolated (useful for B physics)

Jets Jets can be reconstructed with a simple "sliding window" summation on the calorimeter towers (see 6.7.1); jets in the forward region ($3 \leq |\eta| \leq 5$) are kept separate from the others, as different trigger requirements might be imposed on them. With no tracker information b tagging cannot be performed at L1.

Taus Hadronic decays of the tau produce narrower jets than the usual parton hadronization; as a rough τ/jet separation can be performed using only calorimeter information, τ candidates are available even at L1.

E_T **sums** The total E_T, obtained by scalar summation over all the towers, can be used to select generically "hard events" expected from many BSM scenarios. Even more useful is the missing transverse energy E_T^{miss}, the opposite of the vector sum of all E_T in the event, associated to neutrinos and possible other neutral particles with no strong interactions (such as SUSY neutralinos)

7.1.3 Trigger L1 steps

Muon DT/CSC Trigger Track segments are build locally by each DT and CSC station; then the regional track finders combine matching segments to obtain the muon tracks and the associated p_T (track segments may be exchanged between DT and CSC reconstruction in the transition region between the two), sorts candidates by p_T and deliver the best four both for the barrel and the endcaps to the global muon trigger.

Muon RPC Trigger RPC trigger system looks for hit patterns among the RPC cells and uses lookup tables to extract a p_T range for the pattern; as above, the four best barrel muons and the four best encap muons are forwarded to the global muon trigger

Global Muon Trigger Muon candidates from the two different subsystems are compared and, if possible, matched; candidates are accepted if seen from both systems, or just from one but with good track quality (χ^2), to increase efficiency and remove ghost tracks.

In addition, the GMT receives from the calorimeter trigger a map of the quiet regions and the MIP regions, where the energy deposit is compatible to that of a minimum ionizing particle, to perform isolation cuts. The four highest p_T muons, both isolated and not, are sent the global trigger.

ECAL Triggers Energy deposits in strips of five crystals along the ϕ regions are summed, and then towers are formed by summing five strips along η. In order to generate an electron or photon candidate, cuts are applied on total energy deposit, lateral shower profile (energy ratio between two neighbouring strips and the whole tower) and on the HCAL deposit in the same region.

Isolation requires also, in the eight surrounding towers, cuts on ECAL and HCAL deposit, and the absence of a MIP candidate in those regions. Non isolated clusters are accepted if the energy saturates the trigger scale $E_T = 63.5\,\text{GeV}$; this allows to increase the efficiency for high energy electrons and photons, as background contribution is small at these energies. .

Jet Trigger Energy deposits are summed over regions of 4×4 towers including both ECAL and HCAL energy; then, using a sliding window approach, groups of 3×3 regions are selected as jet candidates if the central region has a higher ECAL + HCAL deposit and there is no electron/photon candidate found there.

Tau tagging at L1 A 4×4 tower region is flagged with τ-veto if there are more than two active towers; a jet is tagged as tau if all the 9 regions are not flagged.

Quiet and MIP regions If a 4×4 region has total E_T below some threshold is marked as quiet for muon isolation cuts; in addition, a MIP flag is set in calorimeter towers where the energy deposit is compatible with that of a minimum ionizing particle, and an entire region is flagged as MIP if there is at least one MIP-like tower in it. This information is forwarded to the global muon trigger.

Global trigger The Global Trigger receives the trigger candidates from the different subsystems, and builds the two global objects $\sum |E_T|$, E_T^{miss}; this is the only step at which threshold cuts are applied to candidates to select or reject the event.

Trigger primitives are kept, even if they are not the ones causing the decision to accept the event, as they will be used as starting points for HLT reconstruction.

A block diagram of the level 1 trigger is presented in figure 7.1.

The logic of the global trigger is entirely implemented on programmable devices (FPGA) so that it all the decision making process can be updated for the new physics that might show on.

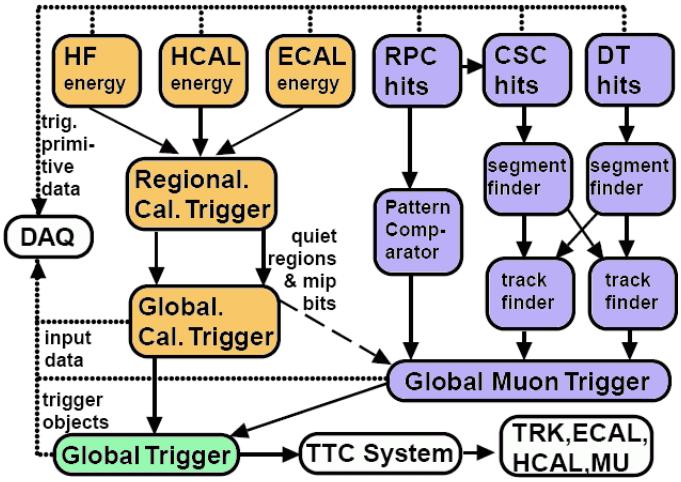

Figure 7.1: Trigger L1 structure

7.1.4 Trigger L1 rates

The maximum data rate allowed as input to the HLT is 100 kHz, but for the first years at low luminosity part of the HLT computer farm won't be installed yet and so the maximum rate is fixed to 50 kHz; this rate has further been divided by a safety factor 3, and thresholds have been chosen so that the expected rate is 16 kHz.

When LHC will reach the design luminosity of $10^{34}\,\mathrm{cm}^{-2}\mathrm{s}^{-1}$ the full HLT and DAQ will be available, and the maximum allowed rate for trigger level 1 will be raised to $\simeq 33$ kHz.

The total rate has been shared almost evenly among electron/photons, muons, taus and jets or composite triggers: jet $*$ E_T^{miss}, $e/\gamma *$ jet and $\mu *$ jet for high luminosity only. The thresholds and the expected inclusive rates for each channel are listed in table 7.1.

7.2 High level trigger

7.2.1 Implementation

The high level trigger (HLT), sometimes also called event filter, receives the 100 kHz input from the level 1 trigger and has to reduce this up to the final rate of events to be stored on tape (100 Hz).

The CMS implementation of this trigger differs from the one used in many other experiments.

Table 7.1: Trigger level 1 thresholds and rates

	Threshold [GeV]		**Inc. Rate** [kHz]	
Channel	Low L	High L	Low L	High L
Inclusive isolated photon	29	34	3.3	6.5
Di-electrons/photons (isol.)	17	19	1.3	3.3
Inclusive isolated muon	14	20	2.7	6.2
Di-muons	3	5	0.9	1.7
Single tau-jet	86	101	2.2	5.3
Two tau-jets	59	67	1.0	3.6
1, 3 of 4 jets	177,86,70	250,110,95	3.3	3.0
Jet $*$ E_T^{miss}	$88 * 46$	$113 * 70$	2.3	4.5
Electron/photon $*$ Jet	$21 * 45$	$25 * 52$	0.8	1.3
Muon $*$ Jet	–	$15 * 40$	0.8	0.8
Minimum bias, calibration	–	–	0.9	1.0

The first difference depends on the implementation: after level 1, all operations are implemented by software on a farm of ordinary computers, to allow for maximum flexibility of the algorithms and easiness of upgrade (is just a matter of adding computational elements to the farm).

The second difference, possible because of the first one, is that there is no hard separation between steps ("level 2", "level 3", ...), the event is reconstructed starting from the fastest detectors (calorimeter, muon chambers) and proceeding down to the slowest ones (pixel and then tracker) and the event is discarded as soon as the partial reconstruction is sufficient to reject it. At the moment calorimeter only steps are called "level 2", pixel ones "level 2.5" and full tracker information "level 3", but the order in which steps are done is flexible, and can be changed if faster algorithms are discovered to allow usage of more complex information at an earlier stage. This partial reconstruction allows to have as much as $\simeq 1$ s processing time in HLT, as most of the events are rejected after a tiny fraction of this time freeing the associated computing resources for the events more difficult to reconstruct.

In addition to reconstructing events only "as much as needed" for an accept or reject verdict, regional reconstruction is used to reduce the necessary processing time. All the candidate objects from trigger level 1, even those which did not cause the accept decision, are used as seeds for starting HLT reconstruction; this is particularly useful for the use of the tracker in isolation and b tagging, restricting track finding just to a cone around the L1 object.

7.2.2 HLT isolation cuts

In addition to improving the measurements of the trigger objects from L1 up to a level that almost matches the quality of offline reconstruction, the big improvements of HLT are in the isolation and tagging cuts.

Calorimeter isolation The use of the full granularity of the calorimeters can increase the effectiveness of the isolation cuts, as cones centered on the

objects are less sensitive to pileup and noise than the large regions used at L1; in addition, the energy from the object itself can be subtracted more accurately using the energy deposit in smaller cone. The additional background rejection obtained is not very large (usually a factor 2–3) but helps in cutting down the number of events for which the slower isolation algorithms have to be used.

Pixel isolation Pixel detectors have 2d hits, so that a simple track reconstruction with just three layers can be implemented with a short processing time. As track vertexes can be reconstructed, albeit with a worse resolution, the tracks not associated with the signal object vertex can be ignored, further reducing the dependence of the algorithm on pileup and underlying events (UE). In addition, the knowledge of the z of the vertex increases the knowledge of the E_T of calorimeter objects, which is otherwise degraded by the 5.3 cm z spread of the interaction region.

Track isolation Restricting the track finding to a cone and applying calorimeter isolation first allows the use of track reconstruction for isolation within the available processing time: usually a small number of hits is already sufficient to determine the track orientation and p_T with sufficient accuracy for this purpose. Just as for pixel, vertex association helps against pileup and UE.

It should be noted that slower algorithms work almost as well for selection of double objects (i.e. the di-tau trigger) than for single ones, as the reconstruction for isolation on the second object is applied only if the first one passed the selection, so that the number of events has already been much reduced.

The three isolation steps are not necessary stacked: usually only the calorimetric and one of the two tracking based isolations is enough to reduce the backgrounds; the choice among the two tracker ones is done for each specific channel by looking at the speed vs. efficiency trade-off.

7.2.3 b tagging at HLT

Many interesting physics channels have b quarks in the final state and no other objects suitable for triggering (i.e. $h \to b\bar{b}$, or fully hadronic $t\bar{t}$), so that a fast b tagging implementation at HLT can allow to recover signal efficiency for these events.

Pixel b tagging In order to work at the first stages of HLT, at a 1 kHz rate, only pixel information can be used; primary vertex finding is necessary for b tagging, but it is enough to reconstruct just the z position for which the spread is larger, and this can be performed quickly with just pixel tracks (see 6.4.3). The track counting algorithm (see 6.9.1) was chosen as it is fast enough, and fairly robust due to its lack of dependence on the calibrations; by requiring at least one of the two leading jets to be tagged, a background rejection of a factor 5 is expected.

Tracker b tagging Standard track reconstruction can be attempted after pixel b tagging and by limiting the region to $\delta\eta \times \delta\phi = 0.4 \times 0.4$, $p_T(trk) > 1\,\text{GeV}$ and to tracks compatible with the vertex reconstructed using pixel information;

additional time saving can be obtained by stopping the reconstruction as soon as a sufficient accuracy on the track parameters is available (usually with 8–10 hits). This provides an additional background rejection of 4, while the efficiency for samples with real b jets is almost unchanged

7.2.4 τ tagging at HLT

Tau tagging at HLT is done mostly through isolation cuts, as the majority of hadronic tau decays have only one charged track, or three close ones, plus any number of π^0 photons; the more advanced τ tagging techniques are not needed, as the rate is already small enough.

Reconstruction is attempted looking for a hard track within $\Delta R = 0.1$ from the calorimeter tau jet; the total p_T of all the tracks found in a $\delta R \sim 0.4$ isolation cone around the calorimeter jet axis, excluding a small cone around the track ($\delta R = 0.07$), is calculated and compared with a threshold (1 GeV).

If only one tau candidate has been found at trigger level 1, a second tau is anyway searched for at HLT, by rerunning reconstruction and isolation cuts on the hardest central jet which was not τ tagged at level 1, recovering some efficiency in the di-tau channel; if a second tau is not found after this procedure, a cut on E_T^{miss} is applied to require the presence of a neutrino in the event.

7.2.5 High level trigger thresholds

The high level trigger has a large number of channels, including those limited to specific processes like $B_s \to J/\psi K_S$, and the algorithms and thresholds used are continuously improved as the analyses proceed; because of this, only the more general samples have been considered here.

A list of the HLT thresholds is provided in table 7.2.

Table 7.2: Threshold for some of the more general HLT channels, updated in [PTDRv1]

Channel	Threshold [GeV]	
	(single)	(double)
Electron	26	12
Muon	19	7
Photon	80	30,20
Jet $*$ E_T^{miss}	$180 * 123$	
1, 3, 4 jets	625, 247, 113	
b jet	237	

7.3 Trigger efficiencies

As a conclusion to this short description of the CMS trigger, the efficiencies for some reference physics signals will be presented.

Muon stream The three benchmark processes for muon efficiencies are $H \to WW^* \to \mu\mu\nu\nu$, $H \to ZZ^* \to 4\mu$ and $Z' \to \mu^+\mu^-$. At level 1, at a luminosity of $2 \cdot 10^{33}\,\mathrm{cm}^{-2}\mathrm{s}^{-1}$, the expected net efficiencies are 97.6%, 100% and 99% ($m_{Z'} = 3\,\mathrm{TeV}$) if all the final state muons are within the geometrical acceptance $|\eta| < 2.4$.

At HLT the efficiencies are still very high: for the first channel, 92% efficiency in the inclusive single muon channel and 80% efficiency in the dimuon one is estimated, including the geometrical acceptance; for the second channel is $\gtrsim 98\%$; finally, in the third channel it is $98 - 95\%$ for $m_{Z'} = 1 - 5\,\mathrm{TeV}$ if the events are within the geometrical acceptance (which happends in $80 - 95\%$ of the events, for $m_{Z'} = 1 - 5\,\mathrm{TeV}$).

Electron and photon stream Four processes have been considered for efficiency studies: $W \to e\nu$, $Z \to e^+e^-$, $H \to \gamma\gamma$ and $H \to ZZ^* \to 4e$. The total efficiencies for L1 and HLT, split between electrons and photons, are listed in table 7.3. The high efficiency of the multiple electron signals in the HLT photon channel is due to the fact that no track-supercluster matching is required for di-photon trigger, as the background is already low enough.

Table 7.3: Trigger efficiencies in the e/γ stream

Process	**L1 e/γ**	**HLT 1e + 2e**	**HLT 1γ + 2γ**
$\mathbf{W \to e\nu}$	90.0%	68.0%	—
$\mathbf{Z \to e^+e^-}$	97.1%	89.5%	59.6%
$\mathbf{H \to 4e}$	96.5%	90.2%	70.0%
$\mathbf{H \to \gamma\gamma}$	99.7%	—	88.4%

Tau stream The di-tau channels have been studied in the MSSM process $gg \to b\bar{b}A$, $A \to \tau\tau$. As the efficiency depends on m_A, three different values where used $(200, 500, 800\,\mathrm{GeV})$ At L1 the efficiencies are 51%, 85% and 90%, the smallness of the first being explained by the high p_T thresholds; at HLT efficiencies are all similar $\simeq 30\%$.

Analogue studies have been performed for single tau signals in the MSSM, $gg \to tbH\pm$ followed by $H^\pm \to \tau^\pm\nu$. In the mass range $m_{H^\pm} = 171 - 400\,\mathrm{GeV}$ the L1 efficiency is $54 - 76\%$, and reduces to $17 - 42\%$ after HLT.

Chapter 8

Appendix: inner tracker integration and burn-in

Integration and testing of parts of the inner tracker have been performed in the INFN Pisa - San Piero a Grado laboratories; this includes also the final burn-in of fully integrated structures (TIB layers or TID disks).

As I had some first hand experience in some these tasks, a brief description of some issues will be given here.

8.1 Integration database

To follow the complex procedure of TIB/TID integration and testing, a SQL database is used to store all information. In particular, this database contains:

- The logical structure of the different parts (TIB, TID, DAQ crates, ...)
- Information on each component (for instance, depletion voltage for the modules)
- The inventory for each component, tracking the location where it is stored and its status (mounted, in stock, faulty, ldots)
- Status of the integration: for each logical position, the ID of the mounted component is registered.
- Connectivity: every single connection among signal and power cables is registered, so that when a faulty transmission is found, all the connections on the path can be examined.

The database is usually accessed through a graphical user interface written in Java, that allows to perform the common tasks in an user friendly way without requiring the knowledge of the deep structure of the database, and allowing for validation of the user input. The client is also able to connect to the central database in Lyon to download the informations on the single components and import them in the inner tracker database.

During this year I have been able among the maintainers of the integration database and its client; in addition to routine tasks and bug fixing, I was able

to introduce some improvements, like inserting new structures in the database, and adding features to the client to speed up the otherwise very lengthy and tedious procedure of registering all the hundreds of connections necessary for the burn-in of each tracker structure.

8.2 Tracker burn-in

8.2.1 Burn-in procedure

After the structure has been fully connected to the data acquisition, control, power and cooling lines, the FEC (front end controller) is used to send I^2C messages to all the tracker electronics; this allows to immediately spot modules with faulty chipset or other problems in the control channels.

By using the temperature sensors mounted in the tracker, one can measure the effectiveness of the cooling device, which is critical for the operation of the modules.

In order to test that also all the data connections are correct, again a control signal is sent to all AOHs (analog opto-hybrids) in succession, which now respond with optical signals on the data line; as only one AOH responds at each control signal, the full map of the associations between AOH control addresses and output data lines can be built, which can be checked against the tracker integration database to spot wrong connections.

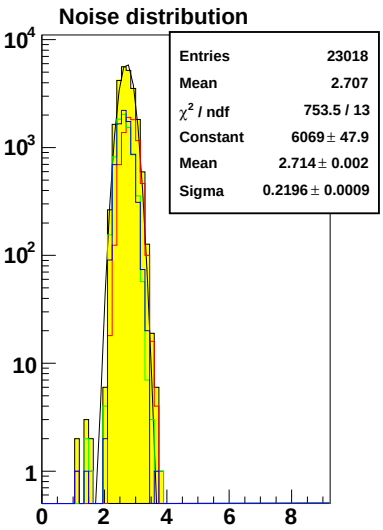

Figure 8.1: A sample noise distribution, in ADC counts.

Time alignment of all the modules follows: as analog signals from AOH are preceded by a digital header which clearly stands out over the noise, this can allow to determine precisely the delays introduced by the interconnections and adjust the time offsets so that signals from all the modules reach the DAQ synchronized.

Each AOH can operate using four different amplifications over the optical link; the choice of the gain is done in order to have similar output signals at the FED (front end digitizer), which could require different gains if the fibers and connections have better or worse light efficiency. The calibration is done using again the digital header in AOH signals, which are emitted by the AOH with fixed pulse height. If an AOH is found to have very low output signals, the path of the light through all the cables, obtained by the integration database, can be checked, and faulty or badly connected fibers can be fixed.

After the correct gain has been chosen in the above step, the scale used in ADC conversion within the FED can be calibrated to assign an equal number of ACD counts to a reference pulse height; the scale is often chosen so that it is saturated by the signal of eight minimum ionizing particles.

The final step in normal burn-in is the pedestal measurement: in the absence of signal, the fluctuations of the analog signals are recorded, and the distribu-

tion of the noise can be extracted; this includes both strip-by-strip noise and common-mode noise, which (by definition) affect all strips within a module equally. Measurements of the noise have been very useful to choose the best grounding schemes to be used. Pedestal drift is also important to determine the stability of the electronics.

An example of the noise distribution seen at burn-in, is shown in figure 8.1, measured for a part of TIB layer 3 with the electronics working in peak mode.

8.3 Cosmic muon burn-in

Cosmic rays provide a decent source of muons which can be used to test the response of silicon modules to the signal of minimum ionizing particles; plastic scintillators are used to provide a trigger system. The signals clearly stand out over the background, with $S/N \gtrsim 22$ (figure 8.2(a)).

Recently, cosmic muon data has been taken in a setup with four TIB layers, so that it was even possible to perform track reconstruction on these events within the CMSSW framework (see figure 8.2(b)), even if some tweaking of the reconstruction code to allow for tracks which don't obey to any vertex constraint.

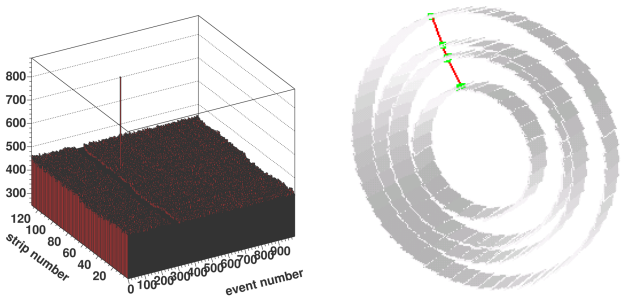

(a) Single layer μ (b) Reconstructed track

Figure 8.2: (a) Plot of the signal measured on each strip of a module as a function of time; the passage of the muon is visible as a narrow spike; (b) A track from burnin with cosmic muons, reconstructed with CMSSW and plotted using IGUANA, the CMS visualization tool.

Part III

Single top quark physics at CMS

Chapter 9

Before LHC: single top searches at Tevatron

9.1 Overview

At Tevatron single top quark production differs with respect to LHC, as the hierarchy of production cross sections is different: t channel has the largest cross section ($\sigma_t^{\text{Tev}} = 1.98\,\text{pb}$), the one of s channel is almost half ($\sigma_s^{\text{Tev}} = 0.89\,\text{pb}$, and the tW cross section is much smaller ($\sigma_{tW}^{\text{Tev}} = 0.13\,\text{pb}$); the $t\bar{t}$ background cross section is slightly more than twice the combined single top channels ($\sigma_{t\bar{t}}^{\text{Tev}} = 6.7\,\text{pb}$). $W + jets$, including heavy flavours such as $Wb\bar{b}$, are the major backgrounds to single top searches.

The most recent results are from CDF ([CDF]), using an integrated luminosity of $\sim 700\,\text{pb}^{-1}$ from Tevatron Run II.

9.2 Data selection

Trigger At CDF single e and single μ triggers require $p_T > 18\,\text{GeV}$, $|\eta| < 1$; an additional $e \cdot E_T^{miss}$ trigger selects forward electrons ($1 < |\eta| < 2$, $p_T > 20$) if $E_T^{miss} > 15\,\text{GeV}$.

Selection cuts

- **Lepton** $p_T > 20\,\text{GeV}$. If two leptons are found, the region $M_{ll} = 91 \pm 15\,\text{GeV}$ is excluded to reject Z events.
- **Neutrino** $E_T^{miss} > 20\,\text{GeV}$, as leptonic decays must contain at a neutrino.
- **Jets** Exactly to jets, with $p_T > 15\,\text{GeV}$, $|\eta| < 2.8$. At least one jet must be b-like. An additional constraint $0.5 < \Delta\phi(E_T^{miss}, \text{leading jet}) < 2.5$ provides rejection against non-W backgrounds where a fake E_T^{miss} signal is produced by the finite jet energy resolution.

After all selections cuts, the expected number of events is 28.2 for single top signal and 645.9 for background. 26% $Wb\bar{b}$, 20% $Wc\bar{c}$, 6% $t\bar{t}$, plus 20% events from QCD jet production where a light quark jet is mistagged as b-like and

another 25% from the same source where a jet is misidentified as a lepton.

Kinematic fitting In order to improve the resolution in the kinematic variables by means of redundant measurements, the values for the top quark decay products momenta are obtained through a constrained χ^2 fit. The less precisely measured parameters are P_b, $|E_T^{miss}|$, $\phi_\nu = \phi(E_T^{miss})$, and $P_z(\nu)$ can be reconstructed only up to a twofold ambiguity by imposing the M_W mass constraint; for each choice of the sign of the neutrino P_z and of the jet to pair with the W, a χ^2 is constructed from these variables and the $M_{\ell\nu b}$, for which the "true value" is fixed at m_t.

Since improving further the S/B ratio by means of cuts would reduce too much the signal efficiency, multivariate methods are used.

9.3 Multivariate analysis

Enhanced b tagging First of all, an improved tagging of b-like jets is performed using a neural networks[1] (NN) which extends the simple detached vertex b-tagging by exploiting also the different decay multiplicity of B hadrons, their large mass, the B lifetime and the presence of soft leptons in many decay chains. A cut on the NN output could remove 60% of non b background while keeping a 82% efficiency for signal, but better results are obtained if the continuous NN output is used as an additional input for the multivariate analysis.

9.3.1 Likelihood based analysis

Likelihood functions are a standard way to combine multiple variables in one for better discerning power.

The procedure is rather simple[2]: let $x_v, v = 1 \dots n_v$ be the variables, s an index labelling the different sets ($s = 1$ is the signal, $s = 2..n_s$ the backgrounds).

1. Histograms $h_i^{s,v}$ are filled for each variable v, set s and bins $i = 1..b_v$.

2. These histograms are normalized so that $\sum_i h_i^{s,v} = 1$ for every set s, and variable v.

3. The probabilities $p_i^{s,v}$ are defined as $p_i^{s,v} = h_i^{s,v} / \sum_{s'} h_i^{s',v}$.

[1] Neural networks are classifiers composed by many simple interconnected nodes, often arranged in layers; input is fed through some nodes, and output is collected from other nodes; nodes are usually simple, i.e. they return a function of the weighted sum of their inputs. Then network can be "trained" on a sample where the correct classifications are known, and later used to classify similar data. Nodes usually return a simple function of the weighted sum of their inputs. More details and references can be found at `ftp://ftp.sas.com/pub/neural/FAQ.html`.

[2] Note that from a statistical point of view this procedure is not completely correct, as it does not take into account correlations between variables; anyway it is largely adopted, and produces satisfactory results

4. For each measurement $\{x_v\}$ one determines the bins i_v in which the of the $\{v\}$ variables fall, and the likelihood for a set s is computed as

$$\mathcal{L}_s(\{x_v\}) = \frac{\prod_v p_{i_v}^{s,v}}{\sum_{s'} \prod_v p_{i_v}^{s',v}}$$

For t channel analysis the variables used are:

- H_T: scalar sum of the p_T of the two jets, lepton and neutrino (E_T^{miss})
- M_{jj}: invariant mass of the two jets
- $M'_{l\nu b}$: a top mass reconstructed using the raw P_b and the $P_\nu(z)$ from the kinematic fit (using fitted values for all the momenta would just yield the fixed value $m(top)$ which is constrained in the fit)
- $Q \times \eta$: lepton charge times the untagged jet pseudorapidity
- $cos(\theta_{l,q})$: cosine of the angle between the lepton and the untagged jet, in the top quark rest frame
- $b - tag$: output of the NN b-tagger
- $\mathcal{M}_{t\ ch.}$: the matrix element for t channel single top (calculated with MadGraph), evaluated using the momenta from the kinematic fit

For s channel the choice is similar:

- H_T: scalar sum of the p_T of the two jets, lepton and neutrino (E_T^{miss})
- $p_T(j_1)$: leading jet p_T
- $cos(\theta_{\nu,\hat{z}})$: cosine of the angle between the neutrino momentum and the beam, in the top quark rest frame.
- $M''_{l\nu b}$: like $M'_{l\nu b}$, using a very simple NN to select the b quark to pair with the neutrino using the kinematic fit χ^2 and the difference in η between the two jets.
- $b - tag$: output of the NN b-tagger
- $\mathcal{M}_{s\ ch.}$: the matrix element for s channel single top, evaluated using the momenta from the kinematic fit

The likelihood for t channel separates the signal from all backgrounds rather well, while the one for s channel has a poor rejection against the "internal" t channel background.

The plots of the expected number of events classified using the likelihood compared with the observations are given in figure 9.1

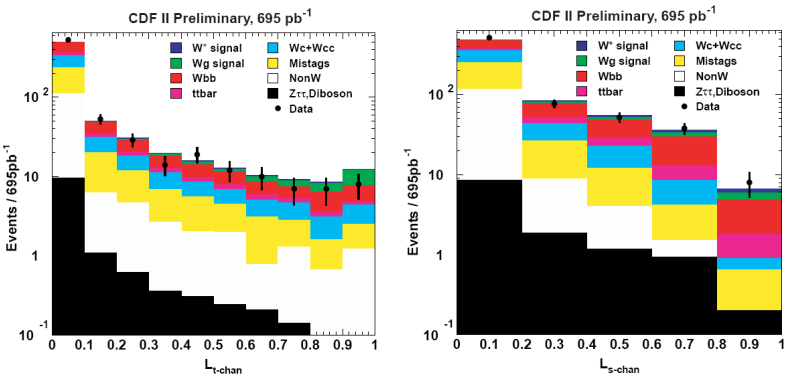

(a) t channel (b) s channel

Figure 9.1: CDF single top searches: likelihood based analysis; W^* and Wg are other names for s channel and t channel single top, respectively.

9.3.2 Neural Network approach

The other tool for multivariate analysis used in single top searches is a neural network with 14 inputs and one output: input variables include lepton and jet p_T, angular variables, invariant masses, the χ^2 from the kinematic fit, NN b tagging output; the one output channel is a number between -1 and $+1$, which should be maximum for signal and minimum for backgrounds.

Three different setups are used in which the signal is, respectively, all single top channels, only t channel and only s channel. In figure 9.2 is shown the expected number of events classified using the NN from the first setup, compared with the experimental signal observed.

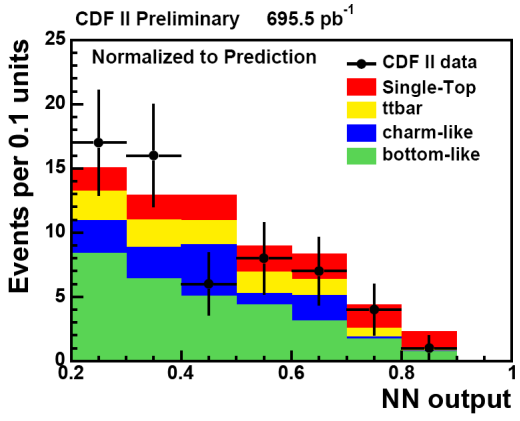

Figure 9.2: CDF single top searches: neural network based analysis, using both single top channels as signal

9.4 Conclusions

Systematics systematic uncertainties for both "theoretical" (ISR,FSR,PDF) and instrumental (jet energy scale, b tagging) have been estimated. Most effects are at the level of $1-3\%$, except jet energy scale which is $\sim 5\%$, and this gives a total uncertainty of $\sim 8\%$ on t channel cross section; s channel and combined analysis suffer from an additional very large systematic ($\sim 100\%$ and $\sim 30\%$) that comes from the modeling of non-W background.

Results Methods from bayesian statistics are used to determine the observed cross sections and the exclusion limits for different confidence levels (CL); a plot of this contour in the σ_t, σ_s plane is shown in 9.3 for the likelihood approach, while the 95% CL limits for both approaches are collected in table 9.4 . The CDF result is within one standard deviation from the SM predictions.

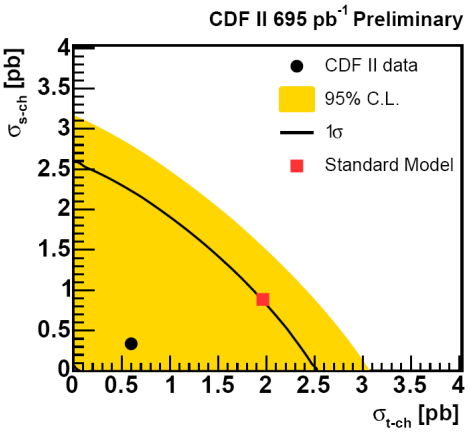

Figure 9.3: Preliminary results from CDF single top searches with $695\,\mathrm{fb}^{-1}$ (from likelihood analysis)

	t ch.	**s ch.**	**all**
Likelihood	2.9	5.1	4.3
Neural Network	3.1	3.2	3.4

Table 9.1: Upper limits to single top cross sections (95% CL) from CDF single top searches with $695\,\mathrm{fb}^{-1}$ (preliminary)

Chapter 10

Common tools for single top analysis

While the three single top channels have been considered almost independently, there are some features of the analysis which are almost uniform among the channels. A general description of these will be provided here.

10.1 The combined efficiency method

The selection efficiency for each physical process sample is usually estimated using a Monte Carlo sample as the ratio between generated and accepted events; in the case that no events are accepted a upper limit of $1/N_{gen}$ or $1.14/N_{gen}$ is given, which correspond to 63% and 60% CL for a Poissonian statistics. While this procedure is usually good, it fails for background processes with very high cross section and very low selection efficiencies, such as QCD multi jet production: in that case all events are rejected at the first selection stages, and the upper limit $1/N_{gen}$ is unacceptably large.

In order to estimate a more reasonable upper limit the combined efficiency has been developed using the assumption that for independent cuts the selection efficiencies factorize. The procedure is then simple: cuts are grouped in blocks so that the different blocks are almost independent, and efficiencies for each of these cut blocks are estimated in the traditional way as N_{acc}/N_{gen} as for every single cut the efficiency is large enough that $N_{acc} > 0$ or that $1/N_{gen}$ is an acceptable upper limit; finally, a "combined efficiency" is calculated as the product of these efficiencies. For example, the chance of finding a pair of opposite flavour isolated leptons in multi jet events can be estimated as the product of the probabilities of finding separately an isolated electron and a muon.
Further steps can be taken to improve this estimate. First of all, there are cuts that are obviously dependent on most of the others (fe.g. those on invariant masses); in this case, the efficiency for the cuts is estimated separately by assuming that the efficiency for this particular background is smaller than the one for some reference set (either the signal or some important background).

10.2 Evaluation of systematic uncertainties

10.2.1 Theoretical uncertainties

Integrated luminosity

While the statistical uncertainty on the luminosity is very small (1% after 100 ms of data taking), the total uncertainty on the integrated luminosity is expected to be $\pm 5\%$ at $10\,\mathrm{fb}^{-1}$ (10% at $1\,\mathrm{fb}^{-1}$, 3% at $30\,\mathrm{fb}^{-1}$).

In an ideal analysis where background is negligible, if N is the number of accepted events, ϵ the efficiency (from Monte Carlo), and L the integrated luminosity, then $\sigma = N/(\epsilon L)$ and the uncertainty is

$$\left(\frac{\Delta\sigma}{\sigma}\right)_L = \frac{1}{N/(\epsilon L)} \left|\frac{\partial}{\partial L}\left(\frac{N}{\epsilon L}\right)\right| \cdot \Delta L = \frac{\Delta L}{L}$$

If there are backgrounds so that $N = S + B$, and the way B is subtracted can influence the uncertainty on σ_S due to luminosity

Using known cross section The simplest way to subtract the background is by assuming the cross section for background (σ_B) known:

$$N = S + B = L(\epsilon_S \cdot \sigma_S + \epsilon_B \cdot \sigma_B)$$
$$\sigma_S = \frac{N}{\epsilon_S L} = \frac{N}{\epsilon_S L} - \sigma_B \frac{\epsilon_B}{\epsilon_S}$$

As the last term does not scale with luminosity, then

$$\left(\frac{\Delta\sigma}{\sigma}\right)_L = \frac{1}{\sigma_S} \left|\frac{\partial}{\partial L}\left(\frac{N}{\epsilon_S L}\right)\right| \cdot \Delta L = \frac{N}{L\epsilon_S\sigma}\frac{\Delta L}{L} =$$
$$= \frac{S+B}{S}\frac{\Delta L}{L} = \left(1 + \frac{B}{S}\right)\frac{\Delta L}{L}$$

This means that the uncertainty on the luminosity will bigger than 5%, and can become very large if $S/B \ll 1$

Using other data In order to improve the above result one can normalize the number of background events using data. One can select signal-like events in one region (1) and background-like ones in another region (2), so that

$$N_1 = S_1 + B_1 = L(\epsilon_{S,1} \cdot \sigma_S + \epsilon_{B,1} \cdot \sigma_B)$$
$$N_2 = S_2 + B_2 = L(\epsilon_{S,2} \cdot \sigma_S + \epsilon_{B,2} \cdot \sigma_B)$$

Now, if all the efficiencies are know from the Monte Carlo simulation, one can invert the above equations eliminating σ_B and solving for σ_S.

$$\sigma_S = \frac{N_1}{L\epsilon_{S,1}}\left(1 - \frac{N_2}{N_1}\frac{\epsilon_{B,1}}{\epsilon_{B,2}}\right)\left(1 + \frac{\epsilon_{S,2}\,\epsilon_{B,1}}{\epsilon_{S,1}\,\epsilon_{B,2}}\right)^{-1}$$

Now the factor $1/L$ multiplies all the expression, so that again

$$\left(\frac{\Delta\sigma}{\sigma}\right)_L = \frac{\Delta L}{L}$$

Background cross sections

The uncertainties on background cross sections have a behaviour similar to those from the knowledge of integrated luminosity.

If a background process X is subtracted using a fixed cross section, the relative uncertainty on the signal cross section is

$$\left(\frac{\delta\sigma}{\sigma}\right)_X = \frac{B_b}{S} \cdot \left(\frac{\delta\sigma_X}{\sigma_X}\right)$$

if B_X and S are the expected X background and signal yields; in case of poor S/B these uncertainties might become unmanageably large.

For background with large B/S, normalizing the background on the data, in the same way as described for the luminosity uncertainty, effectively removes the uncertainty from the background cross section, at least as long as the uncertainty is only on the overall normalization of the cross section and not on the differential distributions.

PDF uncertainties

Uncertainties on the parton density functions can affect the measured cross sections (i.e. if background and signal are affected differently) or the accuracy with which the measured and theoretically calculated cross sections can be compared in order to extract measurements of some parameter (i.e. $|V_{tb}|$ from single top cross section).

Modern PDF fits now give not only the best fit PDF, but also a set of other densities obtained by varying by $\pm 1\sigma$ each of the independent parameters; for CTEQ pdfs this amounts to 40 additional parton densities. In order to determine the effect of PDF uncertainties on a measurement, one could simulate events with each of these $40 + 1$ density, and compare the estimated "measured" values that would be obtained from the different sets; this task is often unmanageable, as very large samples would be required to have a negligible uncertainty from simulation statistics and to be able to correctly calculate the effect of PDFs.

A much less computationally expensive method uses the reweighting technique: a single sample of events is simulated with the best fit density, but for each event the $40 + 1$ weights from different PDFs are calculated. This allows to extract the $40 + 1$ different "measurements" from the same sample with different weights, and compute the effect of PDF uncertainties with much less uncertainty from the simulation statistics as now the samples have maximal correlation except for the densities.

Within CMS software framework the CMKIN program, the universal interface to generators like PYTHIA, Herwig or AlpGen, is able to perform the computation of all weights from all PDF sets compatible with Les Houches Accord standard such as CTEQ, MRST and others. The procedure is still somewhat lengthy, about 20 times slower than for normal physics simulation, because each density set must be evolved to the Q^2 of the event to compute the weight; in any case no additional time is required in the detector simulation and reconstruction steps, which are much longer than physics generation, especially when using full simulation.

Different methods have been proposed on how to evaluate the uncertainty on a measured parameter X, such as a cross section, when the 40 δX_i have been computed. A method which is statistically correct and does not overestimate uncertainties is as follows: for each of the $n = 20$ parameters, the δX_i^+ and δX_i^- shifts for a $\pm 1\sigma$ change in the parameter are combined to produce the positive and negative uncertainties on X through formula (10.1).

$$(\delta X^+)^2 = \sum_i (\max\{0,\, \delta X_i^+,\, \delta X_i^-\})^2 \qquad (10.1)$$
$$(\delta X^-)^2 = \sum_i (\max\{0,\, -\delta X_i^+,\, -\delta X_i^-\})^2$$

In this way, shifts from each independent parameter are added up in quadrature correctly, considering separately the positive and negative shifts, even in the case when δX_i^+ and δX_i^- have the same sign.

10.2.2 Experimental systematics

Jet energy scale

A very important source of systematic uncertainty is the calibration of jet energy scale; even if multiple calibration methods have been studied, as described in section 6.7.2, non negligible uncertainties on the scale are expected even after some years of LHC.

A simple way to estimate the effect of jet energy scale on any measured quantity without problems with simulation statistics is to use the same data sample first with no correction, as "simulated sample", and then with the jet energies rescaled by a given amount, as "data sample"; the shift of the fitted quantity on the "data sample" with respect to the true value is a measure of the effect of the jet energy scale on the quantity.

The procedure is repeated for a positive and a negative shift of the jet energy scale by an amount equal to the expected uncertainty on jet energy scale, and the largest shift is used as systematic uncertainty on the jet energy scale.

b-tagging efficiency

At an integrated luminosity of $10\,\mathrm{fb}^{-1}$ the expected knowledge on the b tagging efficiency is $\pm 4\%$ in the barrel and $\pm 5\%$ in the endcaps (both are relative uncertainties) for a large range of cut values on the b tagging discriminator, with some dependence on the b jet E_T below $\sim 80\,\mathrm{GeV}$, as shown in figure 6.20.

Different methods have been used to estimate the effect of this uncertainty on the single top cross section measurements.

The simplest method is to assume a flat $\pm 4\%$ uncertainty on the selection efficiency for signal and backgrounds, uncorrelated among the two. This estimate was used in the t and s channel analysis.

In di-leptonic tW channel analysis the cross section was fitted from a "data" sample in which 4% of the b tagged jets where insead assumed to be untagged, and then again by assuming 4% of the untagged jets to be b tagged instead, in both cases using the unmodified sample as "simulated" set. The two shifts where used to determine the uncertainty. This estimate is assumed to be conservative

for the mistag rate, on which no published uncertainty is available but that is surely below 4%.

In semi-leptonic tW analysis the shift in the fitted cross section obtained when the discriminator values of all the jets were shifted by an amount δ was used. δ was chosen to give relative shifts in the b-tagging efficiency for b jets equal to the expected systematic uncertainties. This method probably provides the best estimate for the b tagging efficiency systematic, but it might underestimate the uncertainty on the mistagging probability.

10.3 Computing significance

10.3.1 Definitions

Significance Significance is used to quantify the difference between a measurement and a theoretical prediction, or between two measurements; we will be concerted only on the first issue.

More precisely let the measured value be x_m and the expected value x_e. The significance s is defined through the equation

$$\mathcal{P}(\{|x - x_e e| > |x_m - x_e|\}) = 2\int_s^\infty \frac{1}{\sqrt{2\pi}} e^{-t^2/2} dt$$

where $\mathcal{P}(A)$ indicates the probability of measuring any value $x \in A$

One tailed significance can be built in a similar way: if $x_m > x_e$ then one can define s_+ through

$$\mathcal{P}(\{x > x_m\}) = \int_{s_+}^\infty \frac{1}{\sqrt{2\pi}} e^{-t^2/2} dt$$

Observation A common application of significance is with discoveries or confirmations of some new phenomena through a measurement, such as the discovery of a new particle. In this case the aim is to compare the actual measurement x_m and the expected value in a theory T_0 without that particle; one has to compute, usually with the help of Montecarlo techniques, the probability distribution of the x values if the T_0 is true, and use that distribution to calculate the significance.

Counting experiment Counting experiments are the simplest ones for calculating significance, as the measurement is simply the number N of observed signal-like events. If the theory without signal T_0 is true, all these events will be background events B; if $p_0(n)$ is the probability of counting n events when T_0 is true, the significance is defined as

$$\sum_{n=N}^{\infty} p_0(n) = \int_s^\infty \frac{1}{\sqrt{2\pi}} e^{-t^2/2}$$

If the uncertainties on the background are purely statistical, p_0 is a binomial or Poissonian probability. If there is some systematical uncertainty on the background usually one does not know the real shape of p_0; the standard approach

is to assume that the probability distribution is the convolution

$$p_0(n) = \int_{-\infty}^{\infty} p_p(n|\mu)\, N(\mu|B, \Delta B_{syst.}) d\mu$$

between a Poissonian distribution $p_p(n|\mu)$, with average μ, and a Gaussian distribution of μ with average B and standard deviation equal to the systematic uncertainty ΔB_{syst}

Future counting experiments As LHC has not started yet, this analysis is focused on determining the significance one can expect to find when data will be available; that is, the difference between what we expect to measure if the standard model is true and the prediction of a "standard model without single top".

If the standard model is at least approximatively true, one can estimate to observe a number N of signal-like events, S of which are real signal and B which are background; vice versa, without single top the prediction is $N_0 = B$.

Significance formulae Different estimators of significance exist; if we are interested in the significance of an observation of a signal, for which S events are expected over a background of B, and there is a systematic uncertainty ΔB on the background yield[1], the two basic ones are S_G and S_{cP}; the first is simply defined as

$$S_G = \frac{S}{\sqrt{B + \Delta B^2}} \tag{10.2}$$

while for the second an implicit formula is given

$$\sum_{n=S}^{\infty} \int_{-\infty}^{\infty} P(n|\mu)\, G(\mu|B, \Delta B)\, d\mu = \int_{S_{cP}}^{\infty} dx\, G(x|0, 1) \tag{10.3}$$

if $G(x|\mu, \sigma)$ and $P(n|\mu)$ are the Gaussian and Poisson probability densities.

If the expected yields are large, the two formulas give the same results as the Poisson density converges to a Gaussian by the central limit theorem.

Other estimators have been proposed, such as $S_{12} = 2(\sqrt{S+B} - \sqrt{B + \Delta B^2})$, with various different ways of taking into account systematic uncertainties; the results obtained with them are very similar, and so we will not discuss them here.

Deviations from Poisson statistics It should be noted that when the number of signal events is not obtained by straight counting the distribution of such a number no longer follows the Poisson statistics, and in particular it is no longer true that $\mu = \sigma^2$; this happens, for example, when the background events estimated by counting events in another region are subtracted from the number of signal-like events. If the numbers are still large, the Gaussian approximation is still good, and formula (10.2) can be used if the B at denominator is replaced by the variance of the expected background $\sigma^2(B)$, induced by the statistical uncertainties; for example in the dileptonic tW analysis $B \sim 1500$ but

[1] ΔB should be calculated in a scenario with no signal, but the difference is rarely important

the statistical uncertainty $\sigma(B)$ is 54 events instead of $\sqrt{1500} \simeq 39$ because the statistical fluctuations of the number of events in the background normalization region must be taken in account too.

Chapter 11

Single top, t channel

11.1 Overview

Among the three single top processes, t channel production has the largest cross section and the cleanest signature, so that it is likely to be observed first.

The final state after the $t \to Wb$ decay is Wbq; only the events with leptonic decays of the W are studied, as the others are too similar to ordinary QCD jet events which have extremely large cross sections and are therefore strongly suppressed by the trigger and suffer an overwhelming background.

The CMS analysis included in [PTDRv2]([CMS NOTE 2006/084]) is further restricted to muonic events, as muon identification and reconstruction is more accurate.

Monte Carlo samples for this analysis have been generated using SingleTop for single top events and a large range of matrix element generators (MadGraph, CompHEP, AlpGen, PYTHIA and TopReX) for background; parton showering and hadronization is always done with PYTHIA. NLO cross sections have been used for all single top channels and $t\bar{t}$, either directly or by rescaling the LO samples with constant K factors.

Full detector simulation and event reconstruction (OSCAR + ORCA) has been used for all the events.

A cut based selection is used to extract signal events from background; a genetic algorithm[1] software (GARCON) has been used to optimize cut values for a maximum S/B times statistical significance[2] at $10\,\mathrm{fb}^{-1}$. The expected yield is 2389 signal events and 1785 background events (mostly $t\bar{t}$ and $W + 2j$),

[1] A genetic algorithm is an optimization technique where a large, initially random, "population" of "individuals" (in this case, the cut parameters) is tested, and the better ones are allowed to "reproduce" by giving birth to other individuals with the possibility of "cross-breeding" (e.g. interchanging the value of a parameter with the partner individual) and casual "mutations" (e.g. perturbing a cut value by some random amount); the evolution procedure is iterated many times, with the result of producing (usually) better individuals. The algorithm is slow compared to straight minimization (e.g. steepest descent), but much more reliable, and performs well even for a large number of variables.

[2] Within the allowed optimization variables in GARCON, it is a reasonable compromise between optimizing statistical significance and systematical uncertainty (almost proportional to S/B)

for a total $S/B \simeq 1.34$ and a statistical significance $S/\sqrt{(S+B)} \simeq 37$.

Systematic uncertainties from three different sources have been considered: theoretical uncertainties (pdf, higher orders, t and b quark masses) that affect mostly the total production cross section, jet energy scale and b tagging efficiency, both of which affect the expected efficiencies of signal and background events; the total contribution from these systematics on both signal and background to the measurement of the cross section is 8.0%.

Adding together statistical (2.7%), systematical (8.0%) and luminosity (8.7%) uncertainties, a measurement of the t channel cross section within 12.1% appears to be attainable with $10\,\mathrm{fb}^{-1}$. A simple extrapolaton to $1\,\mathrm{fb}^{-1}$ shows that a 7.7σ observation of the signal will be attainable even in the initial LHC phase.

11.2 Event generation and reconstruction

11.2.1 Parton level generation

For single top events the SingleTop generator has been used, as it implements NLO cross section with the correct matching with parton showering, spin correlations, t and W widths and b quark mass; TopReX, which has similar features, has also been used as a cross check. Only events $W \to \mu\nu$ decays have been produced, and generator level cuts on muon ($p_T > 9\,\mathrm{GeV}$, $|\eta| < 2.4$) and jets ($p_T > 10\,\mathrm{GeV}$, $|\eta| < 5$, $\Delta R(j,j) > 0.5$) have been imposed in order to increase the efficiency; the effective cross section after the cuts is 180 pb.

Events with W and heavy or light jets have been generated using the best suited matrix element generators for each specific process; LO cross sections have been used, rescaled to the NLO ones through constant K factors, and with the correct partonic matrix element for the hard jets in Wjj. The W boson was forced to decay as $W \to \mu\nu$ ($Wb\bar{b}j$, Wjj) or leptonically $W \to \ell\nu$ ($W+j$), as contributions from the other decays are expected to be small; no other cuts have been applied at generator level.

For the $t\bar{t}$ sample, the dominant background, direct generation through PYTHIA has been adopted as it is better suited for the large production needed; the sample has been rescaled with a constant K factor to the NLO cross section.

Looking at parton level distributions one can check the two main features of this channel: the η distribution for the light quark jet (fig. 11.1(a)) is peaked at $|\eta| \sim 3$ and not at the center, and the additional b quark is produced with very low p_T ($\lesssim 15\,\mathrm{GeV}$, see fig. 11.1(b)) so that is almost always invisible.

11.2.2 Detector simulation and reconstruction

The GEANT4 based detector simulation (OSCAR) has been used for all samples, and the pileup corresponding to a luminosity $2 \cdot 10^{33}\,\mathrm{cm}^{-2}\mathrm{s}^{-1}$ has been superimposed to the events at digitization.

Events where fed through the standard CMS reconstruction (ORCA) stages (Hit $\to$ Digi $\to$ DST) using the reconstruction algorithms described in chapter

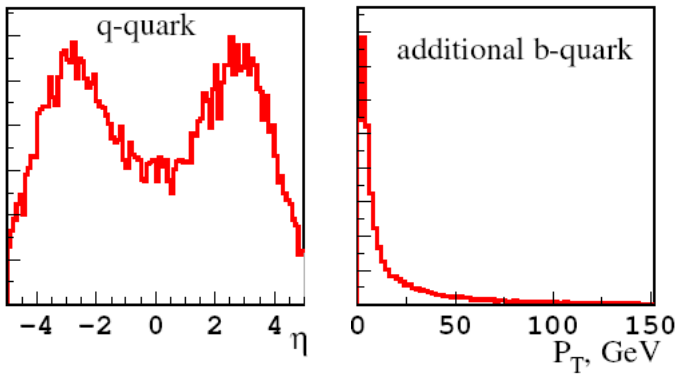

(a) Light quark pseudorapidity (b) Additional b quark p_T

Figure 11.1: Parton level distributions for single top t channel

6. Iterative cone algorithm ($R = 0.5$) has been chosen for jet reconstruction, using calibrations from Monte Carlo jets.

11.3 Event selection

11.3.1 Trigger and preselection

Events are required to pass the inclusive isolated muon trigger channel, that requires $p_T > 19\,\text{GeV}$ and $|\eta| < 2.1$.

Looking at the plots after full simulation and reconstruction (figure 11.2) one can check that the base kinematics found at parton level are preserved: the number of reconstructed jets is peaked at two for signal events, and there is a light quark[3] jet at high $|\eta|$.

After trigger, additional requirements are imposed: $E_T^{miss} > 40\,\text{GeV}$, and at least two jets with uncalibrated $p_T > 20\,\text{GeV}$.

11.3.2 Event selection

W boson reconstruction As there is only one neutrino, the W mass constraint allows for full kinematic reconstruction up to the twofold ambiguity on the longitudinal component of the neutrino momentum.

Due to experimental uncertainties, it might happen that the quadratic equation for $p_z(\nu)$ has no real solutions: in this case the m_W value in the equation is increased up to the minimal value required for a real solution to be found; in the opposite case, when equation has two real solutions, the one giving minimal $|p_z(\nu)|$ is selected.

Jet kinematic cuts Events are required to have exactly two jets with $p_T > 35\,\text{GeV}$; one must be within $|\eta| < 2.5$ and b tagged ($disc > 2.4$) while the second

[3]It should be noted that b tagging cannot be applied outside the tracker coverage, so that all forward jets are considered light

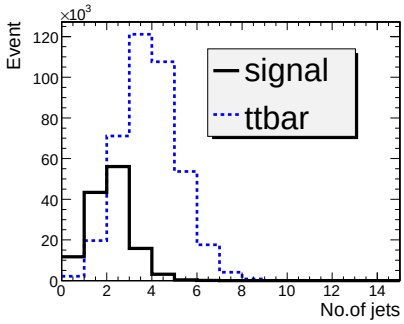

(a) Number of jets (uncalibrated $p_T > 20\,\text{GeV}$)

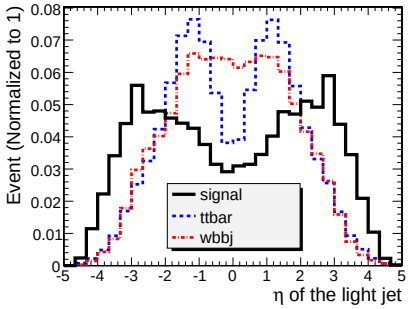

(b) Light jet pseudorapidity

Figure 11.2: Jet number and kinematics after full simulation and reconstruction (t channel)

must be forward ($|\eta| > 2.5$)

Top reconstruction The top quark can be reconstructed using the W and the b jet in the event: the top mass peak is cleanly visible (figure 11.3)

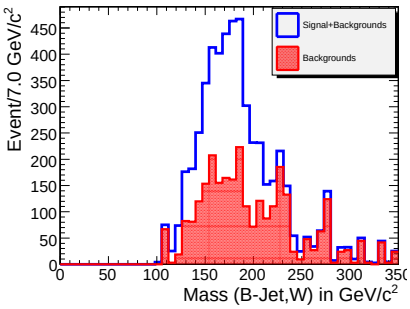

Figure 11.3: Reconstructed top quark mass (t channel)

Cut optimization Additional cut variables are used to increase the signal purity: the transverse mass of the W boson $m_T(W)$, the reconstructed top mas $m_{rec}(t)$ and the total reconstructed transverse momentum $\vec{\Sigma}_T$ defined as

$$\vec{\Sigma}_T = \vec{p}_T(\mu) + \vec{E}_T(b) + \vec{E}_T(j) + \vec{E}_T^{miss}\,.$$

This variable, zero at partonic level, gives the p_T amount of "extra objects" such as soft jets or leptons outside acceptance.

A genetic algorithm code (GARCON) has been used to optimize the cut bounds on these three variables and possible additional cuts on E_T^{miss}, $p_T(\mu)$,

jet E_T and the b tagging discriminator cut value. The cut windows obtained are

$$\begin{aligned} & |\vec{\Sigma}_T| && < 43.5\,\text{GeV} \\ 50\,\text{GeV} < & \ m_T(W) && < 120\,\text{GeV} \\ 110\,\text{GeV} < & \ m_{rec}(t) && < 210\,\text{GeV} \end{aligned}$$

Selection efficiency The selection efficiencies obtained by applying the cuts in sequence are summarized in table 11.1 for the signal and the dominant backgrounds. For an integrated luminosity of $10\,\text{fb}^{-1}$, 2389 signal and 1785 background events are expected, with a signal over background ratio $S/B \simeq 1.34$.

Table 11.1: Summary of effective cross sections at each selection stage; all values are in picobarns except the last row that contains the expected yield for $10\,\text{fb}^{-1}$

	signal	$\mathbf{t\bar{t}}$	$\mathbf{W}(\to \mu)\mathbf{b\bar{b}j}$	$\mathbf{W}(\to \ell)\mathbf{j}$	$\mathbf{W}(\to \mu)\mathbf{jj}$
$\sigma \times$ BR	180	833	32.4	9700	99
isolated muon	0.73	0.14	0.52	0.16	0.81
jets & E_T^{miss}	0.036	$6.4 \cdot 10^{-3}$	$3.4 \cdot 10^{-3}$	$9 \cdot 10^{-6}$	$3 \cdot 10^{-3}$
3^{rd} jet veto	0.021	$5.8 \cdot 10^{-4}$	$1.6 \cdot 10^{-3}$	$4 \cdot 10^{-6}$	$1.1 \cdot 10^{-3}$
$\lvert\Sigma_t\rvert$ cut	0.018	$4.1 \cdot 10^{-4}$	$1.2 \cdot 10^{-3}$	$4 \cdot 10^{-6}$	$6.8 \cdot 10^{-4}$
$m_t(w)$ window	0.015	$2.2 \cdot 10^{-4}$	$9.6 \cdot 10^{-4}$	$1 \cdot 10^{-6}$	$5.4 \cdot 10^{-4}$
$m_{rec}(t)$ window	0.013	$1.4 \cdot 10^{-4}$	$5.8 \cdot 10^{-4}$	0	$4.1 \cdot 10^{-4}$
Expected events	2389	1188	195	0	402

Multi-jet background QCD background have been estimated through the combined efficiency method introduced in section 10.1. Two cut groups have been used: the requirement of one hard isolated muon (ϵ_ℓ) and the requirement of two jets, one b-tagged and one forward, plus $E_T^{miss} > 40$ (ϵ_J); the expected number of multi-jet after this preselection is less than 8% of all the other backgrounds, so it has been considered neglegible in the analysys.

11.4 Systematics uncertainties

Theoretical uncertainties Theoretical uncertainties on the signal and background production have been considered, even if only through their effect on the total cross section.

A detailed calculation of the uncertainties on the signal cross section has been performed in [2], considering separately the effect of PDF, higher ordered in perturbation theory (through QCD scale dependence) and uncertainties on the top and bottom quark masses. The results are presented in table 11.2; the total uncertainty on the cross section is $-4\%/+3.6\%$.

For the backgrounds, theoretical calculations give 5% for $t\bar{t}$, 17% for $Wb\bar{b}j$, 7% for Wj and 5% for Wjj

Source	**Effect** $[\delta\sigma/\sigma]$
PDF	-2.2% / $+1.3\%$
QCD scale	$\pm 3\%$
top mass	$-1.46\%/+1.56\%$
b mass	$< 1\%$
combined	$\mathbf{-4}\%$ / $\mathbf{+3.6}\%$

Table 11.2: Theoretical uncertainties on t channel cross section

Jet energy scale The systematic uncertainty was estimated with the common procedure described in section 10.2.2.

b **tagging efficiency** The simplest method described in section 10.2.2 was used to estimate the uncertainty from b-tagging efficiency, assuming a $\pm 4\%$ uncertainty in the selection efficiencies for all the samples.

Integrated luminosity As described in [PTDRv1], chapter 8, the expected uncertainty on the knowledge of the integrated luminosity is conservatively assumed to be 5%; this affects all samples in a correlated way, and produces an uncertainty on the signal cross section given by

$$\frac{\Delta\sigma}{\sigma} = \frac{\Delta N}{S} = \frac{\Delta N}{N} \cdot \left(1 + \frac{B}{S}\right) \simeq 8.7\%$$

11.5 Conclusions

Adding up all the individual contributions, listed in table 11.3, the uncertainty on the cross section is

$$\frac{\mathbf{\Delta}\sigma}{\sigma} = \mathbf{2.7}\%\,(\text{stat}) \;\oplus\; \mathbf{8.0}\%\,(\text{syst}) \;\oplus\; \mathbf{8.7}\%\,(\text{lum}) \;=\; \mathbf{12.1}\%$$

In the above results the systematics on jet energy scale and b tagging are added add up incoherently on the samples; an over-conservative approach can be obtained by assuming full correlation among the samples, for which the overall systematical uncertainty is 10.7%, and the total one becomes 14.1%

Significance The significance obtainable for observing the signal can be calculated as the probability that all the signal is just a fluctuation of the background $\delta B = S$. As numbers are large we can work in the Gaussian approximation, for which the significance is $s_G = S/\Delta B$ where ΔB contains statistical, systematic and luminosity uncertainties on the background alone; the result at $10\,\text{fb}^{-1}$ is 15.9.

Table 11.3: Statistical and systematical uncertainties for t channel analysis, for $10\,\mathrm{fb}^{-1}$ integrated luminosity. In the last column, contributions to the cross section uncertainty from each source are provided.

	signal	**$t\bar{t}$**	**W$b\bar{b}$j**	**Wjj**	**$\Delta\sigma/\sigma$**
Yield	2389	1188	195	402	
Statistics	2.0%	2.9%	7.2%	4.9%	2.7%
Theory	4.0%	5.0%	17%	5.0%	5.0%
Jet energy scale	3.0%	6.1%	3.1%	$< 1\%$	4.3%
b **tagging**	4.0%	4.0%	4.0%	4.0%	4.5%
Luminosity	5.0%	5.0%	5.0%	5.0%	8.7%

Estimates for $1\,\mathrm{fb}^{-1}$ It can be interesting to extrapolate down the significance to an integrated luminosity of $1\,\mathrm{fb}^{-1}$ to see if it would be possible to claim a 5σ observation even there.

In addition to increasing the statistical uncertainty by a factor $\sqrt{10}$, also the systematics must be rescaled: the uncertainty on the knowledge of integrated luminosity doubles ($5\% \to 10\%$), the uncertainty on the jet energy scale too, while the b tagging systematic only increases by a factor 1.5 and the theoretical uncertainties don't change.

The estimated significance is then $s_G \sim 8.4$, but numbers are smaller so that the correct distribution, Poissonian convoluted with a Gaussian systematic, should be used, and the result would be $s_P \simeq 7.7$; even using the overconservative approach in summing systematics the significance is still large, $s_P \simeq 7.5$.

Chapter 12

Associate tW production

12.1 Overview

Associated tW production has a cross section of 0.14 pb at Tevatron, so that the integrated luminosity collectable in the next years will probably be insufficient for a significant discovery; at LHC the cross section is much larger, 60 pb, thanks to the increased gluon and b parton luminosities in the needed x range, so that observation of the signal should be possible.

The final state for tW after the $t \to Wb$ decay is WWb, similar to the one of $t\bar{t}$ production except for the single b jet; due to the much larger $t\bar{t}$ cross section ($\simeq \times 14$), the large contribution from such background events where the second b jet is outside the acceptance is the main issue for tW searches.

Due to the much better quality of lepton triggers with respect to thoese based on jet and b jet ones, only events with at least one $W \to \ell\nu$ have been considered. Specifically, the analysis has been done separately in the semi-leptonic decay channel ($tW \to \ell\nu bjj$) and di-leptonic one ($tW \to \mu e\nu\nu b$); only final state muons and electrons are used, even if also τ leptons are allowed at generator level, and in the di-leptonic channel only opposite flavour leptons are used to reduce the Zb background.

Monte Carlo events have been generated through TopReX, PYTHIA and AlpGen; for the semi-leptonic channel, a custom version of the fast FAMOS detector simulation has been used, while in the di-leptonic channel the main signal and background events were available from the official production of fully simulated events, and FAMOS was used for the production of minor background samples and systematic uncertainty evaluation.

Similar preselection requirements have been applied for the two decay channels, using lepton and jet quality cuts, and the same trigger streams have been used (inclusive isolated electron or muon). The further selection has some notable differences, as in the semi-leptonic case the full event kinematic can be reconstructed, and combinatorial issues of the $W \leftrightarrow b$ pairing and the choice of the solution for $p_z(\nu)$ must be faced, while for di-leptonic decays the two neutrinos do not allow for any reconstruction.

In both cases the S/B ratio after all selection cuts is poor: 0.37 for di-leptonic

decays, where the background is almost only dileptonic $t\bar{t}$; 0.19 for semi-leptonic, where non negligible contributions from W + jets and t-channel single top are expected. The expected signal yield for $10\,\mathrm{fb}^{-1}$ integrated luminosity is 560 and 1700 for di-leptonic and semi-leptonic decays.

Multi-jet QCD background has been examined with the combined efficiency method, and is found to be negligible for di-leptonic events and small for semi-leptonic ones.

Systematic uncertainties from most experimental sources have been computed: jet energy scale, b-tagging efficiency, pileup, integrated luminosity and Monte Carlo statistics; uncertainties from background cross section and pdf uncertainties were also included. Due to the bad S/B, background normalization using data is crucial to keep systematic uncertainties at an acceptable level.

Selection optimization has been done using genetic algorithms or simple cut scanning, in order to reduce the total uncertainty on the measured cross section. The estimates for the statistical and systematical uncertainties for $10\,\mathrm{fb}^{-1}$ integrated luminosity are $7.5\% \oplus 16.8\%$ for semi-leptonic and $8.8\% \oplus 23.9\%$ for di-leptonic.

Significance of the observation, against the null hypothesis of no tW production, can be computed separately for the two channels (4.2 for 2ℓ, 5.1 for 1ℓ), and the combined value is 6.4; even if the additional uncertainties from the currently available simulated statistics are over-conservatively added to the systematic uncertainty, the combined significance is still 5.1.

12.2 Event generation and reconstruction

12.2.1 Physics event simulation

Different physics generators have been used for matrix element generation of the various physical processes. TopReX was used for single top samples and for $t\bar{t}$ and $Wb\bar{b}$ background (1ℓ analysis), as it was specifically designed to address those processes. AlpGen was adopted for $W + n$ jets, as it includes the correct matrix elements for final states with n partons and the correct matching with PYTHIA parton shower. The general purpose and fast PYTHIA simulator was used for WW + jets, $t\bar{t}$ (2ℓ analysis), and QCD multi-jet.

Showering and hadronization have been simulated with PYTHIA for all processes.

Whenever NLO calculations of the cross sections were available but only LO generation was possible, samples have been rescaled with constant K factors to the NLO cross section.

In order to avoid double counting whenever simulated samples, where both di-leptonic and inclusive samples were used, generator level information was used to reject the inclusive events where both W bosons were undergoing leptonic decays; this allows to correctly add up the contributions without introducing additional statistical uncertainties that would show up if a simple subtraction of the dileptonic yield from the inclusive yield was used.

12.2.2 Detector simulation and reconstruction

Full GEANT detector simulation and event reconstruction through OSCAR+ORCA was used in the collaboration official Monte Carlo production. Simulated samples for $t\bar{t}$, di-leptonic tW and QCD jet production were available at the time, so they have been used in di-leptonic channel. The remaining backgrounds, which were deemed to yield minor contributions, were simply passed through fast simulation with FAMOS.

Semi-leptonic tW samples from full simulation, instead, were not available, so FAMOS had to be used; to avoid introducing some bias by comparing fast simulation signal with full simulation backgrounds[1], FAMOS has then been used also for all background samples.

A custom build version of FAMOS was used within the semi-leptonic group in order to include additional features not yet available in the standard release, notably the complete simulation of HLT triggers, the inclusion of calorimeter tower information into the output files, and the inclusion of weights for pdf uncertainties (described in 10.2.1).

A summary of all the simulated samples and the software used is presented in table 12.1.

Table 12.1: Simulated samples used for tW analysis; for matrix element generators A, P, and T mean AlpGen, PYTHIA and TopRex, while detector simulation O,F,F$'$ mean OSCAR+ORCA, standard and custom FAMOS.

Mode	**Semi-leptonic**	**Di-leptonic**
di-leptonic tW	180k TF$'$	80k TO
semi-leptonic tW	360k TF$'$	—
fully hadronic tW	180k TF$'$	—
di-leptonic $t\bar{t}$	360k TF$'$	900k PO
non di-leptonic $t\bar{t}$	—	1.54M PO
semi-leptonic $t\bar{t}$	740k TF$'$	—
fully hadronic $t\bar{t}$	180k TF$'$	—
leptonic t-channel single top	100k TF$'$	40k TF
hadronic t-channel single top	100k TF$'$	—
leptonic s-channel single top	100k TF$'$	—
hadronic s-channel single top	100k TF$'$	—
leptonic $Wb\bar{b}$	100k TF$'$	—
hadronic $Wb\bar{b}$	100k TF$'$	—
W + 2 jets	576k AF$'$	—
W + 3 jets	321k AF$'$	—
W + 4 jets	87k AF$'$	—
WW+jets di-leptonic	—	100k PF
WW+jets inclusive	—	100k PF
Multi-jet	1.4M PF$'$	2M PO

[1]Even if the fast simulation is rather accurate, efficiencies are slighly higher than for fully simulated events

12.3 Event selection

12.3.1 Trigger

In both decay channels the inclusive muon and inclusive electron trigger channels have been considered: jet and E_T^{miss} triggers have too high thresholds compared to the average p_T of the objects produced in this process, while di-lepton triggers are not interesting because only opposite flavour leptons are used.

Trigger efficiencies have been determined using both FAMOS and fully simulated events, and good agreement was found. The expected high level trigger efficiencies are 71.2% for the di-leptonic channel, and 47.7% for the semi-leptonic one.

12.3.2 Event preselection

Leptons

Electron Identification Cuts have been applied on the ratio between calorimeter supercluster energy and track momentum ($E/P \geq 0.8$), and on their inverse difference ($|1/E - 1/P| < 0.8\,\mathrm{GeV}^{-1}$), on the ratio between hadronic and electromagnetic energy deposits ($H/E < 0.05$), and on the angular matching between supercluster and track ($\Delta\eta < 0.005$, $\Delta R = \sqrt{\Delta\phi^2 + \Delta\eta^2} < 0.15$)

Photon conversion removal Electron candidates from photon conversions have been discarded by requiring no other electron tracks within $\Delta R < 0.01$

Electron isolation Full track based isolation has been applied, with cone radius $R_{iso} = 0.35$, veto radius $R_{veto} = 0.015$, vertex matching $\Delta z \leq 4\,\mathrm{mm}$, $\Delta r \leq 1\,\mathrm{mm}$; only tracks with at least four tracker hits, and $p_T > 0.9\,\mathrm{GeV}$ are used

Muons For muon candidates tracker isolation is required, but only in the di-leptonic channel.

Jets

The main rejection of $t\bar{t}$ background is given by the veto on the second b jet. Because of this, reconstructed jets which do not belong to the final state partons, such as those from pileup, radiation or even calorimetric noise faking a jet, must be identified in a reliable way; on average, about one "extra" jet is found in each event with a E_T comparable to that of the signal jets.

This problem was pointed out in other analysis where a jet veto was important for background rejection, such as $H \to WW \to 2\ell\,2\nu$.

In order to understand the features of these "extra" jets, single muon samples and semileptonic tW samples have been used: jets not associated to final state partons or leptons are characterized by few associated tracks and calorimeter towers, with a greater angular spread.

Semi-leptonic channel In the semi-leptonic channel, a Fisher discriminant is build from the combination of five variables: the number of associated tracks, number of associated towers, tower energy weighted ΔR, maximum tower energy and ratio between the calorimetric energy deposits within a cone of $\Delta R = 0.3$ and the total jet energy. This allows classify the jets into three categories, with different efficiencies for signal (real jets) and background (extra jets): good jets ($\epsilon_S = 84.3\%$, $\epsilon_B = 13.1\%$), loose jets ($\epsilon_S = 13.4\%$, $\epsilon_B = 22.7\%$) and bad jets ($\epsilon_S = 2.3\%$, $\epsilon_B = 64.2\%$). Bad jets where completely removed from the list of reconstructed jets, while loose jets are not accepted for signal jets but are counted for the jet veto purpose.

A plot of the five variables and of the fisher discriminant distributions for jets associated to a signal and extra jets can be found in figure 12.1; the distribution of number of jets for different quality requirements is plotted in figure 12.2

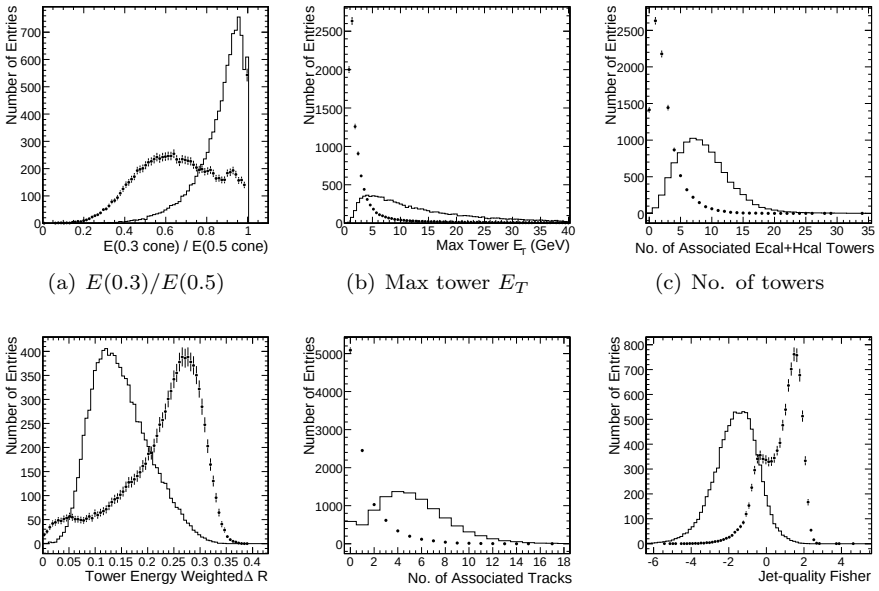

(a) $E(0.3)/E(0.5)$ (b) Max tower E_T (c) No. of towers

(d) Weighted ΔR (e) No. of tracks (f) Fisher discr.

Figure 12.1: (a-e) discriminating variables used to detect extra jets; (f) Fisher discriminant built from these variables. In all plots, the continuous histogram is the distribution for jets matched to quarks or leptons from the tW process, and the points are from extra jets.

Di-leptonic channel In the di-leptonic analysis a simpler cut was deemed to be sufficient: jets were accepted if three or more tracks with $p_T > 1\,\text{GeV}$ and at least five tracker hits where found, otherwise they where dropped from the list of reconstructed jets; such cut provides a 86.2% efficiency for real jets and a 71.8 rejection of extra jets.

In order to reduce the contamination from those $t\bar{t}$ events where a good jet is mistagged and discarded, eventually allowing the event to pass the jet veto,

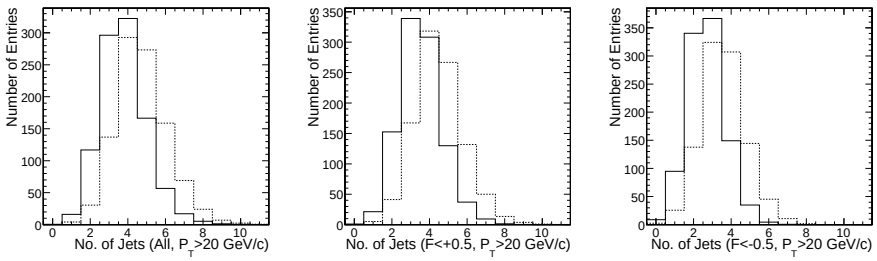

(a) All jets (b) Without bad jets (c) Only good jets

Figure 12.2: Number of jets in semileptonic tW events (solid) and $t\bar{t}$ events (dashed), for different cuts on the jet quality Fisher discriminant.

events where two jets are discarded as bad are rejected: there is almost always one extra jet in $t\bar{t}$ background events, and so if two jets are discarded this usually means that a good jet has been mistagged as bad.

12.3.3 Event selection: di-leptonic channel

Charged leptons The charged leptons are required to be of opposite charge with different flavours (one electron and one muon) in order to suppress the $Z \to \ell^+\ell^-$ and Drell-Yan backgrounds. A p_T cut at 20 GeV on both charged leptons reduces the backgrounds where one of the leptons comes from the decay of a b quark. Leptons not coming from W decays have a p_T distribution that peaks below 10 GeV, as shown in figure 12.3; instead, p_T distributions for the three samples tW, $t\bar{t}$ and WW are almost exactly equal if dileptonic final decays are considered.

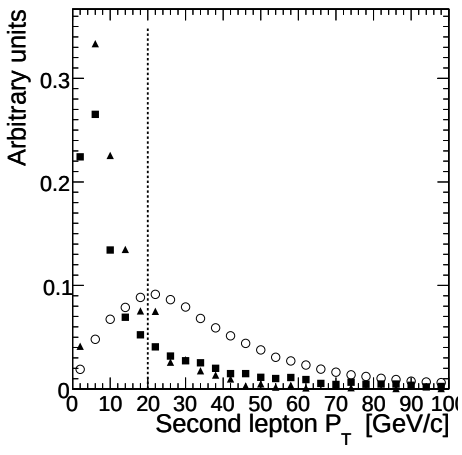

Figure 12.3: The p_T distribution of the second lepton for di-leptonic $t\bar{t}$ (empty circles), non di-leptonic $t\bar{t}$ (squares) and leptonic t channel single top (triangles).

This cut also avoids the region in which the p_T spectra produced by FAMOS

and ORCA differ considerably.

Jets The combined secondary vertex b-tagging algorithm has been used, and jets are tagged as b if the discriminating function is > 0 (efficiency $\simeq 60\%$). The events can be well classified by the number of b jets found and the p_T of the second jet (see figure 12.4). WW background is very important for single jet events with no b tagging, but is otherwise almost completely negligible; $t\bar{t}$ background is present everywhere, and is dominating over any other sample for high jet 2 p_T in all the two b events. Events are selected as signal if they have exactly one jet, b tagged.

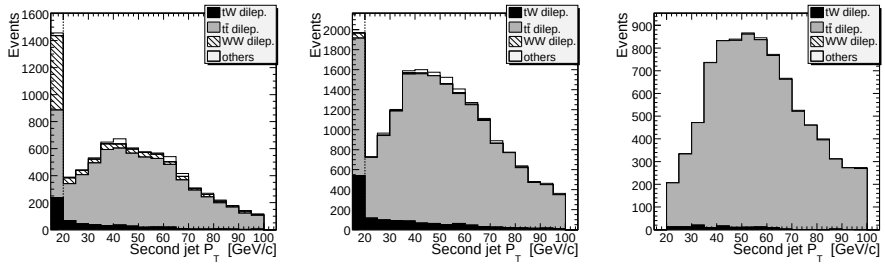

(a) No b jets (b) One b jet (c) Two b jets

Figure 12.4: p_T of the second jet for events with 0, 1 and 2 b-tagged jets; the vertical axis is numbers of events expected for 10 fb^{-1}; Leptonic t channel single top, non di-leptonic $t\bar{t}$ and WW are grouped together under "other". The first column in the zero and one b plots are single jet events.

Missing energy $E_T^{miss} > 20\,\text{GeV}$ is required to provide better rejection against low $\hat{p_T}$ multi-jet background.

Isolation All the reconstructed objects are required to be isolated ($\Delta R > 0.5$) in order to suppress background caused by non primary leptons or hadrons misidentified as leptons.

The kinematic cuts are summarized in table. The b-disc in the table is the b tagging discriminator.

Table 12.2: Kinematic cuts used in the di-leptonic channel.

Leptons
$\lvert\eta(e)\rvert < 2.4$, $\lvert\eta(\mu)\rvert < 2.1$
$p_{T_1} > 20$ GeV, $p_{T_2} > 20$ GeV
no other lepton with $p_T > 5$ GeV
Jets
One jet: $\lvert\eta\rvert < 2.4, p_T > 60$ GeV, b-disc > 0
No other jets with $p_T > 20$ GeV
Missing E_T: $E_T^{miss} > 20$ GeV

12.3.4 Event selection: semi-leptonic channel

Leptons One electron ($|\eta| < 2.4$, $p_T > 30\,\text{GeV}$) or one muon ($|\eta| < 2.1$, $p_T > 20\,\text{GeV}$) is required, and no additional leptons with $p_T > 10\,\text{GeV}$ are allowed. Different thresholds are used for electron and muons because the trigger thresholds are also different between the two flavours.

Jets Combined secondary vertex algorithm has been used with a threshold of 2 ($\simeq 50\%$ signal efficiency) for defining b jets; light quark jets are instead required to have a negative discriminating value ($disc = 0$ corresponds to $\simeq 60\%$ efficiency). No jets in the intermediate region are allowed.

Two light quark jets and and one b jet are required, all with $p_T > 35\,\text{GeV}$ and $|\eta| < 3$, and classified as good jets using the fisher discriminator defined in 12.3.2. No other jets with $p_T > 20\,\text{GeV}$, $|\eta| < 3$ are allowed in the event, unless classified as bad jets and removed during preselection; if a fourth jet is found but with $p_T < 20$ or $|\eta| > 3$, and the invariant mass of this jet and any one of the other light jets is within 20 GeV from the W mass, the event is also rejected, to reduce the efficiency of $t\bar{t}$ background events with one soft or very forward jet where one of the two b-jets is mistagged as light jet.

Missing energy $E_T^{miss} > 40\,\text{GeV}$ is required to provide better rejection against multi-jet background, for which E_T^{miss} is peaked around 20 GeV.

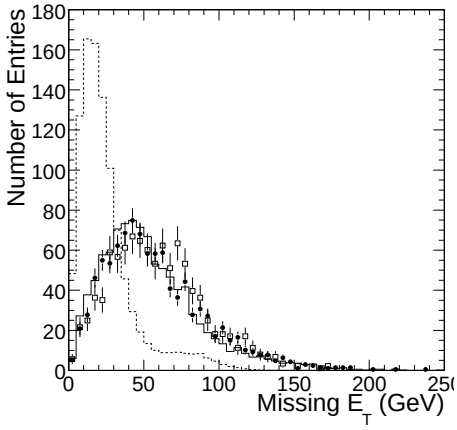

Figure 12.5: Missing transverse energy in semileptonic tW (solid histogram), QCD jets (dashed histogram), semi-leptonic $t\bar{t}$ (black dots) and dileptonic $t\bar{t}$ (white squares).

Isolation The three jets and the leptons are required to be isolated in (η, ϕ) space by $\Delta R > 0.5$.

W boson reconstruction The hadronically decaying W boson can be easily reconstructed from the two jets, and a $m(jj) < 115\,\text{GeV}$ is applied; the distribution of the invariant mass $m(jj)$ is plotted in figure 12.6(b).

In order to reconstruct the $W \to \ell\,\nu$ one must assume $\vec{p}_T(\nu) = \vec{E}_T^{miss}$ and obtain $p_z(\nu)$ from the mass constraint. In case the quadratic equation has two solutions, the one with lowest $|p_z(\nu)|$ is used (67% of the times it is correct); vice versa, if the two solutions are complex and conjugate, that happens in 37% of the events, the real part of $p_z(\nu)$ is used. A cut on the transverse mass of the leptonic W is also applied, $m_T(\ell + E_T^{miss}) < 120$. A plot of $M_T(W)$ can be found in 12.6(a).

$W \leftrightarrow b$ **pairing** In order to choose which W boson must be paired to the b jet, three variables have been considered for each W: the p_T of the $W + b$ system, the angular distance $\Delta R(b, W)$ and the product of the charges $q(b) \cdot q(W)$. The charge of the leptonic W is inherited from the lepton, while for the jets a charge is defined as the weighted sum of the charges of the tracks within the jet cone, with weights proportional to $\vec{p}_{trk} \cdot \vec{p}_{jet}$, and the hadronic W charge is given by the sum of the charges of the two light jets.

A Fisher discriminant with all these six variables was used to choose the correct pairing, yielding the successful choice in 72% of the events.

The distribution of the reconstructed top mass is plotted in figure 12.6(c).

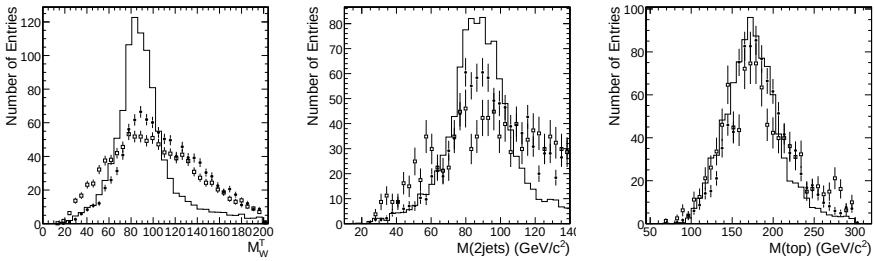

(a) $M_T(W \to \ell\nu)$ (b) $M(W \to jj)$ (c) $M(top)$

Figure 12.6: (a) transverse mass of the W decaying to $\ell\nu$; (b) mass of the W decaying hadronically; (c) mass of the reconstructed top quark. The distributions are plotted for semileptonic tW (solid histogram), semi-leptonic $t\bar{t}$ (black dots) and dileptonic $t\bar{t}$ (white squares).

Signal region Some global cuts are applied at the end of the reconstruction process, to improve the signal purity:

- Reconstructed top p_T within $20\,\text{GeV} < p_T(t) < 200\,\text{GeV}$
- Reconstructed top mass within $110\,\text{GeV} < m(t) < 230\,\text{GeV}$
- Scalar sum of the transverse energies $H_T < 850\,\text{GeV}$
- Reconstructed $p_T(t + W) < 60\,\text{GeV}$

12.3.5 QCD jet background

Background from QCD jets have been estimated using the combined efficiency method described in section 10.1.

Semi-leptonic In the semi-leptonic channel, the blocks where built by grouping the normal selection cuts into four blocks: jet selection (including veto), lepton selection, kinematic cuts on the reconstructed W bosons, and final selection (cuts on the reconstructed top, and b tagging requirements).

The amount of background expected from this estimate is not so small: 508 events for $10\,\text{fb}^{-1}$, 30% of the expected signal yield; anyway this number is expected to be largely conservative, as an anticorrelation was found between the cuts used to select leptons and those used to select jets.

Di-leptonic In the di-leptonic analysis cuts slightly different from those used in the normal selection where used, in order to reduce the correlations; four cuts are used: inclusive single e, inclusive single μ (both including p_T, η and isolation requirements), $E_T^{miss} > 20\,\text{GeV}$ and an exclusive cut on the jets (one or two jets, all b tagged).

By allowing for the second jet, the amount of QCD jet background expected for both signal and background control selections where estimated.

Eventually, the yields were computed by determining the combined efficiency also for the signal, and assuming the ratio between real efficiencies for signal and QCD jet background to be equal to the one between their combined efficiencies. Only a negligible amount of background from this source is expected: 5.6 events for the signal selection, and ≤ 10 for the background control selection.

The loose E_T^{miss} cut was found to provide rejection only for low $\hat{p}_T$ events. The background estimation procedure was repeated also without this cut, and the resulting background yield is still negigible ($B_{QCD}/S \lesssim 3\%$).

12.3.6 Efficiencies and expected yields

The efficiency results are converted in effective cross sections by multiplying them by the production cross sections of each process.. The effective cross sections, as well as the expected yields with $10\,\text{fb}^{-1}$ of data for all signal and background samples considered, are shown in table 12.3 and table 12.4 for di-leptonic and semi-leptonic channels, respectively. The signal to background ratio for $10\,\text{fb}^{-1}$ of integrated luminosity is found to be $562/1532 = 0.37$ for the di-leptonic channel and $1699/9256 = 0.18$ for the semi-leptonic channel.

12.4 Systematic uncertainties

12.4.1 Background normalization

In both analyses of tW cross section, a large number of $t\bar{t}$ background events pass all selection cuts. This requires to normalize background using data, by selecting separately signal-like and $t\bar{t}$-like events, as otherwise the uncertainties on the $t\bar{t}$ cross section or on the integrated luminosity will produce unmanageably large uncertainties on the measured tW cross section.

Table 12.3: Summary of effective cross sections at each stage of the analysis for the di-leptonic channel. All values are in picobarns except that the last row is the expected number of events for $10\,\text{fb}^{-1}$.

	tW	**$t\bar{t}$**		**WW**		**t ch.**	**QCD**
	(2ℓ)	(2ℓ)	(other)	(2ℓ)	(other)	(1ℓ)	**jets**
Production	6.7	92	740	11.1	89	82	$2.3 \cdot 10^9$
HLT	4.9	74	327	7.7	27	41.4	$1.5 \cdot 10^6$
2 ℓ	1.9	25	5.1	2.6	0.23	2.3	$2.1 \cdot 10^3$
Lepton p_T, η	0.68	7.9	0.118	0.54	0.012	0.098	0.002
≤ 1 extra jet	0.46	6.6	0.105	0.42	0.010	0.067	0.002
Jet p_T, η	0.30	5.2	0.096	0.33	0.004	0.033	0.0
≥ 1 bq-jet	0.21	4.2	0.068	0.019	0.0	0.022	0.0
$E_T^{miss} > 20$	0.19	4.0	0.064	0.019	0.0	0.020	0.0
≤ 2 jet	0.16	2.9	0.032	0.016	0.0	0.012	0.0
Final select.	0.056	0.14	0.0	0.006	0.0	0.0	0.0
Events [$10\,\text{fb}^{-1}$]	562	1433	4.3*	55	10*	20*	10†

* Upper limit at 68% CL estimated as $1.14/N_{gen}$.
† Estimated with the combined efficiency method.

If the control samples are chosen so that they are affected by systematic uncertainties of experimental origin (b tagging, jet energy scale) in the same way as the signal sample, uncertainties from these sources can also be reduced.

Semi-leptonic In the semi-leptonic analysis, the selection of the background control sample was done by requiring an additional hard jet in the event, without requirements on the b-tagging discriminator value assigned to the jet. The p_T requirements for the jets where also lowered: the b jet and the additional jet are required to have $p_T > 30\,\text{GeV}$, while light jets are accepted down to 20 GeV, which is the threshold used also for the jet veto.

Di-leptonic In di-leptonic analysis the requirements are the same as those used for signal selection except that one additional jet is required, $20\,\text{GeV} < p_T < 80\,\text{GeV}$, $|\eta| < 2.5$, and b tagged ($disc > 0$).

12.4.2 Theoretical systematics

Background cross sections A 9% uncertainty on the $t\bar{t}$ cross section was assumed, but this background is normalized on data and so the contribution to the uncertainty on the tW cross section is negligible.

The uncertainty on the $W+jets$ and $WW+jets$ cross sections contribute to the uncertainty on the cross section respectively by 3.1% (semi-leptonic analysis only) and 1% (di-leptonic analysis only). In the semi-leptonic analysis, an additional 0.8% uncertainty from the t channel single top is expected.

Parton density functions The reweighting technique described in section 10.2.1 was used to estimate the uncertainties form this source; the computed

Table 12.4: Summary of cross section times branching ratio times efficiencies at each stage of the analysis for the semi-leptonic channel. All values are in picobarns except that the last row is the expected number of events for $10\,\text{fb}^{-1}$.

	tW	**$t\bar{t}$**	**t ch.**	**W$b\bar{b}$**	**W2j**	**W3j**	**W4j**	**QCD**
Production	60	833	245	300	7500	2166	522	$9.7 \cdot 10^9$
HLT	18.9	263.9	39.5	34.0	1006	300	73	$1.9 \cdot 10^5$
Preselection and isolation	9.05	179.4	12.0	2.15	52	35	12	1325
Jet & lepton p_T; jet veto	1.28	18.5	1.31	0.061	0.60	4.9	1.0	4.23
b-tagging	0.669	6.13	0.476	0.016	0.10	0.99	0.26	0.85
kinem. cuts	0.223	0.987	0.047	0.003	0.017	0.101	0.008	0.105†
Signal region	0.170	0.762	0.035	0.001	0.013	0.054	0.008	0.051†
Events $[10\,\text{fb}^{-1}]$	1699	7624	351	10	130	539	80	508†

† Estimated with the combined efficiency method.

uncertainty is $-4.4\%/+6.0\%$ in the di-leptonic channel and $\pm 1.6\%$ in the semi-leptonic channel.

12.4.3 Experimental uncertainties

Jet energy scale The uncertainty on the jet energy scale is the dominant source of uncertainty in the di-leptonic channel, accounting for a $\delta\sigma/\sigma = 19.7\%$, and is very important also in the semi-leptonic channel ($\delta\sigma/\sigma = 9.4\%$). The somewhat conterintuitive fact that the uncertainty in the di-leptonic channel is larger can be explained with the fact that in this channel the signal is separated from the dominant $t\bar{t}$ background by the presence of a single jet instead of two, so that a miscalibraton of the jet energies will mostly result in signal-like events be considered $t\bar{t}$-like or vice versa; in the semi-leptonic analysis the requirement of additional jets partially offsets this effect as in this case a miscalibration results mostly in an increase or decrease of the efficiency for signal and background events, which introduces a smaller uncertainty thanks to background normalization.

b tagging efficiency Different methods have been used to estimate b tagging efficiency, all described in section 10.2.2. The uncertainty in the di-leptonic channel is larger than the one in the semi-leptonic one (8.7% vs 3.6%); attempts where made to reduce this uncertainty by not requiring the second jet in background control samples to be b tagged, or even using the weighted sum of the background control samples with one and two b-jets with weights of 1 and 2 respectively[2], but it resulted in an even larger uncertainty from the jet energy scale, so they were abandoned.

[2] In this way, the efficiency for both signal and background events has a linear dependence on the b tagging efficiency.

Pile-up Both analysis are very sensitive to the amount of pileup, for two reasons: the very strict threshold used for jet veto (20 GeV) and the jet cleaning algorithms used, which are based on calorimeter information or tracks without requiring vertex association. A sample of events was generated using the same physics events (that is, the same samples of generated particles) applying fast detector simulation and reconstruction through FAMOS with different amounts of pileup: zero, one and two times the expected amount for low luminosity runs; by fitting the cross section on the samples with different pileup using as "simulation" a sample with the standard amount of pileup, a significant variation was found: +20.4%/−16.2% for di-leptonic and +35%/−63% for semi-leptonic channels with zero/double pileup amount, with respect to the 4% variation from statistical origin observed when the FAMOS simluation was applied two times on the same physics sample with the same amount of pileup. As the instantaneous luminosity is expected to be known an uncertainty surely smaller than ±100%, the uncertainty quoted on the tW cross section is smaller, 30% of the difference between no pileup and normal pileup, as it was done also in the $t\bar{t}$ analyses within the CMS collaboration[PTDRv2].

Integrated luminosity The expected uncertainty on the integrated luminosity is 5%; in the di-leptonic channel the background is almost only $t\bar{t}$, that is normalized using data, and so the the uncertainty on the cross section from the knowledge of integrated luminosity is only 5.4%, while in the semi-leptonic channel also other backgrounds are non negligible so that the uncertainty increases to 7.8%.

Table 12.5: Summary of uncertainties on tW cross section measurement for $10\,\mathrm{fb}^{-1}$ of integrated luminosity.

	$\Delta\sigma/\sigma$	
	di-leptonic	**semi-leptonic**
Statistics	**8.8**%	**7.5**%
$\sigma(t\bar{t})$	—	—
$\sigma(W + jets)$	n/a	3.1%
$\sigma(WW + jets)$	1%	n/a
$\sigma(t$ ch.)	—	0.8%
PDF	−6.0%/+4.4%	1.6%
Jet energy scale	19.7%	9.4%
b tagging	8.7%	3.6%
Pileup	6.1%	10.3%
All syst.	**23.9**%	**16.8**%
Luminosity	5.4%	7.8%
Simulated statistics	9.9%	15.2%

12.5 Conclusions

The overall uncertainty expected on the cross section for tW associated production is

$$\frac{\boldsymbol{\Delta}\sigma}{\sigma} = \mathbf{7.5}\%\,(\text{stat.}) \;\oplus\; \mathbf{14.9}\%\,(\text{syst.}) \;\oplus\; \mathbf{7.8}\%\,(\text{lum.}) = \mathbf{18.4}\% \quad (1\ell)$$

$$\frac{\boldsymbol{\Delta}\sigma}{\sigma} = \mathbf{8.8}\%\,(\text{stat.}) \;\oplus\; \mathbf{23.3}\%\,(\text{syst.}) \;\oplus\; \mathbf{5.4}\%\,(\text{lum.}) = \mathbf{25.5}\% \quad (2\ell)$$

Significance The significance of the possible observation of the tW signal was calculated using the common procedures introduced in section 10.3; the Gaussian and Poissonian estimators give approximatively the same result, 5.1 in the semi-leptonic channel and 4.2 in the di-leptonic one.

Combining the two channels a significance of 6.4 is reached.

Chapter 13

Single top, s channel

13.1 Overview

The s-channel single top production, $q\bar{q}' \to W^* \to t\bar{b}$, is very interesting from the theoretical point of view because the theoretical uncertainties on the cross section are smaller than in the other channels, as it involves only light quark PDFs which are well known, and the uncertainty may in principle be further reduced by normalizing the process on the abundant and well known $q\bar{q}' \to W \to \mu\nu$ process. This could allow for a precise extraction of $|V_{tb}|$ from the measured cross section.

Moreover, the process is sensitive to interesting BSM scenarios such as additional heavy W bosons or the presence of a charged Higgs boson $H^{\pm}$.

The cross section at LHC is very small (10 pb), so that it is extremely difficult to resolve the signal against the backgrounds like $t\bar{t}$, t-channel single top and $Wb\bar{b}$.

The analysis published in [PTDRv2] used event samples generated with TopRex, PYTHIA and AlpGen, using FAMOS for detector simulation as there has been no official production of fully simulated events for that channel. The backgrounds considered were $t\bar{t}$, t-channel single top, $Wb\bar{b}$, tW, $w + 2jets$ and $Z/\gamma^* b\bar{b}$.

Inclusive single lepton ($1e$, 1μ) and combined $e \times jet$ trigger channels were used, and events with the final state $\ell E_T^{miss} bb$, and no other jets, where selected. In order to improve purity, additional cuts where imposed on the reconstructed $m_T(W)$, $m(top)$ and on the scalar and vector sums of the transverse momenta of all reconstructed objects, with thresholds optimized using genetic algorithms. The expected signal yield at $10\,\mathrm{fb}^{-1}$ is 274 events, with large backgrounds from $t\bar{t}$ (1260 events) and t-channel single top (630 events), and a signal over noise ratio of 0.13.

Systematics from theoretical sources (pdf, background cross sections, ...) and experimental sources (jet energy scale, b tagging efficiency) were considered; the dominant contribution is the effect of jet energy scale uncertainty on the expected efficiency of $t\bar{t}$ background, which gives $\delta\sigma/\sigma \sim 27\%$. The expected total uncertainties on the cross section are $\pm 18\%$ (stat) and $\pm 31\%$ (syst), but improvements are likely to be possible: in particular, a significant reduction of

the uncertainties form jet energy scale is foreseen from the use of energy flow techniques and $Z + jet$ calibration, which will be available for higher integrated luminosities.

13.2 Event generation and reconstruction

Generation Single top processes where simulated with TopReX, which includes full NLO computations for t channel, finite top and W widths and spin correlations.

The $Z/\gamma^* b\bar{b}$ sample was simulated only in the muon decay channel: the expected yield from the di-muon sample was doubled, assuming similar selection efficiencies for e and μ (which is true for the other processes), and the contribution was still negligible with respect to the other backgrounds.

The dominant $t\bar{t}$ background was generated with PYTHIA, later rescaling the sample to the NLO cross section; no decay modes where forced at generator level as both semi-leptonic and di-leptonic decays were expected to contribute significantly.

AlpGen was used for the $W + 2j$ sample; as the selection requires two b-tagged jets, this background was found to be negligible, and the other $W + nj$ processes are expected to contribute even less. Both jets are preselected at generator level requiring $p_T > 20\,\text{GeV}$, $|\eta| < 5$.

For all processes PYTHIA has been used for including radiative corrections for showering, and performing the necessary hadronization step.

The simulated samples for this analysis are summarized in table 13.1.

Detector simulation The fast FAMOS simulation of the detector response was used for all the samples, to achieve uniformity between the different processes, as no full simulation samples where publicly available for important processes, including the signal itself.

Table 13.1: Simulated samples used in s channel single top analysis; unless otherwise stated, all W bosons are required to decay leptonically ($\ell = \mu, e, \tau$).

Process	$\sigma \times BR$ [pb]	generator	size
s-channel	3.3 (NLO)	TopReX	233k
t-channel	81.7 (NLO)	TopReX	690k
$t\bar{t}$ (inclusive)	833 (NLO)	PYTHIA	2.76M
$tW(2\ell)$	6.7 (NLO)	TopReX	100k
$tW(1\ell)$	33.3 (NLO)	TopReX	157k
Wbb	100 (LO)	TopReX	549k
$W + 2j$	2500 (LO)	AlpGen	461k
$Z/\gamma^*\, bb$ ($\mu^+\mu^-$)	116 (LO)	CompHEP	59k

13.3 Event selection

13.3.1 Trigger

Only the inclusive (single) lepton triggers and the $e \times j$ HLT trigger channels[1] are suitable to select signal events;

The efficiency of the single muon stream is $24-25\%$ for s and t channel single top and $Zb\bar{b}$ ($Z \to \mu\mu$), and slightly lower for inclusive $t\bar{t}$ (21%) and $Wb\bar{b}$ (17%); a similar efficiency is found for the electron, again except for $t\bar{t}$ (36%) and $Wb\bar{b}$ (14%). The proposed $e \times j$ channel has 7% efficiency for t and s channel single top, 16% efficiency for $t\bar{t}$ and below 1% for $Wb\bar{b}$.

13.3.2 Preselection

In addition to high level trigger requirements, further cuts are applied at this step.

Leptons Only one lepton with $p_T > 10\,\text{GeV}$ is allowed in the event, and it must have $p_T > 19\,\text{GeV}$. Pseudorapidity cuts are applied to keep only events within the fiducial region for muon chambers and ECAL: $|\eta| < 2.1$ for muons, $|\eta| < 2.4$ for electrons.

Tracker isolation with a $R = 0.2$ cone radius is performed, and a p_T threshold equal to 5% of the lepton p_T.

Jets Two jets with uncalibrated $E_T > 30\,\text{GeV}$ and $|\eta| < 3$ are requested, and a veto on additional jets with uncalibrated $p_T > 20$ is applied. Extra jets from calorimeter noise are suppressed by requiring at least two tracks within the jet cone. Combined secondary vertex b tagging is applied to both jets, and both must have positive discriminator (a $disc > 0$ cut corresponds to $\simeq 60\%$ efficiency).

Additional requirements $E_T^{miss} > 30\,\text{GeV}$ is required to provide rejection of non W background like $Zb\bar{b}$ or QCD jet production. The transverse mass of the lepton and missing transverse energy is also computed, and required to be less than 100 GeV, which allows greater rejection of dileptonic $t\bar{t}$ and tW processes.

The preselection efficiencies for the signal and main backgrounds are listed in table 13.2. The efficiencies for Wt associated production is $0.34 \pm 0.01\%$ for semi-leptonic and $0.24 \pm 0.02\%$ for di-leptonic decays, while Wjj has only $0.019 \pm 0.002\%$ efficiency because of the rejection factor ~ 200 obtained requiring two b tags; efficiency for the Z sample is negligible ($0.008 \pm 0.004\%$).

QCD jet background was not considered, as it was found to be negligible in t channel analysis, and here an additional b tag is required, further reducing the selection efficiency.

[1] The introduction of this channel in HTL, with thresholds similar to the $\tau \times j$ one, is still under study and has not been approved jet; anyway, its presence is not critical for this analysis.

Table 13.2: Efficiencies of the preselection cuts, with respect to the initial number of events, for the signal and the main backgrounds. HLT includes 1μ, $1e$ and $e \times j$ triggers. Uncertainties are from simulated statistics only.

	s ch.	**t ch.**	**$t\bar{t}$**	**$Wb\bar{b}$**
HLT	$37.5 \pm 0.2\%$	$42.5 \pm 0.1\%$	$30.1 \pm 0.1\%$	$29.4 \pm 0.1\%$
Isolation	$33.7 \pm 0.2\%$	$39.0 \pm 0.1\%$	$21.7 \pm 0.1\%$	$28.2 \pm 0.1\%$
E_T^{miss} cut	$27.3 \pm 0.2\%$	$31.9 \pm 0.1\%$	$17.4 \pm 0.1\%$	$22.6 \pm 0.1\%$
$M_T(W)$ cut	$23.2 \pm 0.2\%$	$26.3 \pm 0.1\%$	$13.6 \pm 0.1\%$	$18.4 \pm 0.1\%$
≥ 2 jets; $p_T(j)$	$11.9 \pm 0.1\%$	$11.5 \pm 0.1\%$	$11.9 \pm 0.1\%$	$0.88 \pm 0.03\%$
jet veto	$8.9 \pm 0.1\%$	$8.2 \pm 0.1\%$	$1.84 \pm 0.04\%$	$0.76 \pm 0.03\%$
b-tag	$3.07 \pm 0.07\%$	$0.72 \pm 0.02\%$	$0.28 \pm 0.02\%$	$0.14 \pm 0.01\%$

13.3.3 Event reconstruction

Neutrino The neutrino is reconstructed from E_T^{miss} by imposing the constraint $m(E_T^{miss} + \ell) = m_W$. If the quadratic equation for $p_z(\nu)$ has two complex conjugate solutions, the common real part is chosen: the distribution of the quadratic discriminator Δ is peaked near zero (figure 13.1(a)), but detector effects and lack of total hermeticity introduce uncertainties, and negative Δ's become possible (figure 13.1(b)); whenever a negative Δ is found, most likely at parton level it was $\Delta \sim 0$, so that ignoring the complex part of the solution gives a satisfactory estimate of the correct neutrino p_z (see section 14.1.1 for more details). If two real solutions are available, the one giving minimum $|p_z(\nu)|$ is chosen, like in the t channel analysis.

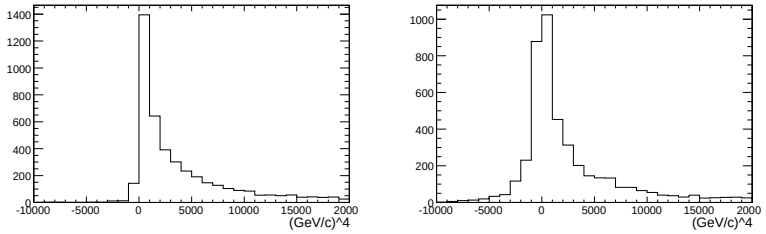

(a) Parton level Δ (b) Reconstructed Δ

Figure 13.1: Discriminator of the quadratic equation for the m_W constraint, at parton level (left plot) and computed with reconstructed objects (right plot)

Top quark As there are two b jets in the event, care must be taken in pairing the correct one with the reconstructed W. Two criteria have been considered: choosing the pairing with maximum $p_T(top)$ and choosing the b jet with minimum $Q_j \cdot Q_l$, where Q_j and Q_l are the jet and lepton charges, which means choosing the jet with charge "most opposite" to the lepton one; the latter method provides better performance, yielding the correct pairing in 67% of the events.

13.3.4 Event selection

After preselection and reconstruction additional cuts are performed in sequence:

1. b-tagging discriminator of the two jets, which should exceed 0.4 and 0.1 for the leading and subleading jet.
2. The p_T of both jets must be above 50 GeV; γ + jet calibration is used. This provides a rejection factor $\times 2$ against $Wb\bar{b}$.
3. Mass of the reconstructed top: $120\,\text{GeV} < M(\ell\nu b) < 220\,\text{GeV}$.
4. Transverse momentum of the top: $25\,\text{GeV} < p_T(\ell\nu b) < 160\,\text{GeV}$.
5. Vector sum of the transverse momenta of the top quark and the other b jet $\Sigma_T = |\vec{p}_T(t) + \vec{p}_T(b')| < 20\,\text{GeV}$.
   This provides a rejection factor $\times 4$ against $t\bar{t}$, and $\times 2$ against $Wb\bar{b}$ and t channel with a 73% efficiency for the signal
6. Scalar sum of the transverse momenta of all the reconstructed objects $H_T = |\vec{p}_T(\ell)| + |\vec{p}_T(\nu)| + |\vec{p}_T(b)| + |\vec{p}_T(b')| < 340\,\text{GeV}$.
   This rejects another $\sim$50% of $t\bar{t}$ background.

The values of the cuts have been optimized with the same genetic algorithm used for t channel analysis, GARCON. Table 13.3 contains the efficiencies and expected yields for $10\,\text{fb}^{-1}$. 273±4 signal events and 2045±63 background events (63% $t\bar{t}$, 30% t channel, 17% $Wb\bar{b}$) are forseen, with a signal over background ratio $S/B = 0.133 \pm 0.005$; listed uncertainties are for simulated statistics only.

Table 13.3: Summary of effective cross sections at each selection stage; all values are in picobarns except the last row that contains the expected yield for $10\,\text{fb}^{-1}$. Details on the trigger and preselection efficiencies are given in table 13.2.

	s channel	**t channel**	**$t\bar{t}$**	**$Wb\bar{b}$**
$\sigma \times BR$	3.33	81.7	833	100
Trigger	1.25	35	251	29
Preselection	0.102	0.59	2.33	0.14
$\text{jet}_{1,2}$ b-disc. > 0.4, 0.1	0.087	0.44	1.82	0.119
$p_T(\text{jet}_{1,2}) > 50\,\text{GeV}$	0.070	0.31	1.63	0.052
$M(\ell\nu b) \in [120, 220]\,\text{GeV}$	0.053	0.20	1.07	0.036
$p_T(\ell\nu b) \in [25, 160]\,\text{GeV}$	0.049	0.19	1.00	0.036
$\Sigma_T < 20\,\text{GeV}$	0.036	0.088	0.25	0.018
$H_T < 340\,\text{GeV}$	0.028	0.063	0.126	0.016
Expected events ($10\,\text{fb}^{-1}$)	276	629	1259	155

13.3.5 Selections for background normalization

Two different samples of $t\bar{t}$ background where selected for background normalization. For both, cuts are chosen in order to have good sample purity, no overlap with the signal selection, and such that systematic uncertainties affect the control region and signal region in similar way, so that the subtraction does not introduce large systematic uncertainties.

Di-leptonic control sample A control sample was obtained by selecting events which pass all the preselection requirements except that an additional lepton is required. The two leptons are required to be opposite in flavour to reduce Drell-Yan and Z background, and opposite in sign to avoid contamination from other sources like semileptonic b or c decays[2].

This sample has a 0.82% efficiency for dileptonic $t\bar{t}$ (expected yield 7700 events), and a purity of 98.6% $t\bar{t}$, the rest being mostly dileptonic tW events.

Semi-leptonic control sample the other control sample is prepared using the normal preselection requirements except that an additional jet is required. As the efficiencies are very high, only the cleanest sample with muons is used to reduce background contamination.

The purity for semi-leptonic $t\bar{t}$ in this region is 88%, with an expected yield of 65600 events for $10\,\mathrm{fb}^{-1}$, where contaminations are evenly equally distributed among other $t\bar{t}$ decays, tW, t channel single top and $W + jets$.

13.4 Systematic uncertainties

13.4.1 Theoretical uncertainties

Background cross sections A 5% uncertainty was assumed on the $t\bar{t}$ and $Wb\bar{b}$ background cross section, and a 4% for t channel single top.

Additional uncertainties are estimated by parameterizing the signal and background efficiencies as a function of the $\hat{s}$ kinematical variable in the sample with detector simulation, and then using the parton level distribution for $\hat{s}$ to compute the efficiencies for samples with different generator parameters.

These uncertainties were computed for the signal only, as the task was already computationally intensive.

Top quark mass One hundred samples with $m(top)$ values taken from a Gaussian distribution with mean 175 GeV and width 2 GeV where used to determine the sensitivity of the signal efficiency on the top mass. A systematic uncertainty $\delta\sigma/\sigma = 0.5\%$ was estimated from this source.

Parton density functions The results with $40+1$ CTEQ6L LO parton density functions, the best fit and the ones computed with $\pm 1\sigma$ in the independent 20 parameters, and the CTEQ6M NLO density were computed. The resulting uncertainty is 0.7%.

Initial and final state radiation The parameters for ISR/FRS where varied in the ranges $\Lambda_{QCD} = 0.15 - 0.35\,\mathrm{GeV}$ and $Q^2_{max} = 0.25 - 0.4\,\mathrm{GeV}^2$; the cross section dependence on radiation modelling was found to be $\delta\sigma/\sigma = 0.5\%$.

[2] In particular $b \to \ell$ decays of the other b quark in the event, or $b \to c \to \ell$ cascade in the b quark from the top decay

13.4.2 Experimental uncertainties

Integrated luminosity A 19% uncertainty on the cross section was estimated for the 5% uncertainty on the luminosity, as the ratio between the yiedls for signal and the backgrounds not normalizated on data is $\simeq 1/3$ and so the 5% is magnified by a factor four.

Jet energy scale Systematic uncertainties from jet energy scale uncertainties where calculated as described in section 10.2.2.

***b*-tagging efficiency** The uncertainty on the efficiencies from b-tagging efficiency was estimated to be $\pm 4\%$, as described in section 10.2.2.

13.5 Conclusions

Adding up all the uncertainties, which are listed in detail in table 13.4, the uncertainty on the cross section is

$$\frac{\mathbf{\Delta}\sigma}{\sigma} = \mathbf{18}\%\,(\text{stat}) \;\oplus\; \mathbf{31}\%\,(\text{syst}) \;\oplus\; \mathbf{19}\%\,(\text{lum}) \;=\; \mathbf{41}\%$$

Significance In the null hypothesis of no s channel single top production, the expected number of signal-like events is $2045 \pm 45(\text{stat}) \pm 105(\text{syst+lum})$; the significance computed in the Gaussian approximation and with Poisson statistics yield both $S \simeq 2.4$.

Possible improvements Some improvements are probably possible: normalization of the t channel background using data, for example, will reduce the luminosity uncertainty to 8%, and the total uncertainty to 35%.

The greatest source of uncertainty is anyway from the jet energy scale effect on $t\bar{t}$ background: if it were possible to halve just this contribution, in combination with t channel background normalization, the systematic uncertainty would be reduced to 18%, the total uncertainty to 27% and the significance would be 3.3. For higher integrated luminosities, also this systematic uncertainty would decrease thanks to the increased statistic for the more precise $Z + jet$ energy scale calibration, and energy flow methods.

Table 13.4: Statistical and systematical uncertainties for s channel analysis, for $10\,\mathrm{fb}^{-1}$ integrated luminosity. Theory includes PDF, $m(top)$ and ISR/FSR for signal, and cross section uncertainty for backgrounds; entries which give negligible contribution due to the background normalization are suppressed. In the last column, contributions to the cross section uncertainty from each source are provided.

	s ch.	**t ch.**	**$t\bar{t}$**	**$Wb\bar{b}$**	**$\Delta\sigma/\sigma$**
Yield	273	630	1260	155	
Statistics	6.1%	4.0%	2.8%	8.0%	18%
Theory	1.1%	4.0%	—	5.2%	4.2%
Jet energy scale	1.1%	1.3%	6.0%	4.5%	27%
b tagging	4%	4%	4%	4%	10%
Luminosity	5%	5%	—	5%	19%

Chapter 14

New developments

14.1 Reconstruction

14.1.1 Neutrino reconstruction

In all semileptonic single top analyses the longitudinal momentum of the neutrino is determined by imposing the W mass constraint, but different prescriptions are used when the quadratic equation has complex solutions: in the t-channel analysis the W mass in the equation was increased until a real solution could be found; in s-channel and tW analysis the common real part of the two complex solutions was used, for the reasons already stated in 13.3.3.

The resolution on the neutrino pseudorapidity that can be obtained with the two methods has been determined using a sample of about 700k t-channel events produced with TopReX + FAMOS. In order to select only events where the reconstructed objects are correctly matched to the generator level ones, the following cuts where applied: $\Delta R(\ell_{gen}, \ell_{rec}) < 1$, $\Delta\phi(\nu, E_T^{miss}) < 1$, $|({p_T}^{gen} - {p_T}^{rec})/p_T| < 25\%$

The prescription of using the real part of the solution was found to be more accurate, giving a RMS resolution on $\eta(\nu)$ of 0.91, compared to the 1.07 obtained from the other prescription; the tails of the $|\Delta\eta|$ distribution are also improved, as plotted in figure 14.1.

The prescription used to choose the solution for $p_z(\nu)$ when the equation has two real roots is the same in all analyses: select the solution giving smaller $|p_z(\nu)|$. The performance of this choice was tested on the same t channel single top sample described above; the choice is found to be correct in $64.7 \pm 0.3\%$ of the events (where the uncertainty comes only from the simulated statistics).

14.1.2 Jet cleaning

Noise jets in tW In the analysis of the tW associated production the characteristics of extra jets, induced mostly by noise, but also by pileup and underlying event, were studied in detail; selection cuts were chosen to provide good rejection against those jets, necessary for having a good jet veto. As already described in section 12.3.2, calorimeter and tracker information was used to build discriminating variables; a high performance of the jet preselection cuts was achieved,

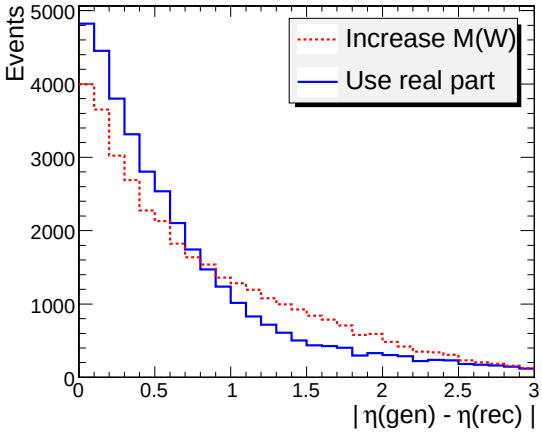

Figure 14.1: Absolute value of the difference between generated and reconstructed neutrino pseudorapidiy, from t-channel single top events, using two different prescriptions to deal with complex solutions of the equation for $p_z(\nu)$

but this introduced a large dependence on the amount of pileup.

Pileup The same issues of the extra jets was found also in other analyses in which jet veto was important, such as in searches for $H \to W\,W$; in that case, real jets from pileup where the main source of the bad performance of the selection. A good rejection of pileup jets was achieved using tracker information *including vertex reconstruction*: for each jet, an α value was computed as the ratio between the p_T of the tracks within the cone, and compatible with the primary vertex of the W decays, and the total jet p_T. A minimum threshold $\alpha > 0.2$ (or sometimes 0.3) was used to define jet association to the primary vertex.

In the reanalysis of the single top quark channels, we will try to use the α cut to reduce the sensitivity to pileup, which is among the largest systematic uncertainties in the tW analysis.

14.2 Systematic uncertainties

14.2.1 Jet energy scale recalibration

All the single top analyses presented here are focused on measuring the production cross section and not the top quark mass, so that they are not inherently sensitive to jet energy scale; on the other hand, the selection relies critically on the number of jets above some threshold. What is really relevant, in this case, is the consistency between data and simulation, and not the absolute scale.

Because of this, a simple method is here proposed to reduce such uncertainty, by recalibrating the energy scale in the simulation on the data using the W mass peak extracted from semileptonic $t\bar{t}$ decays. A clean sample of $t\bar{t}$ events will be selected among the measured data and the Monte Carlo samples, and the ratio

between the fitted values for the W mass peak will be used as a measure of the relative difference in jet energy scales; in following analysis, the momenta of the jets in the simulated samples will be rescaled by this amount, so that the computed selection efficiencies will be more accurate.

Selection of the control sample

Events are selected in the inclusive electron and inclusive muon trigger streams. In order to reduce possible systematic uncertainties, the offline selection requirements are kept simple:

- **One lepton** with $p_T > 20\,\text{GeV}$, and no other leptons with $p_T \geq 10\,\text{GeV}$
- **Two b jets** with $p_T > 35\,\text{GeV}$, and a combined secondary vertex b-tagging discriminator $disc > 2$ (which corresponds to $\sim$50% efficiency)
- **Two light jets** with $p_T > 30\,\text{GeV}$, not b tagged ($disc < 0$)
- **No other jets** with $p_T > 30\,\text{GeV}$

The W mass peak is extracted from a Gaussian fit in the range $65\,\text{GeV} < m(jj) < 105\,\text{GeV}$; the Gaussian approximation would be good in a larger range, but a safety margin of 5 GeV has been left out at both ends so that the approximation remains valid in the whole fit range even when the position of peak is changed by the jet energy scale miscalibration.

Without miscalibration The distribution of $m(jj)$ is shown in figure 14.2, obtained on a sample of inclusive $t\bar{t}$ events generated with PYTHIA and OSCAR+ORCA. Jets already calibrated with the $\gamma + jet$ method were used. The selection efficiency is 0.7% (2.4% if only semileptonic top decays with e,μ are considered), so that 57200 events are expected for $10\,\text{fb}^{-1}$; the statistical uncertainty on the reconstructed W mass on our simulated sample was 0.7 GeV; rescaling to the statistics expected for $10\,\text{fb}^{-1}$, a resolution of $\pm 0.24\,\text{GeV}$ on the position of the mean is expected.

With miscalibration A miscalibration on the jet energy scale was simulated rescaling jet momenta by an amount equal to the expected jet energy scale uncertainty for $10\,\text{fb}^{-1}$ (see 10.2.2). The position of the fitted $m(jj)$ peak is shifted by $\sim$2.7% for a positive or negative miscalibration; this corresponds to $\sim 2\,\text{GeV}$, a 12σ difference with respect to the statistical accuracy attainable for $10\,\text{fb}^{-1}$.

Backgrounds The selection was tested on samples of W+$jets$ (AlpGen+FAMOS), $Wb\bar{b}$, t channel single top and semileptonic tW (all TopRex+FAMOS); 2300 events from t-channel single top and 1500 events from tW are expected for $10\,\text{fb}^{-1}$, while background contributions from non top samples are found to be negligible, so that a signal over background $S/B \simeq 14$ is achieved with these cuts.

The effect of the background on the position of the $m(jj)$ peak was tested: varying the amount of background by $\pm$100% the position of the peak was

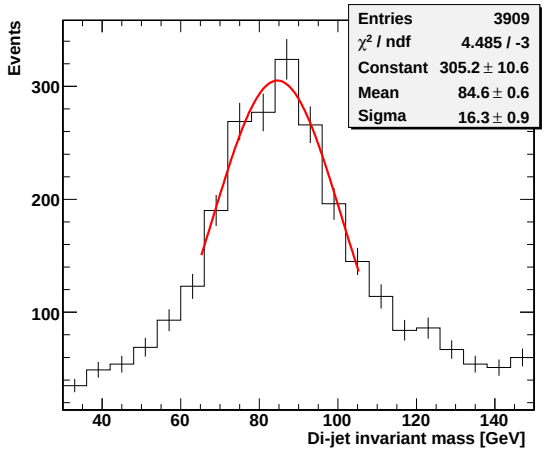

Figure 14.2: W mass peak from $W \to jj$ extracted from semi-leptonic $t\bar{t}$ events.

altered by $\lesssim 0.02\,\text{GeV}$, negligible in comparison with the statistical accuracy of the fit.

Background from QCD jets has not been investigated jet, but the requirement of two b tags and one isolated lepton should provide a good rejection; if necessary, the selection cuts can probably be made more strict without significant loss in the statistical accuracy of $m(jj)$.

Sensitivity We have found that the position of a $m(jj)$ peak is a good observable to detect a jet energy scale miscalibration, as the shift in the peak position induced by a miscalibration of the amount expected for $10\,\text{fb}^{-1}$ is much larger than the statistical accuracy available on the position of the peak. The expected background is very small, and its contribution on the peak position is negligible.

Recalibration

The jet energy scale miscalibration is not expected to be flat in the jet E_T, but through the $m(jj)$ peak only one value for the miscalibration can be extracted, averaged on the energy range of the jets used to reconstruct the W ($40\,\text{GeV} \lesssim E_T \lesssim 70\,\text{GeV}$)

When recalibrating the jet energy scale in the simulation, at least two options are available: to use a flat recalibration, rescaling all jets by the ratio between the position of the fitted peak in the data and in the simulation, or to assume the E_T dependence of the miscalibration known.

Flat recalibration Recalibrating all jets by the $m(jj)_{data}/m(jj)_{sim}$ is not expected to be optimal, as jets selection efficiencies are more affected by the miscalibration of lower E_T jets ($20 - 35\,\text{GeV}$), which is expected to be $1.5 - 2$ times larger than the miscalibration for jets with $E_T \gtrsim 50\,\text{GeV}$.

Nevertheless, this procedure is almost model independent, and the results presented in the following will show that an appreciable reduction of the systematic uncertainty from jet energy scale is expected using it.

E_T dependent recalibration If the E_T dependence of the miscalibration is assumed to be know, dependent on a *single parameter*, it is possible to use simulated data with different miscalibrations to extract the dependence of the parameter from the shift in the $m(jj)$ mass peak, and then apply a recalibration with the correct parameter to account for the $m(jj)$ peak position measured on the data.

This procedure is potentially able to reduce the systematic uncertainties on selection efficiencies even more than the flat recalibration, but systematic uncertainties from the assumed E_T dependence are expected. No estimate of the uncertainties on this dependence has jet been investigated, so we are not able to determine the induced uncertainty on the recalibration procedure now.

The performance of the flat recalibration is expected to be dominated by the difference in the jet energy scale miscalibrations in the two E_T regimes; for more advanced model the dominant uncertainty will probably be from the uncertainties on the assumed E_T dependence, as the uncertainties from statistics and other systematic effects is expected to be small.

As a consequence, it is not possible to have a reliable estimate of the performance of the more advanced method jet, and the flat method has been used in all the following; the results appear to be good even with this simpler method.

Possible systematic uncertainties

As long as all the backgrounds are negligible, the method is clearly unaffected by uncertainties that change the number of collected events without altering the distribution of the $m(jj)$ variable; uncertainties from integrated luminosity and production cross sections can then be neglected.

The uncertainty on b tagging efficiency should play little role, as even a difference in efficiency with non trivial dependence on the jet p_T will hardly affect the shape.

Uncertainties from the top quark mass and parton density functions are expected to give very small contributions as they should only affect the momentum spectrum of the produced W boson, so that effects on the $m(jj)$ peak are expected only indirectly through the differences in the selection efficiency caused by the different distribution of the kinematic variables.

Pile-up and ISR/FSR should give only minor contributions to the $m(jj)$ shape, as the only direct contribution is expected when one of the two light jets used to reconstruct the boson is not from a W decay but $m(jj)$ nevertheless falls inside the fiducial region. Contributions to the selection efficiency could be larger, as the presence of an additional jet from pileup would cause the event to be rejected, but this will not alter directly the shape of the fitted function.

Uncertainties from the fragmentation model can be absorbed in the jet energy scale uncertainty, and can then be ignored. Some uncertainty is instead expected in the possible miscalibration between the energy scale of light jets and b jets, but at the moment there is no estimate on the expected amount of such a miscalibration, so the uncertainty introduced by this cannot be evaluated.

Performance

Toy selections The effectiveness of this correction has been tested by looking at the uncertainty on the efficiency of the same inclusive $t\bar{t}$ sample under sets of kinematic cuts which resemble those used in single top analysis; only cuts on the jet and lepton p_T and η and the jet veto have been included. The relative uncertainty on the selection efficiency caused by the jet energy scale miscalibration is shown in table 14.1 both with and without the recalibration procedure; a sizable reduction, about of a factor two, is observed in all the "toy selections".

It should be noted that in most of the analyses some methods are already used to reduce the systematic uncertainty, such as by estimating the background using a control sample which is affected by jet energy scale in a way similar to the signal; it should be investigated whether the two corrections stack well, or the performance of one of the two is reduced by the presence of the other.

Table 14.1: Effect of jet energy scale recalibration on the uncertainties on efficiency of the $t\bar{t}$ sample under kinematic cuts which resemble those used in the different single top analyses.

Cut set	Efficiency	$\Delta\epsilon/\epsilon$ [%] Up	Down	$\Delta\epsilon/\epsilon$ [%] (Rec.) Up	Down
t channel	0.19%	−3.1%	6.5%	−2.6%	1.8%
s channel	0.37%	−7.2%	6.4%	−4.5%	1.7%
tW (1ℓ)	1.84%	−3.9%	3.1%	−1.4%	0.4%
tW (2ℓ)	0.07%	−23%	27%	−13%	12%

Real selections The performance has been tested also on real selections, and the results will be listed later in the sections devoted to each selection. As the systematic uncertainties have not jet been fully evaluated, a crude ±1% uncertainty has been assumed on the position of the $m(jj)$ peak, 3.3 times the expected statistical accuracy.

The uncertainty on the selection efficiencies have been calculated both with no rescaling, with the rescaling obtained by the expected ±2.7% shift in the W peak position and the two extreme values ±1.7%, ±3.7% of the shift, always assuming ±1% uncertainty on the peak position. The improvement is good: the recalibration procedure reduces the systematic uncertainty by $40 - 60\%$, and sometimes even more, and the performance is scarcely affected by the ±1% assumed uncertainty on the peak.

14.3 Single top t channel revisited

14.3.1 Changes made

Samples Different simulated samples were used, as those used in the other analysis were not available; TopReX was used for single top processes and $Wb\bar{b}$,

AlpGen for $W+nj$ ($n = 2, 3, 4$)[1], PYTHIA for the $t\bar{t}$ background. FAMOS fast simulation was used on all samples except $t\bar{t}$ for which fully simulated samples where readily available.

Reconstruction Many differences have been introduced in the reconstruction process.

- The analysis is no longer restricted to the muon sample, also electron events are accepted; a cut is applied on the presence of a second lepton, independent on the flavour.
- $\gamma + jet$ calibration was used instead of the MC jet, so that jets are calibrated on the momenta of the partons and not those of the hadronized particles. While the calibrations are similar for $E_T \gtrsim 50\,\text{GeV}$, there are non trivial differences in the low energy region, which is very important for the jet veto.
- Extra jets from noise and pileup were removed by using a cut on the α parameter, the ratio between the p_T of the tracks within the cone and *compatible with the primary vertex* and the jet E_T, as defined in 14.1.2; this allows to lower the threshold for the jet veto without loosing efficiency due to calorimeter noise. Vertex association should keep the performance stable even with different amount of pileup.
- The neutrino was reconstructed as described in 14.1.1, which introduces smaller tails in the $|\eta(\nu)|$ resolution.

14.3.2 Reproducing the other selection

The analysis was first tested using the same cuts of the old analysis, except for what stated above, and the results show some marked differences.

Selection efficiencies The signal selection efficiency was found to be lower, so that the expected yield at $10\,\text{fb}^{-1}$ is only 1218 ± 35 (here, and below, uncertainties are from simulated statistics) instead of the 2400 foreseen in the other analysis.

Efficiencies for the backgrounds were even more different: the $t\bar{t}$ background is almost completely suppressed by the jet veto[2], so that a yield almost 100 times smaller is expected (3 ± 7). The main backgrounds are expected from $W+2j$ (312 ± 64), $W+3j$ (91 ± 37), semi-leptonic tW production (27 ± 6), $Wb\bar{b}$ (23 ± 8). Simulated statistics for $W + 4j$ was somewhat lacking (50k events), so that only an upper bound $N \leq 48$ (68% CL) was obtained; as all the events of the sample were rejected at an early selection stage, the estimate is probably largely conservative.

With the yields listed above, a signal to background ratio of 2.7 could be achieved.

[1] $W + 1j$ was not used, as it was found to be negligible in the original analysis, and not AlpGen ntuples from the official production were available

[2] The difference between $\gamma + jet$ and MC jets is though to be the cause of this, but it has not been verified yet

Systematic uncertainties Only the main systematic uncertainties where re-evaluated:

- The statistical uncertainty is only slightly larger (3.4% instead of 2.7%), as the smaller signal efficiency is partially balanced by higher S/B.
- The dependence on the **background cross sections** is similar to the one found in the other analysis, as S/B is larger but the $W + nj$ cross section will be known with 10% accuracy, while for $t\bar{t}$ the value will be more precise (5%): a $\pm 3.7\%$ uncertainty is expected from this source.
- Integrated luminosity has a smaller effect on the cross section uncertainty, only $\pm 6.9\%$, as there is less background
- The uncertainty on b tagging efficiency, computed as in the semileptonic tW analysis using $\delta = 0.19$ (see sec. 10.2.2), was found to be $-1.5\%/+0.7\%$, smaller than the simple $\pm 4\%$ estimate.
- The jet energy scale introduces a sightly larger uncertainty ($-5.5\%/+5.0\%$ instead of $\pm 4.3\%$) in this analysis.

The total systematic uncertainty is $-10.2\%/+9.9\%$, not far from the $\pm 12.1\%$ which was found in the other analysis.

Jet energy scale recalibration The procedure of jet energy scale recalibration introduced in section 14.2.1 was tested on this analysis. To test the robustness of the procedure, three different values for the position of the fitted $m(jj)$ were tried: the value expected in absence of other systematical or statistical uncertainties ($\delta m/m = \pm 2.7\%$ for the jet energy scale uncertainty expected at $10\,\mathrm{fb}^{-1}$), and two nearby values (± 1.7 and ± 3.7) which should be a conservative esitimates of the possible uncertainties on $m(jj)$.

The systematic uncertainty from jet energy scale without calibration is $-5.5\%/+5.0\%$, while the values found for the three recalibrations were: $-2.9\%/+3.1\%$ for $\delta m/m = \pm 1.7\%$, $-2.2\%/+1.4\%$ for $\delta m/m = \pm 2.7\%$ and finally $-1.5\%/+0.7\%$ for $\delta m/m = \pm 3.7\%$. It appears that for whatever guess of $m(jj)$ the uncertainty from jet energy scale is reduced by a significant amount, and for the expected $\delta m/m$ the systematic uncertainty is reduced to less than half.

14.3.3 Optimized selection

As the relevant backgrounds where found to be different, the cuts have been reoptimized again. After a preselection with loose cuts, the selection cuts where optimized in order to minimize the total uncertainty on the cross section, using the flexible JGAP[3] package.

A good improvement on the selection was found: the expected total uncertainty was lowered to $\pm 7.9\%$, by tightening the cuts, with all three main sources of uncertainty (statistics, luminosity and jet energy scale) contributing by almost the same amount. Expected yields for $10\,\mathrm{fb}^{-1}$ are listed in table 14.2, and the detailed breakdown of the systematic uncertainty is given in table 14.3. The achievable signal over background is 8; if sets for which only an

[3] Java Genetic Algorithm Package, [JGAP]

upper limit on the expected yield are available are conservatively added to the background count with a number of events equal to the upper limit, the signal over background is still good (4.7).

Again, if the jet recalibration is used, the uncertainty on the jet energy scale is reduced by a substantial amount ($> 40\%$) with all the three tested values for the position of the fitted $m(jj)$.

Table 14.2: Expected yields at $10\,\mathrm{fb}^{-1}$ in the reoptimized t channel analysis. The listed uncertainty is from MC statistics. When the simulated statistics was too low and no events where accepted, the upper limit at 68% CL is given, marked with (†); the results for $t\bar{t}$ are from the sum of a dileptonic sample (with yield 1 ± 1) and a non dileptonic sample with yield ($0 \pm 8^{\dagger}$).

Process	Yield $[10\,\mathrm{fb}^{-1}]$	
t channel	550	± 23
W + 2j	26	± 18
W + 3j	15	± 15
tW (1ℓ)	12	± 4
Wb$\bar{\mathbf{b}}$	8	± 4
t$\bar{\mathbf{t}}$	1	$\pm 8^{\dagger}$
W + 4j	0	$\pm 48^{\dagger}$

Table 14.3: Expected uncertainties in the reoptimized t channel analysis. The uncertainty from simulated statistics was not added to the total.

	$\boldsymbol{\Delta\sigma/\sigma}$	
Statistics	-4.5%	$+4.5\%$
$\sigma(tW)$ [$\pm 15\%$]	-0.3%	$+0.3\%$
$\sigma(W + nj)$ [$\pm 10\%$]	-1.1%	$+1.1\%$
luminosity [5%]	-5.6%	$+5.6\%$
jet energy scale	-2.8%	$+3.1\%$
b tagging	-1.2%	$+0.6\%$
Total uncertainty	$\mathbf{-7.9\%}$	$\mathbf{+7.9\%}$
Simulated statistics	-2.9%	$+2.9\%$

14.4 Single top tW channel revisited

14.4.1 Changes made

Simulated samples The samples used for this new analysis are very similar to those that were used for the original analysis; the two main differences are the use of full simulation (OSCAR+ORCA) for $t\bar{t}$ also in the semi-leptonic decay mode, as they were readily available, and the use of AlpGen+FAMOS for the $WW + jets$ background.

Jet cleaning Removal of extra jets was obtained with cuts on the α variable (defined in section 14.1.2) and the requirement of at least *two tracks* within the jet cone and associated with the event vertex; the jet quality cuts are applied only for $|\eta| < 2$, where the tracker is fully efficient. A cut $\alpha > 0.1$ was used in semi-leptonic events, while for the di-leptonic ones $\alpha > 0.2$ was used as the only jets that should be present are b jets, for which larger values of α are expected.

Top reconstruction In semi-leptonic events the $W \leftrightarrow b$ pairing is done using a simple angular matching criteria, by pairing the b with the nearest reconstructed W, as no appreciable degradation of the distribution of the reconstructed top mass was found with respect to the previous analysis.

In any case, cuts on the reconstructed top p_T and mass were not found to improve the performance of the selection significantly, confirming the results of the previous analysis, so that the correctness of the $W \leftrightarrow b$ pairing is not important.

14.4.2 Semi-leptonic decay mode

Preselection Events were preselected by applying a loose set of cuts in addition to the High Level Trigger selection: one b-jet ($|\eta| < 2.5$, $p_T > 30\,\text{GeV}$, b-tag. discr. > 0) and two light jets ($|\eta| < 2.5$, $p_T > 20\,\text{GeV}$, b-tag. discr. < 0) were required; a veto was applied on additional jets ($p_T < 35\,\text{GeV}$) and leptons ($p_T < 10\,\text{GeV}$), and additional cuts were imposed to the missing transverse energy ($E_T^{miss} > 20\,\text{GeV}$) and the transverse mass of the leptonically decaying W ($M_T(\ell\nu) < 180\,\text{GeV}$).

A separate preselection stream was used to obtain a clean sample of $t\bar{t}$ background, with the same cuts except that one additional jet was required ($|\eta| < 2.5$, $p_T > 30\,\text{GeV}$), and the cut on the transverse W mass and the b jet p_T were relaxed ($M_T(\ell\nu) < 200\,\text{GeV}$, $p_T > 30\,\text{GeV}$).

Selection After the preselection, the relevant backgrounds were found to be $t\bar{t}$, $W + jets$ and, less important, t-channel single top. Three discriminating variables were found:

- the invariant mass of the hadronically decaying W boson (plot 14.3), which has good discriminating power against non $t\bar{t}$ background that does not contain any $W \to jj$ decay.
- the transverse mass of the W boson decaying to $\ell\nu$ (plot 14.4), useful to discriminat $t\bar{t}$ background where the missing energy is given also by the additional jets which survive the jet veto.
- the discriminator from the combined secondary vertex b-tagging algorithm (14.5), which can provide good rejection of the $W + jets$ background.

The cuts chosen to select signal events were: $60\,\text{GeV} < M(W \to jj) < 100\,\text{GeV}$, $M_T(W \to \ell\nu) < 130\,\text{GeV}$, b-discr. > 2. In addition, the energy thresholds for the light jets were raised to 30 GeV, and the jet veto was made more strict by requiring no additional jets above 30 GeV. An additional loose cut $110\,\text{GeV} < m(top) < 230\,\text{GeV}$ was applied, which slightly improves the rejection of $W + jets$.

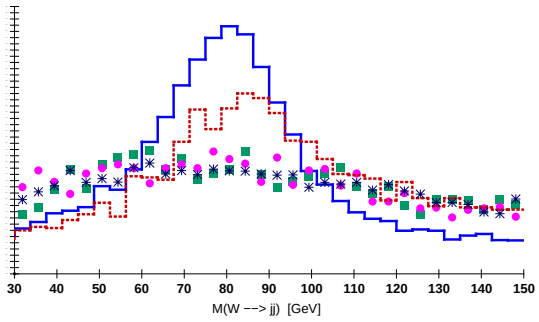

Figure 14.3: Invariant mass of the hadronically decaying W boson: tW (solid blue histogram), $t\bar{t}$ (dotted red histogram), $W + 2j$ (dots), $W + 3j$ (squares), t-channel single top (crosses). Histograms for each sample are normalized to unit area.

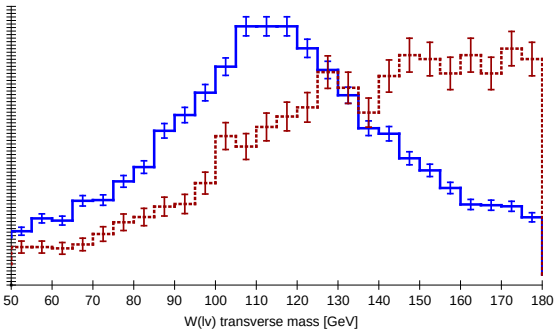

Figure 14.4: Transverse mass of the W boson decaying to $\ell\nu$: tW (solid blue histogram), $t\bar{t}$ (dotted red histogram); distributions for $W + j$ and t-channel single top are very similar to the one for tW. Histograms for each sample are normalized to unit area.

The expected yields for $10\,\text{fb}^{-1}$ are 1616 for tW signal and 2937 for the backgrounds: 1594 ($W + jets$), 868 ($t\bar{t}$), 431 (t channel); a signal to background ratio of 0.55 was achieved with these cuts, a significant improvement over the previous analysis for which $S/B \simeq 0.19$ with almost the same signal efficiency.

$W + jets$ background normalization The control sample for $W + jets$ background was obtained using the same selection cuts used for signal except for the b tagging discriminator ($0.5 < b$-tag. discr. < 2) and the $M(W \to jj)$ where the cut was inverted in order to select events *outside* the $[60\,\text{GeV}, 100\,\text{GeV}]$ mass window.

The expected yields for $10\,\text{fb}^{-1}$ are 4543 ($W + jets$), 331 ($t\bar{t}$), 214 (tW) and 320 (t channel).

$t\bar{t}$ background normalization A control sample was obtained by selecting events with two b jets ($p_T(1) > 35\,\text{GeV}$, $p_T(2) > 30\,\text{GeV}$, b-tag. discr. > 1), two light jets ($p_T > 30\,\text{GeV}$, b-tag. disc. < 0) and no other jets with p_T

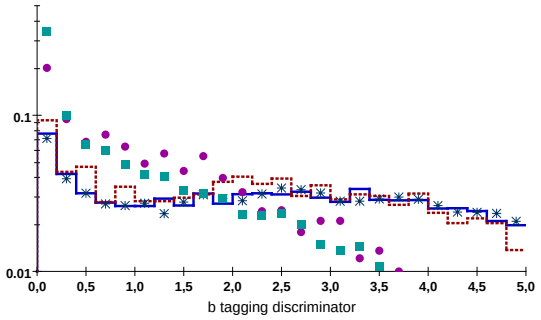

Figure 14.5: Value of the b-tagging discriminator: tW (solid blue histogram), $t\bar{t}$ (dotted red histogram), $W + 2j$ (dots), $W + 3j$ (squares), t-channel single top (crosses). Histograms for each sample are normalized to unit area. Note the semi-logarithmic scale.

Table 14.4: Expected yields after each cut in the semi-leptonic tW analysis, for an integrated luminosity of $10\,\text{fb}^{-1}$.

	tW	**W + jets**	**$t\bar{t}$**	**t ch.**	**$Wb\bar{b}$**
Preselection	13027	109819	18053	10495	1411
b-tagging	8550	24109	11372	6995	795
Jet p_T	5436	11973	8470	3308	220
Jet veto	4872	11291	6666	2988	199
$E_T^{miss} > 30\,\text{GeV}$	4227	9623	5845	2667	179
$M_T(W \to \ell\nu)$	2917	7164	2349	2091	145
$M(W \to jj)$	1930	2144	1057	544	49
$M(top)$	1616	1594	868	431	44
Final yield	1616	1594	868	431	44

above 30 GeV. To increase purity, additional two cuts were applied to the reconstructed W bosons ($55\,\text{GeV} < M(W \to jj) < 105\,\text{GeV}$, $M_T(W \to \ell\nu) > 110\,\text{GeV}$.

The expected yields for $10\,\text{fb}^{-1}$ are 1500 ($t\bar{t}$), 127 (tW), 82 (t channel); the other backgrounds were found to be negligible.

Cross section extraction In order to extract the cross section, the efficiencies for the signal, $t\bar{t}$ background and $W + jets$ background for each of the three selections were determined from simulated events, together with the expected yields from all the other background processes. The three cross section were then extracted by solving the 3×3 set of linear equations; thanks to the purity of the two control samples, the equations are far from being degenerate even with the low purity of the signal selection.

Systematic uncertainties The systematic uncertainties from background cross sections, luminosity, jet energy scale and b-tagging efficiencies have been evaluated for this analysis; the systematic uncertainty from the parton density

functions and the amount of pile-up were taken from the old analysis.

For the pile-up uncertainty, a significant improvement is expected in this analysis as the threshold for the jet veto was increased, and event vertex association was used in the jet preselection; a re-evaluation of the uncertainty will be done soon, but the procedure is lengthy.

Comparing the results from this analysis (table 14.5) with the ones achieved in the old one (table 12.5), a significant improvement is found in most sources of uncertainty: statistics (7.5% → 5.2%), jet energy scale (9.4% → −2.9/+ 7.1%) and integrated luminosity (7.8% → 6.1%).

The total uncertainty on the cross section, even by conservatively assuming the same uncertainty from the pile-up amount, is reduced from ±18.4 to −14.0%/+14.9%.

Table 14.5: Expected uncertainties in the new semi-leptonic tW channel analysis. The uncertainty from simulated statistics was not added to the total. Uncertainties with † were taken from the old analysis.

Statistics	−5.2%	+5.2%
$\sigma(Wbb)$ [±10.0%]	−0.3%	+0.3%
σ(t ch.) [±4.0%]	−0.8%	+0.8%
luminosity [5%]	−6.1%	+6.1%
jet energy scale	−2.9%	+7.1%
b tagging	−3.9%	+0.0%
PDF†	−1.6%	+1.6%
Pile-up†	−10.3%	+10.3%
Total uncertainty	**−14.0%**	**+14.9%**
Simulated statistics	−13.4%	+13.4%

14.4.3 Di-leptonic decay mode

Preselection Events were preselected by applying cuts to the events accepted the High Level Trigger inclusive leptonic channels: two leptons of opposite flavour an sign, with $p_T(1) > 20\,\text{GeV}$, $p_T(2) > 15\,\text{GeV}$, and a b jet ($p_T > 30\,\text{GeV}$, $|\eta| < 2.5$, b-tag. discr. > 0) were required; one additional jet with $|\eta| < 3.0$ was allowed, but a veto was applied on the presence of a third jet with $p_T > 30\,\text{GeV}$. A cut on the missing transverse energy was also applied, with a threshold of 20 GeV.

Selection Some improvement in the selection was achieved by considering the variable

$$\vec{\Sigma}_T = \vec{p}_T(\ell_1) + \vec{p}_T(\ell_2) + \vec{p}_T(b) + \vec{E}_T^{miss}$$

which does not include the $\vec{p}_T$ of the second jet. The distribution of this variable after preselection for the signal and the dominant background (dilep. $t\bar{t}$) is shown in figure 14.6.

Signal-like events were selected with these cuts: $p_T(\ell_{1,2}) > 20\,\text{GeV}$, $|\Sigma_T| < 39.3$, $p_T(jet\,2) < 29.1\,\text{GeV}$, b-tagg. discr. > 2, and a veto on additional jets with $p_T > 20\,\text{GeV}$.

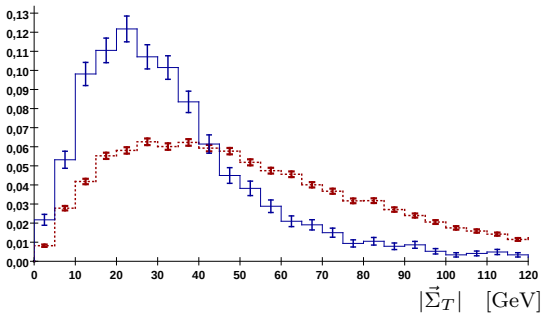

Figure 14.6: $|\vec{\Sigma}_T|$, the vector sum of the transverse momenta of the two leptons, the b jet and the E_T^{miss}, for dileptonic tW signal (solid blue histogram) and dileptonic $t\bar{t}$ background (dotted red histogram). Histograms have been separately normalized to unit area.

A control sample to normalize $t\bar{t}$ background was also extracted by requiring: $p_T(jet\,2) > 35\,\text{GeV}$, b-tagging discriminators > 0.98 (b jet), > 0.83 (jet 2), $|\Sigma_T| > 56.8\,\text{GeV}$ and the same jet veto.

The thresholds for the cuts were optimized with genetic algorithms in order to minimize the total uncertainty on the cross section.

The expected signal yield for $10\,\text{fb}^{-1}$ of integrated luminosity is 593 signal events and 1729 $t\bar{t}$ background events, with all other backgrounds being negligible; in addition, 1882 $t\bar{t}$ events are expected in the background control sample, with negligible contamination from signal and t-channel single top (18 and 13 events respectively).

Systematic uncertainties As in the analysis of the semi-leptonic decay mode, uncertainties from statistics, background cross sections, integrated luminosity, b tagging efficiency and jet energy scale were evaluated, while the uncertainties from PDFs and pileup were taken from the old analysis.

Before optimization the uncertainty is dominated by the uncertainties on the jet energy scale (with $\Delta\sigma/\sigma \sim 20\%$), in accord to what was found in the old analysis; after the optimization, the uncertainty from this source is halved, but the statistic uncertainty is increased so that the total uncertainty is $-18.6\%/+16.4\%$ (table 14.6).

Jet energy scale recalibration

As jet energy scale is the dominant uncertainty in this channel, the improvements by using the jet energy scale recalibration procedure described in section 14.2.1 were examined.

Using the same selection cuts, but with the recalibration procedure, the systematic uncertainty from jet energy scale is significantly reduced: if the expected value for the $m(jj)$ mass peak shift is used ($\pm 2.7\%$), the uncertainty becomes $-3.8\%/+4.0\%$, with respect to the $-10.3\%/+7.8\%$ achieavable without this procedure.

Table 14.6: Expected uncertainties in the new di-leptonic tW channel analysis. The uncertainty from simulated statistics was not added to the total. Uncertainties with † were taken from the old analysis.

Statistics	-10.9%	$+10.9\%$
$\sigma(W + jets)$ [$\pm 10\%$]	-0.7%	$+0.7\%$
luminosity [5%]	-5.5%	$+5.5\%$
jet energy scale	-10.3%	$+7.8\%$
b tagging	-4.5%	$+2.3\%$
PDF†	-6.6%	$+4.4\%$
Pile-up†	$+6.1\%$	6.1%
Total uncertainty	$\mathbf{-18.6}\%$	$\mathbf{+16.4}\%$
Simulated statistics	-11.5%	$+11.5\%$

Even assuming a $\pm 1\%$ uncertainty on the peak position, a good improvement was found: for a shift of $\pm 1.7\%$ the systematic uncertainty is reduced to $-4.2\%/+6.0\%$, while for a shift of $\pm 3.7\%$ the reduction is even larger $-1.6\%/+1.5\%$.

The total uncertainty on the cross section is reduced to $-16\%/+15\%$.

If the recalibration procedure is applied, the cuts used above are no longer optimal, so the selection was re-optimized again, using the jet energy scale uncertainty from the recalibration assuming the $\pm 2.7\%$ shift in the mass peak.

After the optimization procedure, the total uncertainty on the cross section is reduced even more, so that the final $\Delta\sigma/\sigma$ is $-15.2\%/+13.8\%$, which is a definite improvement with respect to the $\pm 26\%$ uncertainty expected from the old analysis.

14.5 Single top s channel revisited

The analysis of s-channel single top was affected by large systematic uncertainties, caused by the small production cross section and the overwhelming background.

14.5.1 Changes

Simulation The only difference with respect to the old analysis was the use of full simulation for $t\bar{t}$ background, for which such samples were readily available

Reconstruction The $b \leftrightarrow W$ pairing to reconstruct the top quark was done by choosing the pair with minimum angular separation ΔR, mostly for practical reasons, as in the tW analysis no significant loss was found when this much simpler procedure was used. The use of more advanced techniques will be left to further developments on this analysis.

Jet recalibration As the uncertainty on the jet energy scale was among the dominant sources of uncertainty on the cross section, in this analysis the procedure of jet energy scale recalibration was used; this allows to reduce by a factor of two the uncertainty from this source.

14.5.2 Selection

The event selection was performed using the same kinematic variables considered in the old analysis, Signal events were selected requiring:

- two b jets with $p_T > 46,\ 31\,\text{GeV}$; the highest b-tagging discriminator was required to be > 3.3, and the lowest > 2.2.
- one lepton passing the HLT single lepton channel, and no additional leptons with $p_T > 5\,\text{GeV}$
- no additional jets with $p_T > 25\,\text{GeV}$, in any η range
- $E_T^{miss} > 20\,\text{GeV}$
- $|\Sigma_T| < 58.8\,\text{GeV}$, $151\,\text{GeV} < H_T < 375\,\text{GeV}$
- $M_T(W \to \ell\nu) < 118\,\text{GeV}$

No cut on the top invariant mass was imposed. As done for the other analysis, most of the thresholds for the cuts were optimized using the JGAP genetic algorithm package.

The expected yield for s channel is 163 events for $10\,\text{fb}^{-1}$, while 832 background events are expected, from t-channel single top (358), $t\bar{t}$ (205), $Wb\bar{b}$ (122), $W + jets$ (91) and tW (56).

The corresponding signal to background ratio is 0.2, slightly better than was achieved in the other analysis, but the signal efficiency is also lower.

$t\bar{t}$ background A control sample for $t\bar{t}$ background selection was extracted from the same preselection stream used before for dileptonic tW selection. Two leptons ($p_T > 20\,\text{GeV}$), and two hard jets were required ($p_T(> 40,\ 35\,\text{GeV}$, b-tagg. discr. $> 0, 1.87$), and no other jet with p_T above $30\,\text{GeV}$; additional requirements were $E_T^{miss} > 20\,\text{GeV}$, $|\Sigma_T| > 37\,\text{GeV}$ [4].

The expected yield for $10\,\text{fb}^{-1}$ is 2554 dileptonic $t\bar{t}$ events, with negligible contributions from dileptonic tW (27.5), other decays $t\bar{t}$ (17.6) and t channel single top (17.5).

t channel background For the abundant background from t-channel single top production, a control sample was obtained starting from the events preselected in the t-channel analysis. The additional requirements imposed were: for the b jet $p_T > 45.4\,\text{GeV}$, b-tagg. discr. > 0.84; for the light quark jet $|\eta| > 2.2$, $p_T > 56.5$; $E_T^{miss} > 40\,\text{GeV}$; $|\Sigma_T| < 72.4\,\text{GeV}$; $M_T(W \to \ell\nu) < 133\,\text{GeV}$, $102\,\text{GeV} < M(top) < 239\,\text{GeV}$.

The expected yields are 2986 t-channel events, 1788 events $W + jets$, and 196 events from all the other processes combined. The non small contamination from $W + jets$ appears not to be a problem for the analysis, as there are events from $W + jets$ also among the signal-like events, so that the systematic uncertainties from the $W + jets$ cross section and luminosity are reduced.

[4] The $|\Sigma_T|$ in this preselection stream was calculated assuming a dileptonic tW decay, so it does not include the second jet

Systematic uncertainties

Most of the systematic uncertainties were evaluated, and are listed in table 14.7. The dominant uncertainty is from the statistics (±20%), while contributions from background cross sections, luminosity and b tagging are at the 6-7% level.

Thanks to the recalibration procedure and the use of higher thresholds for jets, at which the jet energy scale is known more precisely, the uncertainty from jet energy scale is greatly reduced, becoming only $-3.2\%/+1.1\%$.

As the dominant contribution is from statistics, improvements are expected with a larger amount of integrated luminosity: already for $20\,\mathrm{fb}^{-1}$, rescaling only the statistical uncertainty, the cross section could be measured with an overall accuracy of $-20.0\%/+18.8\%$.

Table 14.7: Expected uncertainties in the new s-channel analysis. The uncertainty from simulated statistics was not added to the total.

Statistics	-20.2%	$+20.2\%$
$\sigma(W+jets)$ [±10%]	-7.6%	$+7.6\%$
$\sigma(Wb\bar{b})$ [±10%]	-7.1%	$+7.1\%$
$\sigma(tW)$ [±10%]	-2.5%	$+2.57\%$
luminosity [5%]	-6.0%	$+6.0\%$
jet energy scale†	-3.2%	$+1.1\%$
b tagging	-6.1%	$+0.4\%$
Total uncertainty	$\mathbf{-24.6}\%$	$\mathbf{+23.6}\%$
Simulated statistics	-31.5%	$+31.5\%$

† jet energy scale recalibration has been used, assuming a shift of ±2.7% on the $m(jj)$ peak.

14.6 Conclusions

14.6.1 Status

Studies on single top quark physics at CMS are still ongoing, with results being constantly improved, but some basic facts are sufficiently established.

The simplest goal, observing the t channel production, will surely be met for $10\,\mathrm{fb}^{-1}$ (if the SM is true), and is likely to be achievable even before: a simple estimate suggests that even with the performance of the old analysis observation should be possible with significance > 7 even for an integrated luminosity of $1\,\mathrm{fb}^{-1}$.

The associated tW production will be somewhat harder to observe, but surely within reach of the first years (10-20 fb^{-1}).

In this thesis I have shown that the results of the preceding analysis can be improved in many ways: a better use of the kinematic variables, normalization of the $W+jets$ background using data and jet energy scale recalibration.

The use of tracks with signal vertex association to remove extra jets should also reduce the systematic uncertainty from the amount of pile-up, which was

among the dominant uncertainties in the old analysis; an estimate of this reduction will be among the next tasks in the future.

The hardest goal would be observing s-channel production. In this work I was able to reduce significantly the uncertainty from jet energy scale using the jet recalibration, and control part of the other uncertainties by normalizing backgrounds from $t\bar{t}$ and t-channel single top using data; this could allow to measure the cross section with 20% accuracy with $20\,\mathrm{fb}^{-1}$, but further improvemens are surely possible. Nevertheless, it is hard to belive that precision $|V_{tb}|$ measurements could be extracted from this channel after a few years of LHC.

14.6.2 Outlook

Looking forward, the next steps for single top quark studies at CMS can be many, beyond the necessary work of improving some specific details that are still pending in the current analyses, and further optimization of the current results.

Early physics Designing a selection of single top quark events for the very first runs of LHC, to improve the simple extrapolations to $1\,\mathrm{fb}^{-1}$ done in this work, is surely a priority for short term physics. At that time the first positive results from Tevatron are expected to be available, so that an independent validation of the result will be possible.

Precision measurement of $|V_{tb}|$ In the long term, a careful study of the accuracy attainable on $|V_{tb}|$ from single top searches should be done, taking into account all the channels, possibly targeted to higher luminosities, such as $30\,\mathrm{fb}^{-1}$, at which systematic uncertainties should be smaller. The extraction of $|V_{tb}|$ is affected by theoretical uncertainties (i.e. from PDFs or scale dependence), so that an analysis tuned for the best measurement of the production cross sections could be not optimal for $|V_{tb}|$ measurement.

Improving the tools The current analyses are still based on basic tools; after their results will be established, the use of more advanced techniques could be attempted: the use of kinematic fits and multi-variate methods should probably provide significant improvements, even if the evaluation of the systematic uncertainties coming from the greater use of Monte Carlo information will be more difficult. When LHC will be running, anyway, data driven calibrations could be used for these methods, further improving the results.

Top polarization After the signal from t-channel single top will be observed, studies of the specific features of this process will be possible. In particular, a measurement of the polarization of the top quark will surely be among the goals of single top physics at CMS at that time. In Beyond-SM theories with charged Higgs bosons, for instance, events in which the $W^{\pm}$ boson is replaced by $H^{\pm}$ could be discriminated by looking at the top quark polarization.

14.7 Acknowledgements

I would like to thank Roberto Tenchini and Andrea Giammanco for the guidance and support in this analysis and in the di-leptonic tW analysis for [PTDRv2], the members of the semi-leptonic tW working group from Taiwan (P. Yeh, K. F. Chen, Y.J. Lei, J. Schuemann, Y. Chao, J.G. Shiu, S. Blyth) as feedback and discussion with them allowed to improve the tW much, and M. Duda and D.F. Teyssier for providing part of the Monte Carlo samples used in this studies.

I would also like to thank many people from the CMS Pisa group, which provided in understanding many aspects of CMS including event reconstruction, trigger and the tracker integration and burn-in: Simone Gennai, Andrea Rizzi, Boris Mangano, Fabrizio Palla, Marcel Vos, and many others too...

Acknowledging all the people that contributed less direcly to all these studies and to the background knowledge that made these work possible would be really too long.

Bibliography

General books and reference on QFT and particle physics

[Peskin] M. Peskin and D. Schroeder, *An Introduction to Quantum Field Theory*, Westview Press

[Weinberg] S. Weinberg, *The Quantum Theory of Fields*, Cambridge University Press

[Strocchi] F. Strocchi, *Symmetry Breaking (Lecture Notes in Physics)*, Springer

[Streater] P. Streater and A. Whightman, *P C T, Spin and Statistics and All That*, Bejnamin

[Barger] V. Barger and R. Philips, *Collider Physics*, Addison-Wesley

[Perkins] D. Perkins, *Introduction to High Energy Physics*, Cambridge University Press

[PDG] S. Eidelman *et al.*, Phys. Lett. B **592**, 1 (2004) and 2005 partial update for the 2006 edition available on the PDG WWW pages (URL: `http://pdg.lbl.gov/`)

Hadronic physics, and related generators

[CTEQ] J. Pumplin *et al.* (Coordinated Theoretical-Experimental Project on QCD, CTEQ), *New Generation of Parton Distributions with Uncertainties from Global QCD Analysis*, `http://www.phys.psu.edu/~cteq/` and [arXiv:hep-ph/0512167]

[AP] G. Altarelli and G. Parisi, Nuclear Physics B **126** (1977), 298

[Peterson] D. Peterson *et al.*, Scaling violations in inclusive e^+e^- annihilation spectra, Phys. Rev. D **27** (1983) 105

[PYTHIA] T. Sjöstrand, *The PYTHIA Event Generator* JHEP **05** (2006) 026, also on LU TP 06-13, FERMILAB-PUB-06-052-CD-T, [arXiv:hep-ph/0603175] and online at `http://www.thep.lu.se/~torbjorn/Pythia.html`

[AlpGen] M. L. Mangano, M. Moretti, F. Piccinini, R. Pittau, A. Polosa, JHEP **0307:001**,2003, [arXiv:hep-ph/0206293] and `http://mlm.home.cern.ch/mlm/alpgen/`

Top quark physics

[TopQuark] CDF Collaboration *Observation of Top Quark Production in $\bar{p}p$ Collisions with the Collider Detector at Fermilab*, Phys. Rev. D **74** 2626 (1995)
D0 Collaboration *Observation of the Top Quark*, Phys. Rev. D **74** 2632 (1995)
C. Campagnari and M. Fankilin, *Discovery of the Top Quark*, Phys. Rev. D **69** 137

[TEWG] Tevatron Electroweak Working Group (for the CDF and D0 Collaborations), *Combination of CDF and D0 Results on the Mass of the Top Quark*, [arXiv:hep-ex/0603039]

[Heinemeyer] S. Heinemeyer *et al.*, [hep-ph/0604147]

[Mahlon] G. Mahlon and S. Parker, , *Improved spin basis for angular correlation studies in single top quark production at the Fermilab Tevatron*, Phys. Rev. D **55** (1997) 7249

[Vtb] J. Alwall *et al.*, *Is $V_{tb} = 1$?,* [arXiv:hep-ph/0607115]

[Stelzer] T. Stelzer, Z. Sullivan, and S. Willenbrock, *Single-top-quark production via W-gluon fusion at next-to-leading order*, Phys. Rev. D **56** (1997) 5919 [arXiv:hep-ph/9705398].

[Campbell] J. Campbell and F. Tramontano, *Next-to-leading order corrections to Wt production and decay*, Nucl. Phys. B **726** (2005) 109–130 [arXiv:hep-ph/0506289].

[Maltoni] F. Maltoni, *tW: definition and measurement at the LHC*, Presentation given at the Top2006 workshop at Coimbra

[Smith] M. C. Smith and S. Willenbrock, *QCD and Yukawa Corrections to Single-Top-Quark Production via $q\bar{q} \to t\bar{b}$*, Phys. Rev. D **54** (1996) 6696 [arXiv:hep-ph/9604223].

[TopRex] S. R. Slabospitsky and L. Sonnenschein, Comput. Phys. Commun. **148** (2002) 87 [arXiv:hep-ph/0201292].

CMS detector and reconstruction

[PTDRv1] CMS collaboration, *CMS Physics Technical Design Report Vol. I* **CERN/LHCC 2006-001**, CMS TDR 8.1 (2006), `http://cmsdoc.cern.ch/cms/cpt/tdr/`

[ECTDR] CMS collaboration, *The Electromagnetic Calorimeter Technical Design Report* **CERN/LHCC 2006-001**, CMS TDR 8.1 (2006)

[PTDRv2] CMS collaboration, *CMS Physics Technical Design Report Vol. II*, in preparation.

[CMS NOTE 2006/041] W. Adam, Th. Speer, B. Mangano, T. Todorov, *Track reconstruction in the CMS tracker* CMS Note **2006/041** (2006)

[CMS NOTE 2006/026] S. Cucciarelli, M. Konecki, D. Kotlínski, T. Todorov, *Track reconstruction, primary vertex finding and seed generation with the Pixel Detector* CMS Note **2006/026** (2006)

[KF] R. Frühwirth, P. Kubinec,W. Mitaroff, and M. Regler, *Vertex reconstruction and track bundling at the LEP collider using robust algorithms*, Comput. Phys. Commun. **96**, (1996) 189208. [doi:10.1016/0010-4655(96)00040-9]

[1] K. Prokofiev and T. Speer, *A kinematic fit and a decay chain reconstruction library*, **CERN 2005-002** (2005). Proc. of the 2004 Conference for Computing in High-Energy and Nuclear Physics (CHEP 04), Interlaken, Switzerland, 2004, available at `http://indico.cern.ch`.

[CMS NOTE 2006/042] V. Konoplianikova, A. Ulyanov, O. Kodolova, *Jet Calibration using $\gamma + jet$ Events in the CMS Detector* CMS Note **2006/042** (2006)

[CMS NOTE 2004/015] O. Koldova *et al.*, *Jet energy correction with charged particle tracks in CMS* CMS Note **2004/015** (2004)

[CMS NOTE 2005/027] J. D'Hondt, S. Lowette, J. Heyninck, S. Kasselmann, *Light quark jet energy scale calibration using the W mass constraint in single-leptonic $t\bar{t}$ events* CMS Note **2005/027** (2005)

[CMS NOTE 2006/019] A. Rizzi, F. Palla, G. Segneri, *Track impact parameter based b-tagging with CMS* CMS Note **2006/019** (2006)

[CMS NOTE 2006/014] C. Weiser, *A Combined Secondary Vertex Based B-Tagging Algorithm in CMS* CMS Note **2006/014** (2006)

[CMS NOTE 2006/043] P. Demin, S. de Visscher, A. Bocci, R. Ranieri, *Tagging b jets with electrons and muons at CMS* CMS Note **2006/043** (2006)

[CMS NOTE 2006/030] M. Vos, F. Palla, *B-tagging in the High Level Trigger* CMS Note **2006/030** (2006)

[CMS NOTE 2006/028] S. Gennai *et al.*, *Tau jet reconstruction and tagging at High Level Trigger and off-line* CMS Note **2006/028** (2006)

Other High Energy Physics experiments

[Atlas] ATLAS Collaboration, *ATLAS detector and physics performance, vol. II* **CERN/LHCC 99-15**, ATLAS TDR 15 (2006).

[ILC] International Linear Collider, `http://www.linearcollider.org`

[TOTEM] TOTEM Collaboration, *TOTEM Technical Design Report*, **CERN/LHCC 2004-002** (2004)

Searches for single top quark

[CDF] CDF Collaboration, *Single-Top-Quark Search with* $0.7\,fb^{-1}$, CDF Note 8185

[CMS NOTE 2006/111] M. Baarmand, H. Mermerkaya, I. Vodopiyanov, *Measurement of Spin Correlation in Top Quark Pair Production in Semi-Leptonic Final State* CMS Note **2006/111** (2006)

[2] Z. Sullivan, *Understanding single-top-quark production and jets at hadron colliders*, Phys. Rev. D **70** (2004) 114012, [arXiv:hep-ph/0408049]

[CMS NOTE 2006/084] ,V. Abramov *et al*, *Selection of Single Top Events with the CMS Detector at LHC* CMS Note **2006/084** (2006)

[CMS NOTE 2006/086] , P. Yeh *et al*, *Search for W-associated Production of Single Top Quarks in CMS* CMS Note **2006/086** (2006)

Software

[G4] GEANT4 Collaboration, *GEANT 4 – a simulation toolkit*, Nucl. Instrum. and Methods **A506** (2003) 250-303, [doi:10.1016/S0168-9002(03)01368-8]
GEANT4 Collaboration, *Geant4 Developments and Applications*, IEEE Transactions on Nuclear Science, **53** (2006) 270-278 [doi:10.1109/TNS.2006.869826]
Online at `http://geant4.web.cern.ch`

[ROOT] *ROOT: ab Object Oriented Data Analysis Framework*, `http://root.cern.ch`

[OSCAR] *OSCAR:CMS Simulation Package Home Page*, `http://cmsdoc.cern.ch/OSCAR` and section 2.5 of [PTDRv1]

[ORCA] *ORCA:CMS Reconstruction Package*, `http://cmsdoc.cern.ch/ORCA` and section 2.5 of [PTDRv1]

[FAMOS] *CMS Fast Simulation*, `http://cmsdoc.cern.ch/FAMOS` and section 2.6 of [PTDRv1]

[JGAP] *Java Genetic Algorithm Package*, `http://jgap.sourceforge.net`

[FreeHEP] *The FreeHEP java libary*, `http://java.freehep.org/`